MICROYIELDING AND FLOW IN NIOBIUM ALLOY CRYSTALS

by

F.GRAHAM WILSON

B.A., University of Cambridge, 1966

A THESIS SUBMITTED IN PARTIAL FULFILMENT OF

THE REQUIREMENTS FOR THE DEGREE OF

DOCTOR OF PHILOSOPHY

in the Department

of

METALLURGY

We accept this thesis as conforming

to the required standard

THE UNIVERSITY OF BRITISH COLUMBIA

December, 1969

In presenting this thesis in partial fulfilment of the requirements for an advanced degree at the University of British Columbia, I agree that the Library shall make it freely available for reference and study. I further agree tha permission for extensive copying of this thesis for scholarly purposes may be granted by the Head of my Department or by his representatives. It is understood that copying or publication of this thesis for financial gain shall not be allowed without my written permission.

Department of Metallurgy

The University of British Columbia
Vancouver 8, Canada

Date December 22, 1969

ABSTRACT

Oriented single crystals of niobium and dilute alloys with molybdenum and tantalum were deformed in tension between 77°K and 500°K, and the macroflow and slip parameters established. At high temperatures the main effect of alloying was to increase the flow stress, considerably more with molybdenum than with tantalum. The observed yield drop and subsequent plastic flow were explained in terms of a stability theory relating changes in yield and work hardening parameters with temperature and addition of solute.

A technique was developed for measuring small plastic strains in the microflow region, and for recording the dynamic transition to macroflow. From studies on pure niobium between 77°K and 295°K, the nature of dislocation motion at small strains was established; microflow was explained in terms of a transition from edge dislocation motion to screw dislocation motion at the macroflow stress. Interstitial effects were found to be particularly significant during microflow, and are probably important in determining the low temperature flow stress in even the highest purity bcc metals. A further low temperature contribution comes from a directional component of the internal stress field which depends on the distribution of dislocations rather than on their density.

Microflow curves were obtained for niobium alloy crystals, and the interaction of dislocations with substitutional solute atoms

established. In contradiction to previous suggestions, substitutional solute was found to restrict the mobility rather than the multiplication of dislocations. The elastic contribution of solute atoms to the internal stress field was confirmed, although a quantitative theory for bcc alloys does not yet exist.

Peierls stress considerations alone were found to be incapable of explaining either the temperature sensitivity of flow or the low temperature solution softening; the short range interaction of interstitials with the dislocation core was considered to be more significant.

TABLE OF CONTENTS

PAGE

PAGE

LIST OF TABLES

LIST OF FIGURES

PAGE

PAGE

ACKNOWLEDGEMENT

It is a pleasure to acknowledge the helpful discussions with my research director, Professor E. Teghtsoonian, and with Dr. R.D. Warda. I am also grateful for the secretarial assistance of my wife, who no longer thinks that "microstraining" involves tiny sieves.

1. INTRODUCTION

It is only within the last decade that fundamental studies of deformation processes in bcc crystals have been undertaken. Attention had previously been restricted to fcc and hcp metals because they can easily be obtained as high purity single crystals. The development of electron beam melting in the late fifties enabled niobium, tantalum, molybdenum, and tungsten to be similarly prepared; consequently the deformation characteristics of these metals have received considerable attention. It has been shown that their behaviour is often similar to that of the other metal structures, but there are important differences. In particular, bcc crystals show a very marked strengthening at low temperatures, a complex slip behaviour, marked orientation effects, and discontinuous yielding in all but the purest materials. Since these effects are a result of the motion of dislocations, it has been necessary to consider the detailed properties of dislocations in bcc crystals.

Much of the theoretical interest and accompanying controversy has been concerned with determining the rate-controlling mechanisms of plastic deformation. A majority opinion considers the intrinsic nature of dislocations in the bcc lattice to be the most important feature. However, even the purest crystals contain significant amounts of interstitial impurities, and it is possible that impurity effects may be more important than intrinsic lattice effects.

The application of thermal activation analysis and dislocation dynamics has proved very useful in relating many of the observed effects, but it has not been possible to distinguish between intrinsic and impurity-controlled behaviour. Several new experimental techniques have

been used, particularly the etch-pit and microstrain techniques; the etch-pit technique has usually employed single crystals, while most microstrain tests to date have been performed on polycrystals.

Whereas the effect of substitutional elements has been well established for fcc crystals, most of the data on pure bcc alloys has been published only since the beginning of this work. The microstrain technique offers particular advantages in the study of alloy effects and this work probably represents its first application to the deformation of bcc substitutional alloy crystals.

From the family of bcc refractory metals, niobium was selected as a solvent having a melting point and vapour pressure most suitable for the preparation of pure single crystals. Molybdenum and tantalum were selected as sufficiently different solutes which both show complete solid solubility in niobium and have similar vapour pressures (see A.1).

The initial part of the program was concerned with the conventional tensile testing of pure niobium single crystals over a range of variables such as orientation, temperature and strain-rate. These experiments served to establish and evaluate procedures, and provided a basis for selecting specific conditions for the subsequent deformation of alloy crystals.

The deformation properties of pure niobium and niobium alloy crystals were investigated in detail using macro and microstrain testing techniques. Since the microstrain technique is new, considerable effort was spent in interpreting the results of the technique and in assessing its importance. It was hoped that by applying the technique to a wide range of alloys, more insight could be gained into the interpretation of results from observations on pure bcc crystals.

2. EXPERIMENTAL PROCEDURE

2.1 Specimen preparation

2.1.1 Materials

Polycrystalline rod, 1/8 inch in diameter was obtained from two sources. The initial experiments were performed on pure Nb (minimum 99.82%) from Kawecki Chemical Co, New York. The subsequent experiments were performed on high purity material obtained from the Materials Research Corporation, New York. The six Nb alloys contained nominally 0.5, 2 and 8 atomic percent each of Mo and Ta as solute. A pure Nb sample (containing initially about 40 ppm interstitial impurities) had undergone the same melting and fabrication procedure. For each alloy series, this material acted as a control in the evaluation of interstitial and substitutional solute effects. The interstitial content of the polycrystalline alloy rods after fabrication was not known.

2.1.2 Melting procedure

Single crystals, 1/8 inch in diameter and up to 8½ inches long, were grown in an electron beam zone melter based on the original design (Calverley et al (1957)). Using an emission current of about 100 mA at 2000 V potential, single crystals were obtained by passing the molten zone at 25 cm hour^{-1}. This high speed was used to suppress any redistribution of solute in the liquid zone. Purification by electron beam zone melting occurs mainly by vacuum distillation (Votava (1965)), so the distribution of interstitial impurities along

the rods can be regarded as sufficiently homogeneous. There is also a possibility of preferential loss of one of the alloy constituents, but from the relative and absolute values of the vapour pressures of the components at the melting temperature of the alloy (A.1), this loss is expected to be slight. However this was not the case with the attempted preparation of some NbV alloy crystals. The V loss could have been reduced by operating at high pressures, but there is an upper pressure limit set by the operation of the electron emission technique and by the possibility of gaseous contamination.

2.1.3 Impurities

The dynamic vacuum employed during zone melting was in all cases from 2 - 8 x 10^{-5} torr, this value being a compromise between the loss of substitutional solute and the gain of interstitial impurities. However, the high pressure might have removed some carbon as carbon monoxide (Taylor and Christian (1965)) and hydrogen is relatively easily removed by vacuum distillation.

Pemsler (1961) has given data for the thermodynamics of the interaction of N_2 and O_2 with Nb at high temperatures in the form of Sieverts Law plots. The concentration of N and O in equilibrium with liquid Nb at 2470°C under an applied pressure of 5 x 10^{-5} torr has been calculated to be 27 and 12 wt ppm of N and O respectively (see A.2). Although the equilibrium concentration in the hot solid region will be higher than this, the initial material will contain far more than 40 ppm, so contamination during electron beam melting should not be a problem. However it is unlikely that very much purification could be expected under the above melting conditions.

To reduce contamination from the tungsten cathode, it was heated to a high temperature for some time before melting the specimen and then operated at the lowest possible emission temperature during melting.

2.1.4 Oriented single crystals

A technique for producing oriented seed crystals was devised and used for each alloy to eliminate any possible composition gradients caused by melting together different alloys. The method involved melting part of a short length of rod to produce a single crystal, mounting the specimen for Laue back-reflection photography, and then bending the polycrystalline end to give the desired orientation relative to the X-ray beam. A permanent seed crystal was then grown from the oriented crystal and, once prepared, could be used repeatedly.

The as-grown rods were confirmed to be single crystals of the desired orientation by taking Laue back-reflection photographs at points along their lengths. They were carefully cut with a jeweller's saw into pieces about 4 cm long, after having discarded the immediate beginning and end of the melted region.

2.1.5 Specimen shaping

A spark lathing technique using deionized water as dielectric was developed to produce a reduced gauge section on the crystal lengths. A tapered copper electrode was passed alongside the rotating crystal and the spark energy gradually reduced during the operation from 4×10^4 to 5×10^3 ergs. A final hand polish was given with 2/0 and 4/0 emery papers.

About 0.25 mm (10 thou) was then removed from the gauge section

by chemical polishing in a solution of 1 part HF / 3 parts HNO_3. Gauge diameters were in general uniform to within 0.01 mm and typical specimen dimensions were as follows:

gauge diameter	2.00 mm
gauge length	20 mm
shoulder diameter	3 mm
shoulder radius	2 mm

2.1.6 Crystal perfection

The extent of spark erosion damage on single crystals will depend on the material, the spark energy, the cutting conditions, and the crystal orientation. Damage up to depths of 300μ has been reported in materials softer than Nb (Ahktar (1968)). To evaluate the effect in Nb, successive layers 0.05 mm deep were chemically polished from the surface until 0.3 mm had been removed. At each stage a Laue back-reflection photograph was taken and the specimen was examined optically. After the very first polish, the Laue spots were always exactly the same as on the as-grown crystal. This indicates either that the damage was very slight or that absence of asterism in Laue photographs is no evidence of lack of strain in Nb crystals. The optical observations revealed damage after 0.05 mm had been removed from the surface, but a constant pattern of dislocation etch pits was observed if 0.1 mm or more was removed.

The completed specimens were X-rayed. Some of the large-angle reflections were observed to be composed of several small discrete spots, indicating the presence of a sub-structure of less than ½° misorientation. This was also indicated by the presence of longitudinal striations observed

in the microscope after etching to reveal dislocations. This sub-structure was also seen on the as-grown crystals. A similar sub-structure has been recognized in W and other bcc metals (Koo (1963)).

2.2 Analysis of alloys

2.2.1 Substitutional elements

X-ray fluorescence analysis was performed on each of the alloys before and after melting. A measure of solute content was obtained from a "fluorescence parameter", R, defined as the ratio of the secs/count produced on a solute peak to the secs/count produced on a Nb peak. The ratios used were $\frac{MoK\alpha}{NbK\beta}$ for Mo and $\frac{TaL\alpha}{NbK\alpha}$ for Ta. It was better to time counts rather than count for a fixed time, since the solute counts were then taken over a longer period and the dilute element received statistically more weight.

In all cases the variation of R with position along an as-grown rod was less than the standard deviation of R (maximum 5%). Therefore, the composition along the rods can be regarded as uniform within the sensitivity of the fluorescence technique. Absolute analysis is not possible unless standards are available.

An analysis of the as-received material was given by the suppliers. After crystal growth, a further analysis was performed by Ledoux and Co, New Jersey. The results are given in Table I, together with the letter used throughout for alloy identification and the parameter R obtained from X-ray fluorescence. Because of the inconsistencies in the Mo results, a repeat analysis on this series was performed by Coast Eldridge, Vancouver, and these results are also included in the table.

Table I. Analyses of Nb alloys.

Alloy identification		B	C	D	J	K	L
Nominal at% alloy		0.5 Ta	2.0 Ta	8.0 Ta	0.5 Mo	2.0 Mo	8.0 Mo
As-supplied:	MRC	0.31	1.53	5.04	0.72	1.84	6.15
	Coast Eldridge	-	-	-	0.79	4.84	5.93
As-grown:	Ledoux	0.55	2.21	4.41	1.31	6.38	7.62
	Coast Eldridge	-	-	-	0.69	4.74	5.99
Fluorescence parameter,R:							
	As-supplied	7.1	14.8	33.6	8.9	27.7	37.7
	As-grown	7.3	14.8	33.9	9.7	31.5	40.6
Best value, as-grown		0.5 Ta	1.7 Ta	4.8 Ta	0.9 Mo	4.9 Mo	6.6 Mo

Specimen identification: Each alloy series was given an identifying letter as above; pure Nb was A. A digit following the letter identifies a particular crystal; a second digit identifies the position of the specimen within the crystal. Thus, K41 is the first tensile specimen taken from the fourth crystal of Nb 4.9 Mo.

The values given for the NbMo alloys present a rather confusing picture. In particular it appears that the as-supplied alloy K must have contained far more than the 1.84 at% Mo quoted by MRC, yet the as-grown value of 6.38 at% by Ledoux seems improbably high. In an attempt to clarify the situation, the parameter R was plotted against the various quoted values and the most reasonable calibration curve drawn (Fig 1). The fluorescence results were then used to arrive at the best analysis values shown in Table I.

2.2.2 Interstitial elements

An analysis of C, H, N and O was performed on a selection of alloys by Ledoux. The results are shown below with the interstitial contents given in wt ppm.

Crystal	C	H	N	O	Initial melting pressure (x 10^{-5} torr)
A4	10	5.8	8	102	7.6
D7	13	3.4	3	89	5.3
K3	10	3.7	9	28	2.3
L5	16	3.1	11	42	3.0

Also included is the pressure in the electron beam melter when melting was commenced. There is a possible correlation between this pressure and the interstitial oxygen concentration. The analysis figures for N and O show no resemblance to the values calculated from equilibrium thermodynamics (see A.2).

The total interstitial content is frequently quoted when comparing materials; in this case a typical value would be about 80 ppm total interstitials.

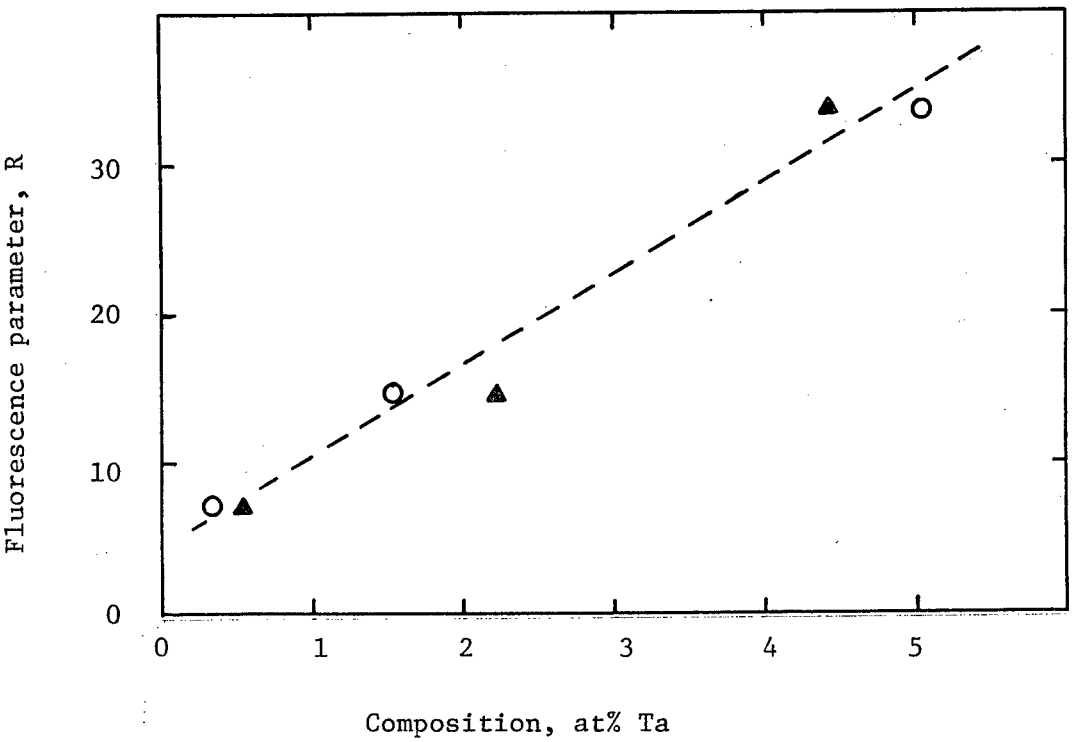

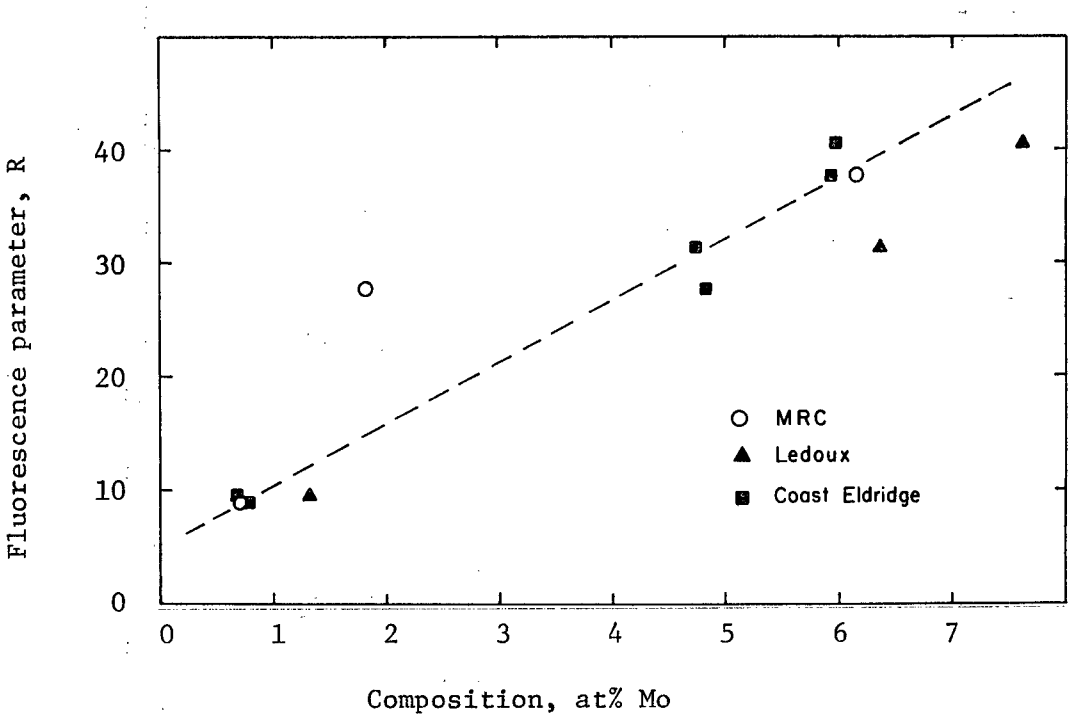

Fig 1. Analysis of Nb alloys: a) NbTa b) NbMo

2.3 Mechanical testing

2.3.1 Specimen deformation

In a tensile test it is necessary to ensure that loading is uniaxial and that no bending moments are introduced into the specimen. During single crystal deformation there is continuous reorientation of the lattice in the gauge length so that to completely prevent bending, the axis of a universal joint must lie at the ends of the gauge length. For the small strains mainly used in this study, the problem is less serious. However to reduce bending and ensure the colinearity of tensile and specimen axes, universal joints were placed outside the specimen shoulders. The specimens themselves were held by the shoulders in split-jaw grips and loaded into the machine using a special jig to prevent accidental damage. Straining was performed on a Floor Model Instron.

2.3.2 Strain measurement

Two regions of strain sensitivity were investigated:

a) Macrostrain region ($\varepsilon > 5 \times 10^{-4}$)

In this region it is usual to measure strain indirectly from the motion of the Instron crosshead, which effectively gives a load-time plot on the Instron chart. This is satisfactory for materials showing discontinuous yielding or for low strain sensitivities of the order of 10^{-3} (ie a 0.1% proof stress).

In order to investigate the use of the crosshead displacement as a measure of strain at sensitivities of 10^{-4}, an Instron extensometer was attached directly to the specimen and the true displacement recorded on the X-axis of an Instron X-Y recorder. Using a fully elastic specimen

in the inverted-cage tensile jig, a non-linear load-time plot was obtained at strain sensitivities of 10^{-4} with loads of 40 lbs. This was attributed to an inherent non-linearity in the Instron crosshead movement when under load. It was also observed htat, in spite of all precautions, a significant amount of plastic deformation occurred at the specimen shoulders during straining. For these reasons, whenever necessary, strain was recorded on an extensometer attached directly to the specimen.

In the conventional testing using load-time curves, temperature control was obtained by immersing the specimen in various hot and cold liquid baths.

b) Microstrain region ($\varepsilon = 10^{-6} - 5 \times 10^{-4}$)

A high sensitivity extensometer was designed and built,consisting essentially of two parallel plates secured to the tensile specimen. The separation was monitored using a Wayne Kerr DM100B distance meter and the output amplified by a high sensitivity X-Y recorder. The signal from the Instron load cell was fed directly to the Y-axis of the recorder. Details of the design and construction of the extensometer are given in A.4. The recorder gave a continuous plot of load and of extension of the specimen gauge.

The construction of the extensometer did not enable it to be used above room temperature. For use at low temperatures, a nitrogen gas-cooling cryostat was designed and built (see A.4).

2.3.3 Computations

A special jig was constructed for use with an optical microscope and X-ray set which allowed slip (or twin) systems to be determined on any cylindrical specimen. The method involved measuring the angle from the slip trace to the tensile axis at any point around the crystal, and

employed a two-surface trace analysis. A graphical extension of the technique (see A.3) enabled two or even three systems operating together to be identified.

A program was written for an IBM 360 computer which enabled coordinates taken directly from the Instron chart to be converted to resolved shear stress versus shear strain on the observed slip system. These results were obtained graphically as a flow curve. This procedure assumed that only one slip system was operative, and that deformation was uniform, which was not always the case.

3. GENERAL DEFORMATION CHARACTERISTICS OF PURE NIOBIUM

The flow properties of pure Nb single crystals have been established by Mitchell et al (1963) over a range of purities, orientations, temperatures and strain-rates. The geometry of the operative slip plane has been studied in detail by Foxall et al (1967). In order to study the effect of solute on pure Nb it was necessary to restrict many of the above variables. A few experiments were performed on pure Nb to confirm the general deformation characteristics which are summarized below.

3.1 Effect of purity

The yield stress and flow stress of Nb decrease with increasing purity and the shape of the flow curve is altered (Mitchell et al (1963)). Bowen et al (1967) have prepared high purity crystals by ultra-high vacuum annealing. Although the impurity content could not be determined, the crystals aged significantly within a few weeks in air at room temperature. The crystals used here did not age detectably over a period of four months.

3.2 Effect of orientation

Much discussion has centred on the dependence of the yield stress and the temperature sensitivity of yield, on the orientation of the tensile axis (see Bowen et al (1967)). The effect on the flow curve is very marked for crystals oriented near the corners of the stereographic triangle. Fig 2 shows flow curves for three crystals of extreme orientations. The stress has been resolved onto the (011) plane in each case. Within the stereographic triangle the effect of orientation is less marked, although different slip systems operate in different regions of the triangle. Foxall et al (1967)

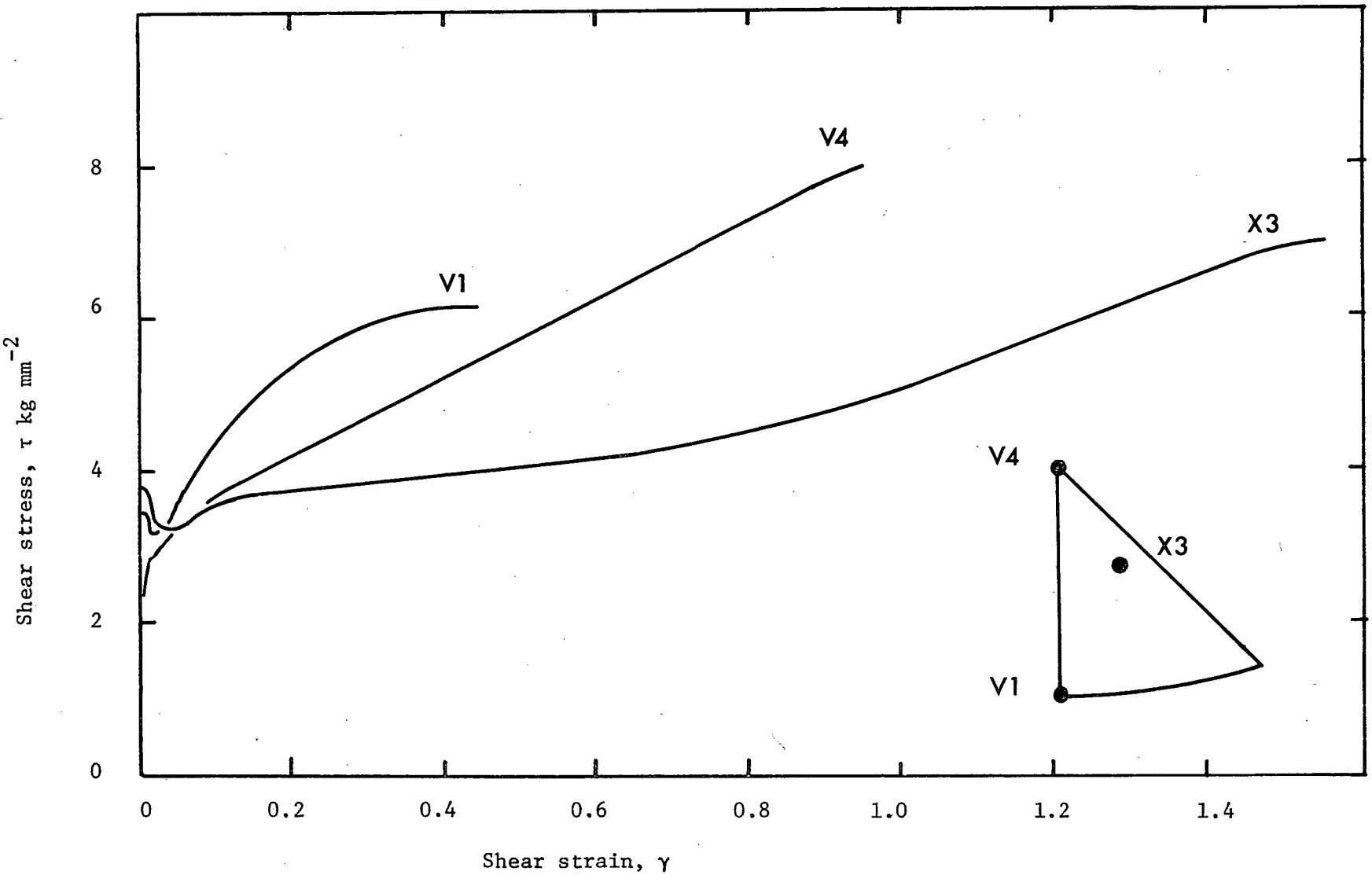

Fig 2. Flow curves at 295°K for pure Nb crystals in different orientations.

found that slip could always be described as taking place on a plane of the type {110} or {112}. If slip takes place on a plane having the highest resolved shear stress, and the critical resolved shear stress is the same for both types of plane, then the regions in which the different slip systems should operate (see A.3) would be as shown in Fig 3. Also shown in the figure is the direction of motion of the tensile axis during straining of three representative crystals. This motion illustrates that the predicted Burgers vector is operative, although the observed slip planes are not precisely of the type {110} or {112}. For this reason, the operative slip planes in this work are described more generally in terms of the slip plane parameter ψ, defined as the angle between the observed slip plane and the (011) reference plane (Fig 3).

An orientation in the middle of the stereographic triangle was selected for all the alloy crystals. This case was the simplest and allowed a considerable amount of slip on a single system, with a $[1\bar{1}1]$ Burgers vector.

3.3 Effect of temperature

The marked increase in strength at low temperatures is the most obvious feature of bcc deformation. Fig 4 shows flow curves at different temperatures; it is clear that both the form of the curve and the stress level are changed. This makes it difficult to compare yield parameters; the yield stress, τ_o, is obtained by extrapolating the load-elongation curve in the linear region following yield back to zero plastic strain. The marked variation of τ_o with temperature is shown in Fig 5 and, for comparison, the data obtained by Duesbery (1967) and Ravi and Gibala (1969) is included. The lower values can be attributed to the higher purity of material used by these workers.

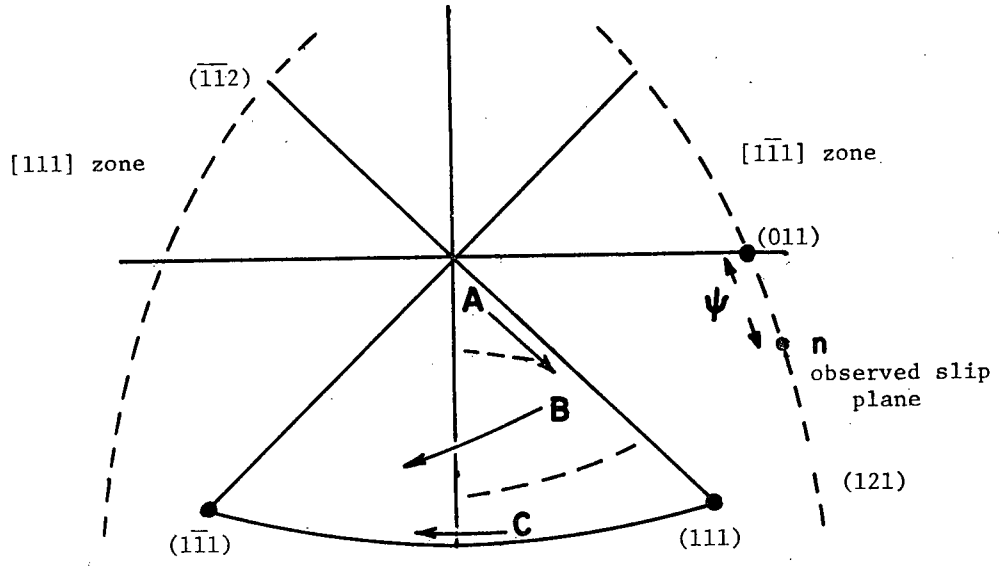

Region	Observed slip system, [b] ψ
A	[111] -28
B	[1$\bar{1}$1] -8
C	[1$\bar{1}$1] 28

Fig 3. Orientation dependence of slip systems.

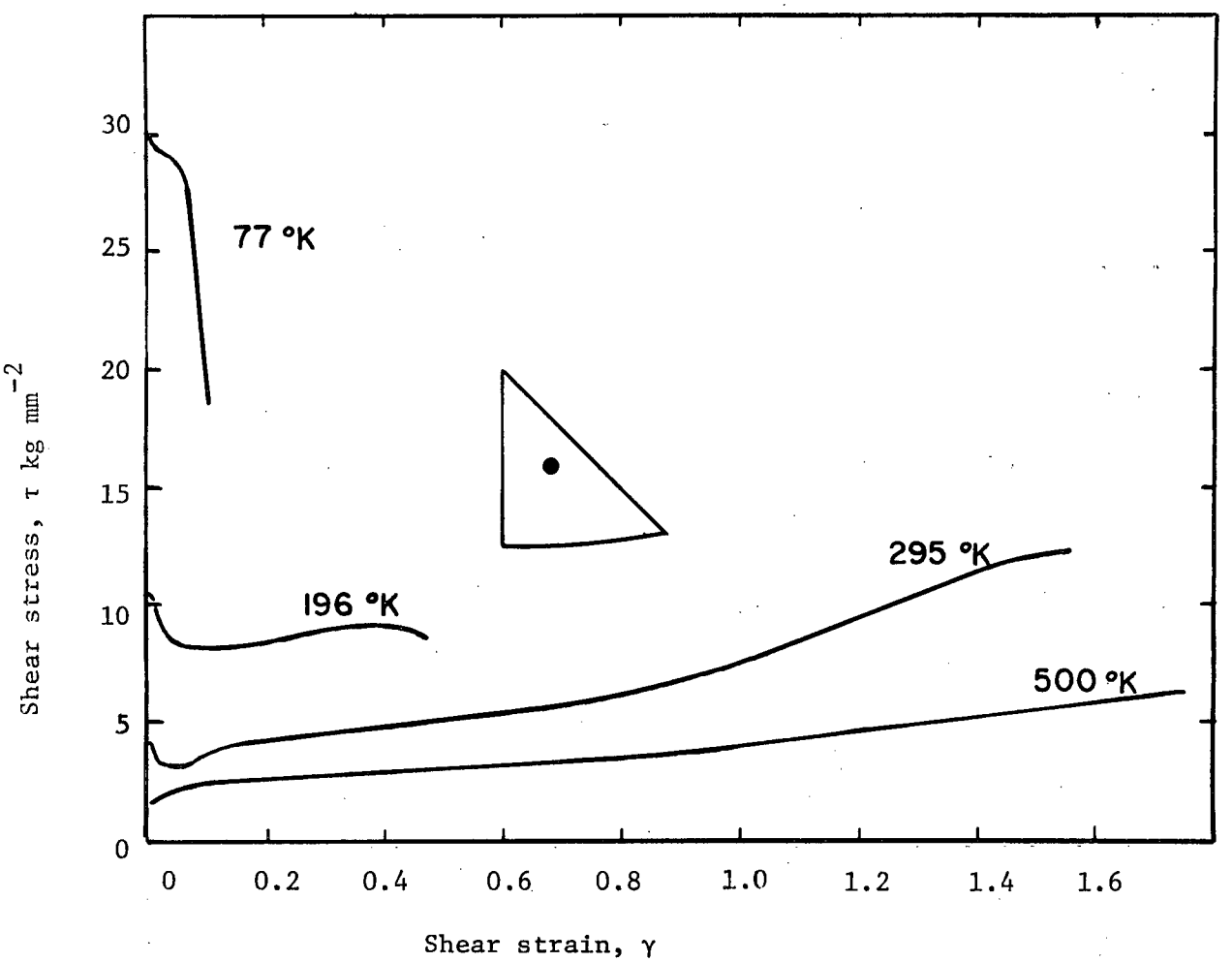

Fig 4. Flow curves for Nb crystals at different temperatures.

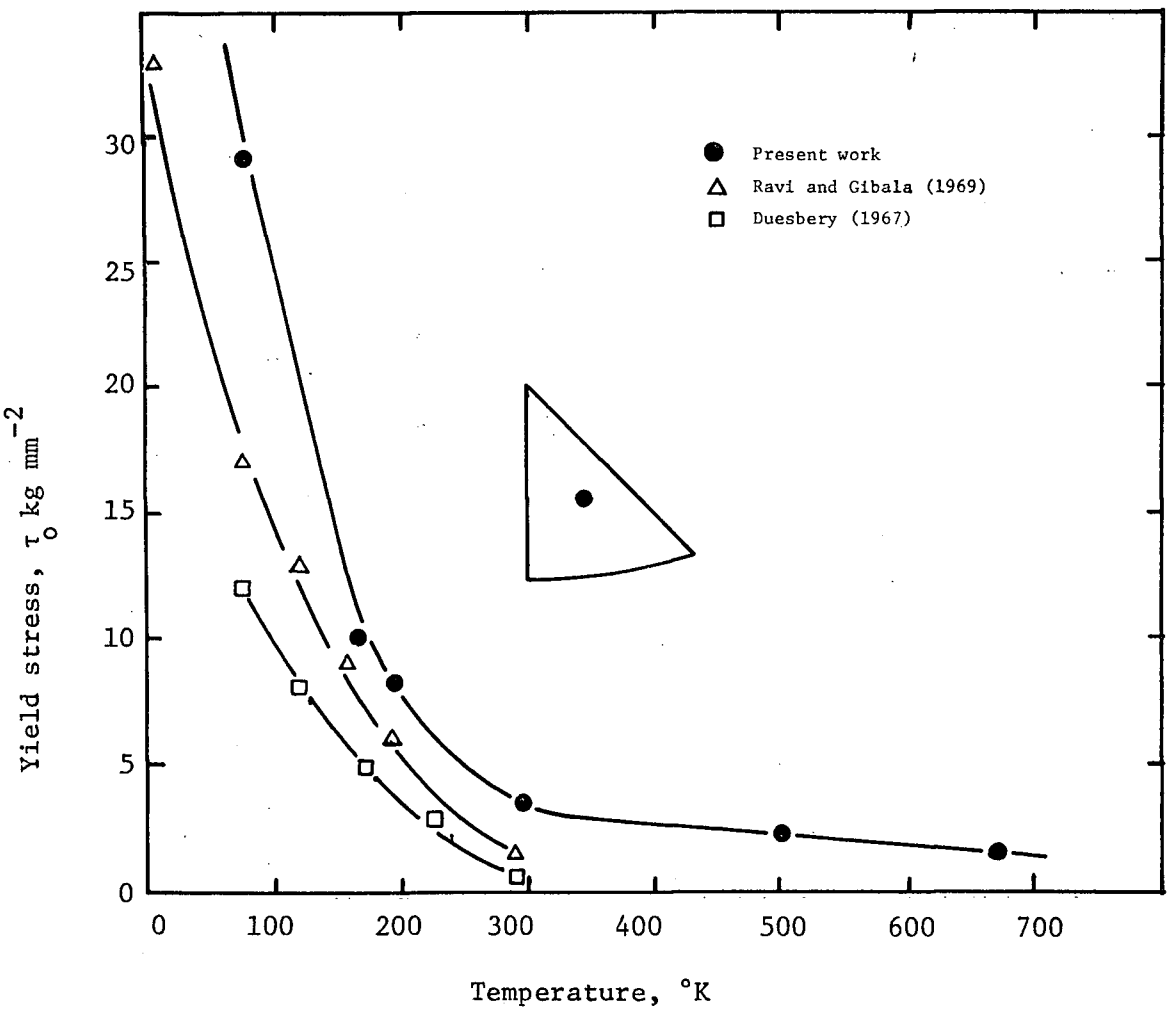

Fig 5. Variation of yield stress with temperature for Nb crystals of different purities.

At room temperature and up to about 450°K, a curve resembling the fcc three-stage curve is observed for orientations within the stereographic triangle. The flow curve for the specimen in Fig 2 is typical. Following the convention established for fcc crystals, the curve is divided into distinct regions:

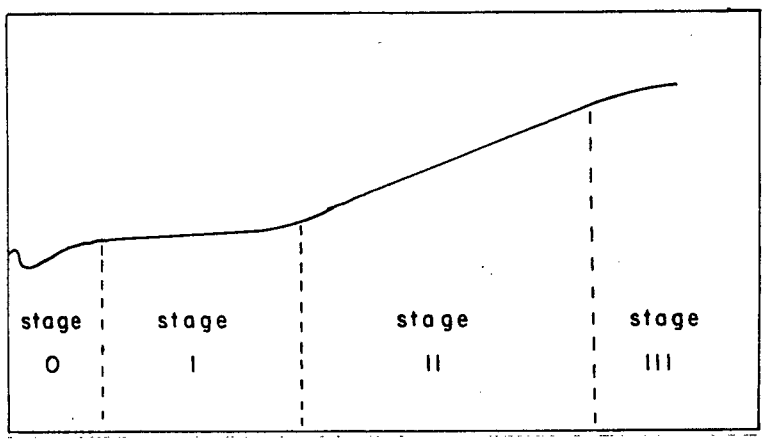

Stage 0 ($\gamma<0.1$) consists of an upper yield point and yield point extension. Stage I ($0.1<\gamma<0.3$) and stage II ($\gamma>0.3$) are linear and fairly distinct. Plastic instability occurred soon after the end of stage II (ie stage III was very small).

The form of the observed flow curve is very dependent on temperature; in particular the following effects are observed in crystals of similar orientation as the temperature is reduced:

a) yield and flow stresses are increased

b) elongation to failure is reduced

c) upper yield becomes more pronounced

d) deformation becomes unstable directly after yield.

3.4 Effect of strain-rate

Mitchell et al (1963) deformed as-grown Nb crystals at room temperature using strain-rates between 1×10^{-1} and 4.5×10^{-6} sec^{-1}, and found that the effect was similar to a decrease in temperature. Their results have been confirmed here over a smaller range of strain-rates: an increase in the nominal strain-rate of an order of magnitude at room temperature increases the yield and flow parameters by about 20%.

Because of the importance of prestraining the crystals before microstrain testing, the strain-rate sensitivity of prestrained crystals was investigated. Crystals were prestrained into stage I and deformed at 295°K and 140°K at various strain-rates. The values of the flow stresses are shown in Fig 6, which also includes the yield stress data of Mitchell et al for as-grown crystals.

At small plastic strains, or if localized yielding occurs, the actual plastic strain-rate might differ considerably from the nominal value (see 5.2.3). The crosshead speed selected for all the alloy tests was 0.005 in min^{-1}, because it was suitable for both micro and macrostrain testing. The corresponding nominal strain-rate was 1.0×10^{-4} sec^{-1}.

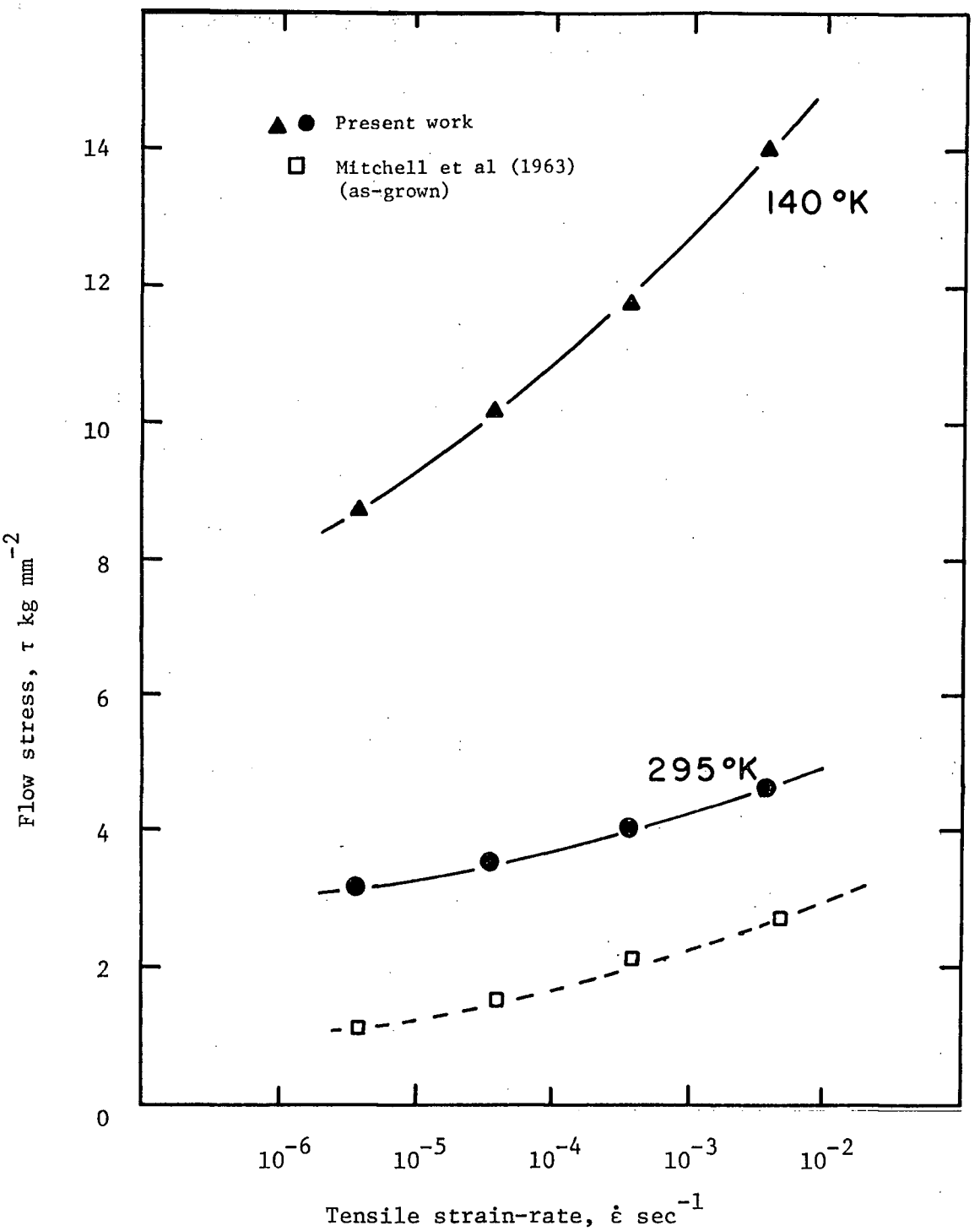

Fig 6. Strain-rate sensitivity of Nb crystals prestrained into stage I.

4. MACRODEFORMATION OF NIOBIUM ALLOY CRYSTALS

4.1 Tensile behaviour at 295°K

Macrostrain tensile tests were performed on specimens of pure MRC Nb and dilute alloys of Nb with Mo and Ta. All the crystals were oriented in the middle of the standard stereographic triangle. Specimens were taken from different parts of the same crystal and from different crystals of a particular alloy. The initial yield was observed with an Instron extensometer and the whole flow curve established from the Instron chart recorder. In many cases, the operative slip systems were determined.

4.1.1 Yield points

4.1.1.1 Results

All the crystals showed an upper and lower yield point at 295°K. In all normal cases, the yield point was well-rounded with about $\gamma = 0.5\%$ pre-yield microstrain. There were differences in the magnitude of the yield drop, $\Delta\tau$: a small variation among specimens of a given alloy but a large variation among different alloys.

For any given alloy, the value of $\Delta\tau$ was very dependent on the local conditions of yield: $\Delta\tau$ was largest in specimens having the greatest variation in diameter along the gauge section. This behaviour differs from that expected from considerations of the mobile dislocation density (Hutchison (1963)). It was also found that $\Delta\tau$ showed a correlation with the magnitude of the upper yield stress τ_{uy}, but not with the lower yield stress $\tau_{\ell y}$. This means that, for a particular alloy, specimens which had a rather high

upper yield stress subsequently exhibited a rather large yield drop.

There was a large difference in the absolute yield drop $\Delta\tau$ of different alloys although the relative yield drop $\frac{\Delta\tau}{\tau_{uy}}$ remained fairly constant ($\sim$5%). The mean value of $\Delta\tau$ for all the alloys tested, together with the standard deviation, is shown in Fig 7. In both alloy systems there is an initial increase in $\Delta\tau$ which levels off at higher concentrations.

Direct evidence for non-uniform yielding was obtained in two cases when the point of minimum specimen diameter lay outside the extensometer gauge length. In these cases the load passed through a maximum before any plastic strain was recorded. Plastic strain was observed when the oncoming Luders front moved into the extensometer gauge length. Because of the inhomogeneous nature of yield, the representation of the flow curve in stage 0 is not very meaningful. However the length of stage 0 was always about γ = 10%, which suggests that at the beginning of stage I all the crystals were in the same physical state whatever the details of yield.

4.1.1.2 Discussion

4.1.1.2.1 Dynamical theory

A dislocation dynamics approach has been successfully used in recent years to explain many of the features of yielding in bcc metals (Hahn (1962), Cottrell (1963), Stein (1968)). The theory explains the yield drop in terms of the initial density of mobile dislocations and their subsequent velocity and multiplication characteristics. However the theory contains so many unknown parameters that it is possible to fit a calculated stress-strain curve to virtually any observed yielding behaviour.

The dynamical approach was taken by Szkopiak (1966) to explain

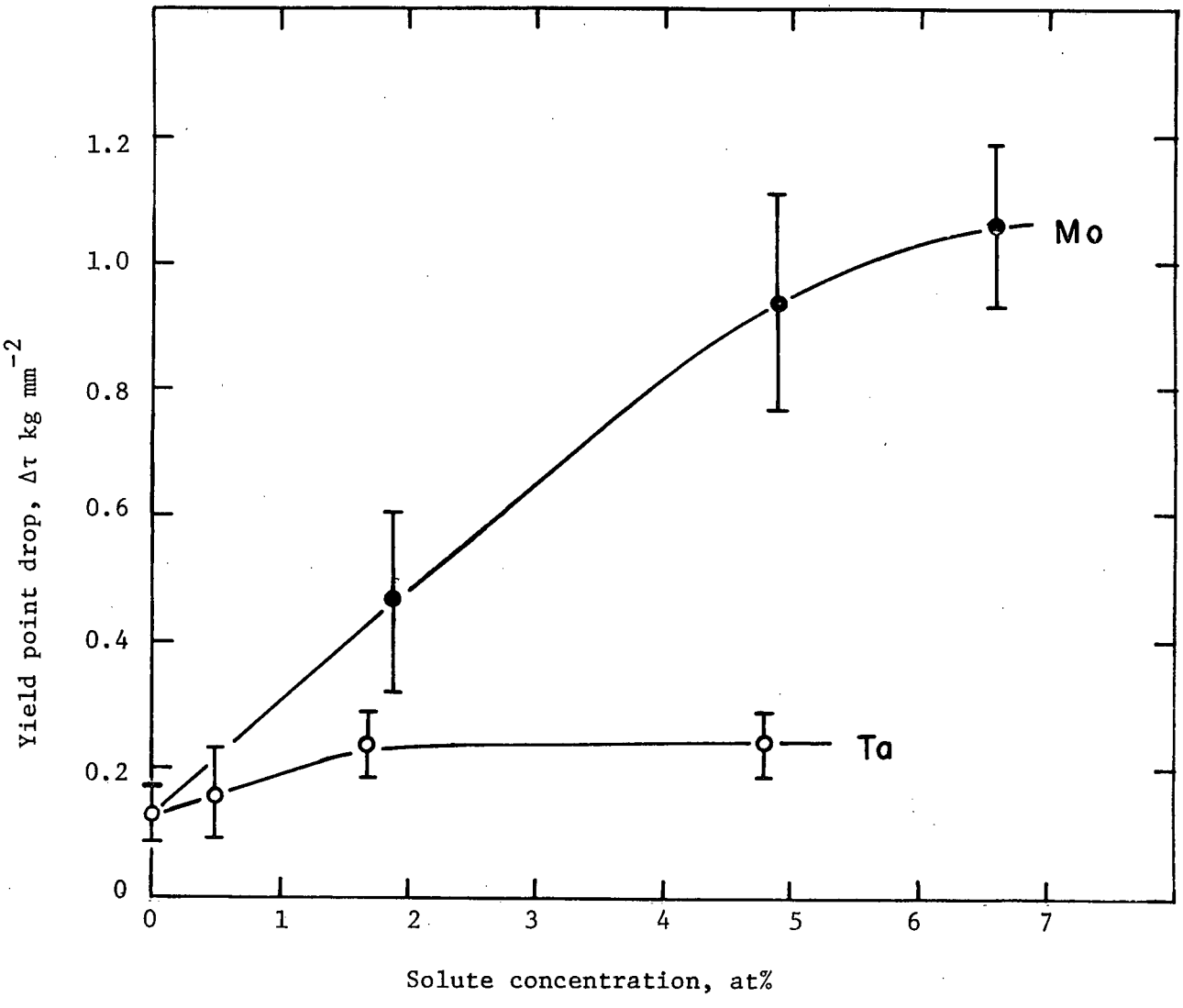

Fig 7. Variation of yield point drop with addition of solute in Nb alloys.

the linear increase of yield point drop with added solute observed in polycrystalline NbO alloys containing up to 800 ppm oxygen. According to this theory, an increase in $\Delta\tau$ could be largely due either to a decrease in the density of mobile dislocations or to an increase in the dislocation velocity exponent with increasing oxygen concentration. Since the dislocation velocity exponent obtained from strain-rate sensitivity experiments was observed to decrease as the oxygen content increased, the observed yield point behaviour was explained by Szkopiak in terms of a reduction in the initial mobile dislocation density.

In the case of substitutional solid solutions there is no reason to expect any marked reduction in the mobile dislocation density with alloying. It is possible that the dislocation velocity exponent might be decreased by addition of substitutional solute, but there is no way of testing this supposition. It therefore appears that, while the dislocation dynamics approach might be capable of describing the yield point behaviour in pure Nb, it cannot usefully be applied to substitutional alloys. Its applicability to this work is further limited because it assumes that yielding is uniform and that no pre-yield microstrain occurs.

Since yielding in pure Nb was observed to be non-uniform, the following theory, based simply on the stability of the initial plastic region, has been developed to predict the dependence of the yield drop on the magnitude of the yield stress and true work hardening rate. It is a continuum approach and its applicability derives from the general nature of discontinuous yielding in both crystalline and non-crystalline materials.

4.1.1.2.2 Stability theory

It is to be expected that the work hardening characteristic of

a material will influence the nature of the yield point. However, since deformation in the region of an upper yield point is far from uniform, the true work hardening rate cannot be obtained from the observed load versus elongation curve. In fact, in the elastic region, the apparent work hardening rate is infinite and after the upper yield point the material is apparently work softening. A more useful definition has therefore been adopted for the "true work hardening rate", Ω. This is supposed to be an intrinsic material parameter, definable in principle, if not in practice, as a function of past history, strain, and strain-rate. The true work hardening rate can be defined only for that region of the material which deforms homogeneously. In the case of the discontinuous yielding observed during tensile deformation of Nb crystals, it refers to the plastic nucleus forming an incipient Luders band.

Consider a nucleus of length x and of volume V which is assumed to be constant. Under a load L, the nucleus extends plastically by an amount dx in time dt:

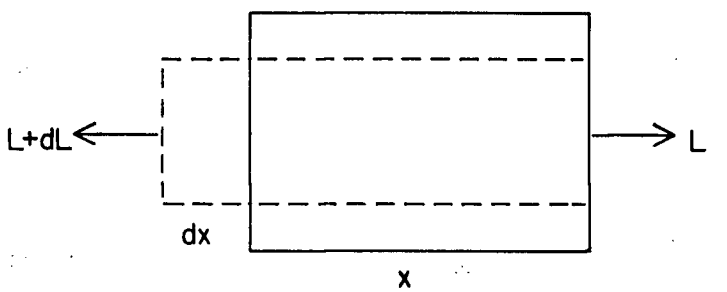

Then the true work hardening rate is defined by

$$\Omega = \frac{d\left(\frac{L}{A}\right)}{\frac{dx}{x}} \qquad (1) \qquad \text{cf } \frac{d\sigma}{d\varepsilon}$$

where A is the instantaneous cross-sectional area given by

$$A = \frac{V}{x} \qquad (2)$$

If the crosshead velocity is $\dot{X}$ and elastic effects are neglected,

$$dx = \dot{X}.dt \qquad (3)$$

provided the plastic nucleus is the only region that deforms.

Substituting (2) and (3) in equation (1) gives

$$\Omega = \frac{x}{V.\dot{X}} \frac{d}{dt} (L.x)$$

or $$\Omega = \frac{x}{V} \left[L + \frac{x}{\dot{X}} \left(\frac{dL}{dt}\right) \right] \qquad (4)$$

From this definition, it can be seen that in the elastic region since $x = 0$, Ω is zero; after yield Ω can still be positive even though the load is decreasing.

It will now be assumed that yielding occurs suddenly at a load L_o and that after yield, Ω is constant. Equation (4) can be used to predict the subsequent flow behaviour (ie $\frac{dL}{dt}$) for given values of L_o and Ω.

The critical condition for the plastic nucleus to be stable is given by

$$\frac{dL}{dt} = 0$$

Therefore $$\Omega = \frac{x.L_o}{V} = \sigma_o \qquad \text{(cf Considères criterion)}$$

where σ_o is the true tensile stress at yield.

If $\Omega > \sigma_o$, deformation will be stable. In this case, there will be no yield drop and x must be identified with the specimen gauge length.

For $\Omega < \sigma_o$, deformation will be unstable and Fig 8 shows the predicted initial forms of the load versus time curves, for three different true work hardening rates. Values for the constants are typical of this work. The actual magnitude of the total yield drop will depend significantly

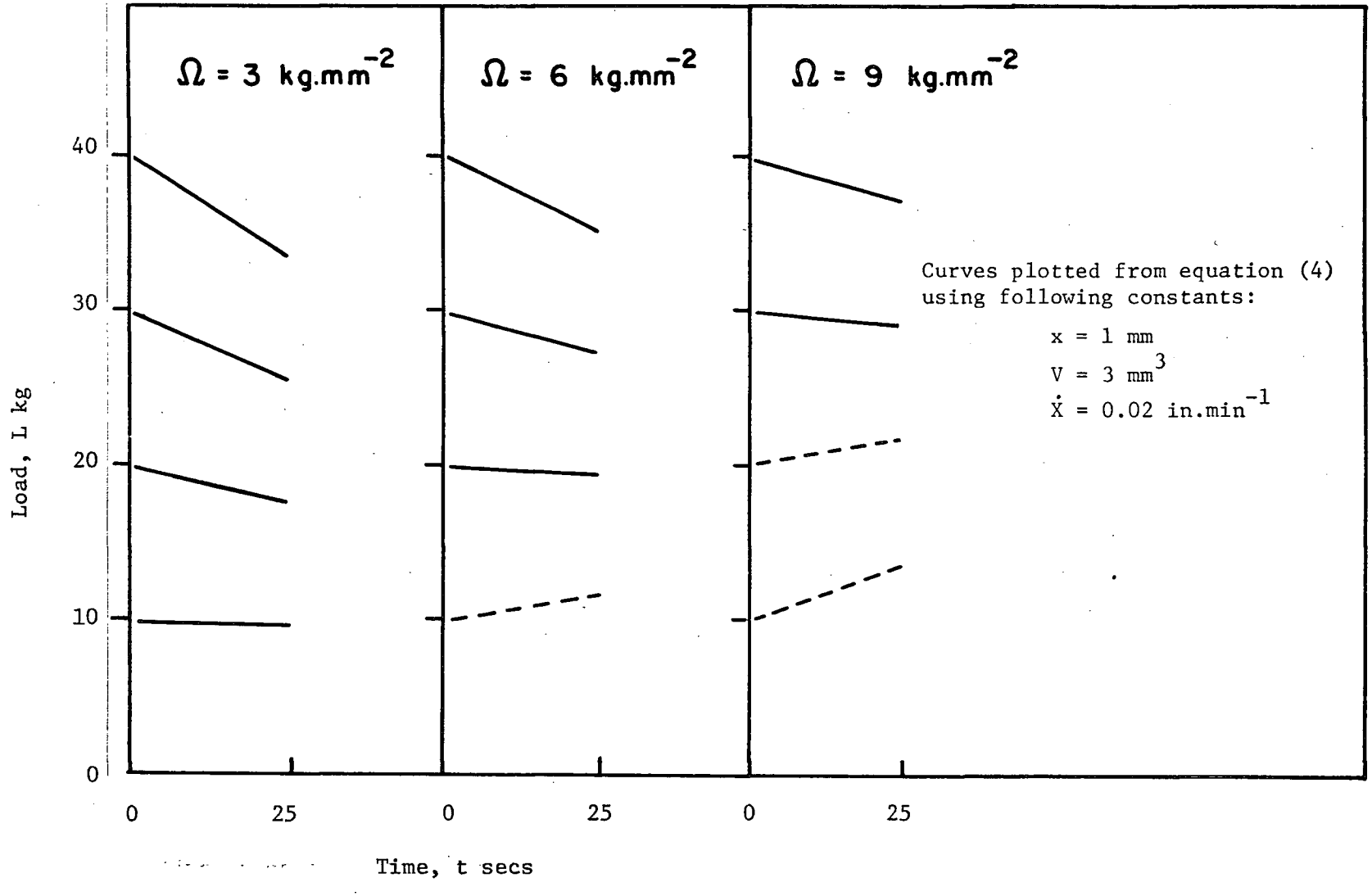

Fig 8. Predicted form of initial yield drop as a function of yield load and true work hardening rate.

on the elastic properties of the tensile testing apparatus, and on the change in Ω with strain and strain-rate. However the trend is quite clear from Fig 8: if there is no significant change in true work hardening rate, then the expected yield drop is greater in those crystals having the higher yield stress. It will be seen in the next section that alloying of Nb produces a large increase in yield stress without much effect on the work hardening parameters. Therefore, for the substitutional alloys examined here, the stability theory has explained the increase in yield drop with increasing solute content shown in Fig 7.

In the case of dispersion hardened alloys it is expected that the work hardening rate will be increased significantly without much effect on the yield stress. In this case the theory predicts a decrease in yield drop with increasing alloy content as can again be seen from Fig 8. This behaviour has recently been observed in $Fe.ThO_2$ alloys (Place (1969)).

After yield, the values of L and $\frac{dL}{dt}$ in equation (4) are indeterminate, but $\frac{dL}{dt}$ will increase and may reach zero while L is still positive. In this case, the Luders band will become stable and spread along the specimen. This was the usual case with pure Nb and NbTa alloys. However, in cases where $\frac{dL}{dt}$ at yield is large and negative, it is possible that L will fall to zero while $\frac{dL}{dt}$ is still negative. This situation corresponds to a Luders failure, and was observed in the high Mo alloys as mentioned below.

The success of the simple stability theory indicates that the importance of dislocation multiplication may have been overstressed in the past. It is suggested that the dislocation dynamics approach and the stability approach represent two different aspects of discontinuous yielding. Cases in which discontinuous yielding is uniform (eg LiF) must be expressed

in terms of dislocation dynamics. However in cases where yielding is non-uniform, the stability approach clearly makes an important contribution.

4.1.2 Flow curves

4.1.2.1 Results

Fig 9 shows the computed flow curve for a Nb 4.8 Ta crystal. It is very similar to the pure Nb flow curve; no differences in form were observed with any of the Ta alloys.

Deformation appeared completely uniform except for the initial discontinuous yield. The yield stress, τ_o, was obtained by extrapolating the flow curve in stage I back to zero plastic strain. The important parameters of the Ta alloy flow curves are shown in Fig 10. The effect of Ta on τ_o is most noticeable at small concentrations but is never very marked. There is possibly an accompanying slight increase in θ_{II}, but no definite effect of Ta on the work hardening parameters is evident. The order of magnitude of θ_I and θ_{II} is indicated.

In the case of the NbMo alloys the hardening effect was much greater than in the NbTa alloys; deformation was observed to become increasingly non-uniform as the Mo content increased. For this reason, the tensile results for the NbMo alloys are shown in Fig 11 as conventional stress versus conventional strain curves. The variation of τ_o with Mo content is shown in Fig 12. It can be seen that the hardening is linear, with a slope of 2.1 kg mm^{-2} $at\%^{-1}$. The hardening effect of Mo is therefore about 35 times greater than that of Ta, for which the corresponding slope is only 0.06 kg mm^{-2} $at\%^{-1}$ in the linear region after the initial rise.

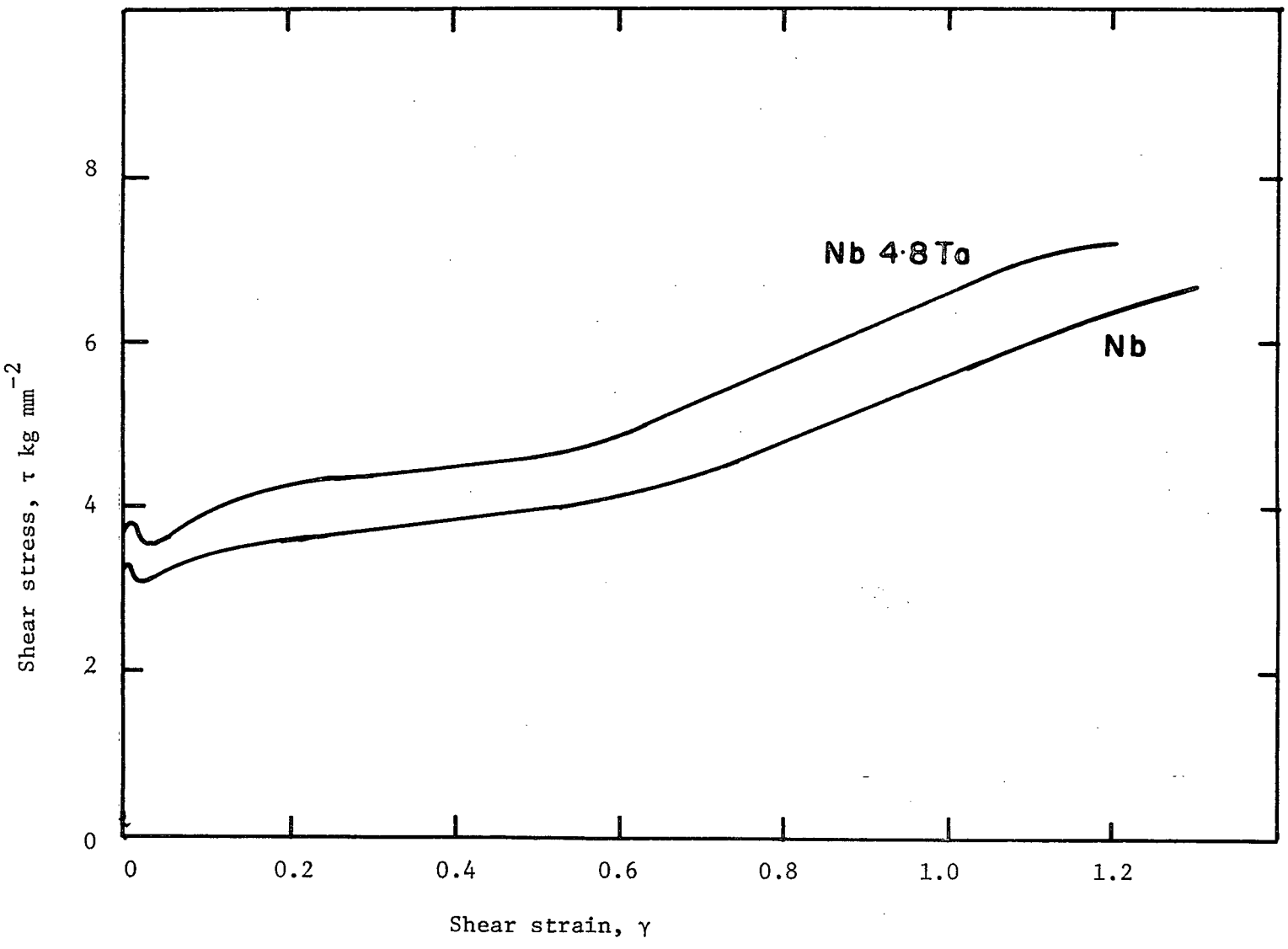

Fig 9. Flow curves for Nb and Nb 4.8 Ta crystals at 295°K.

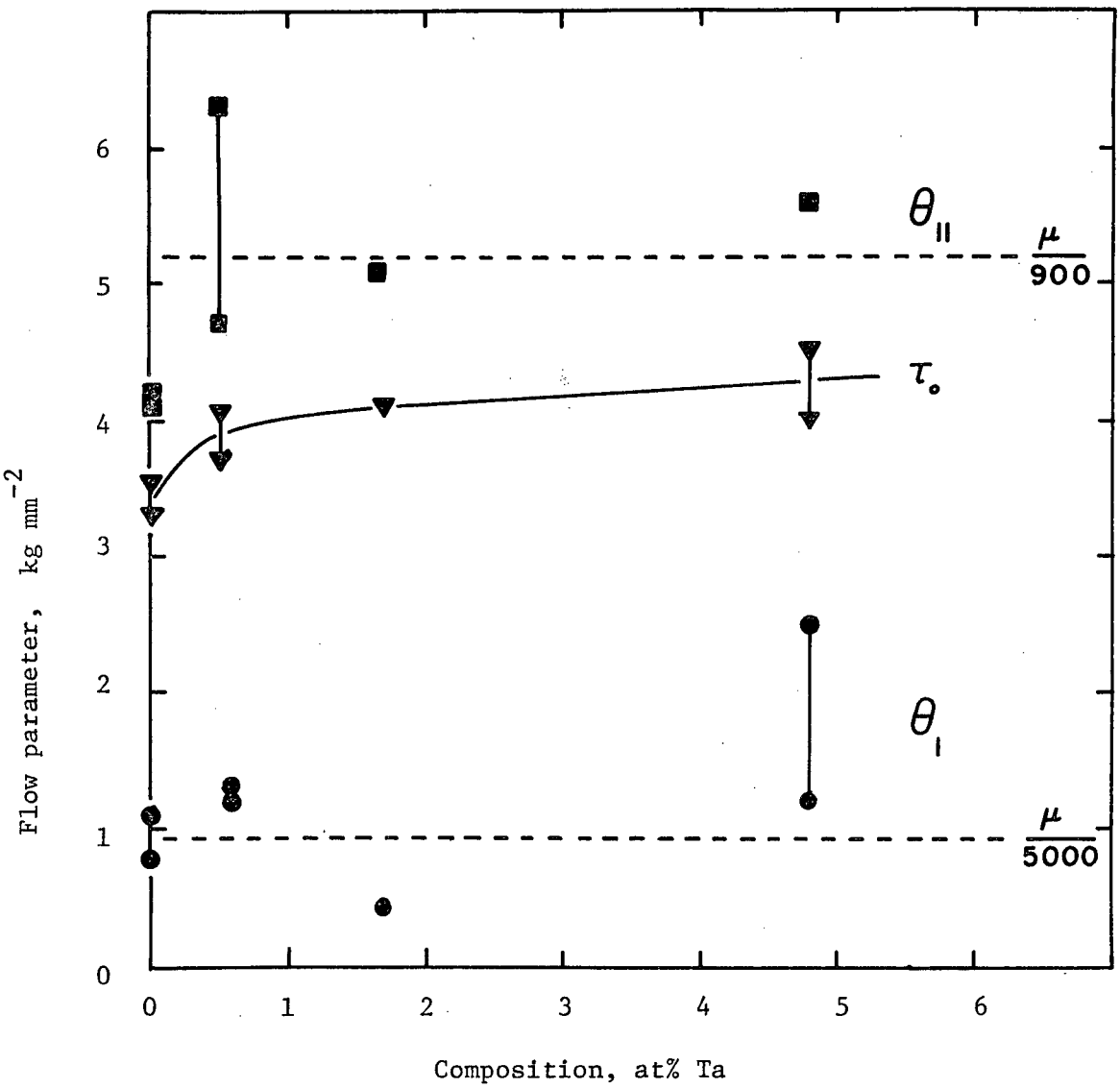

Fig 10. Flow parameters for NbTa alloys deformed at 295°K.

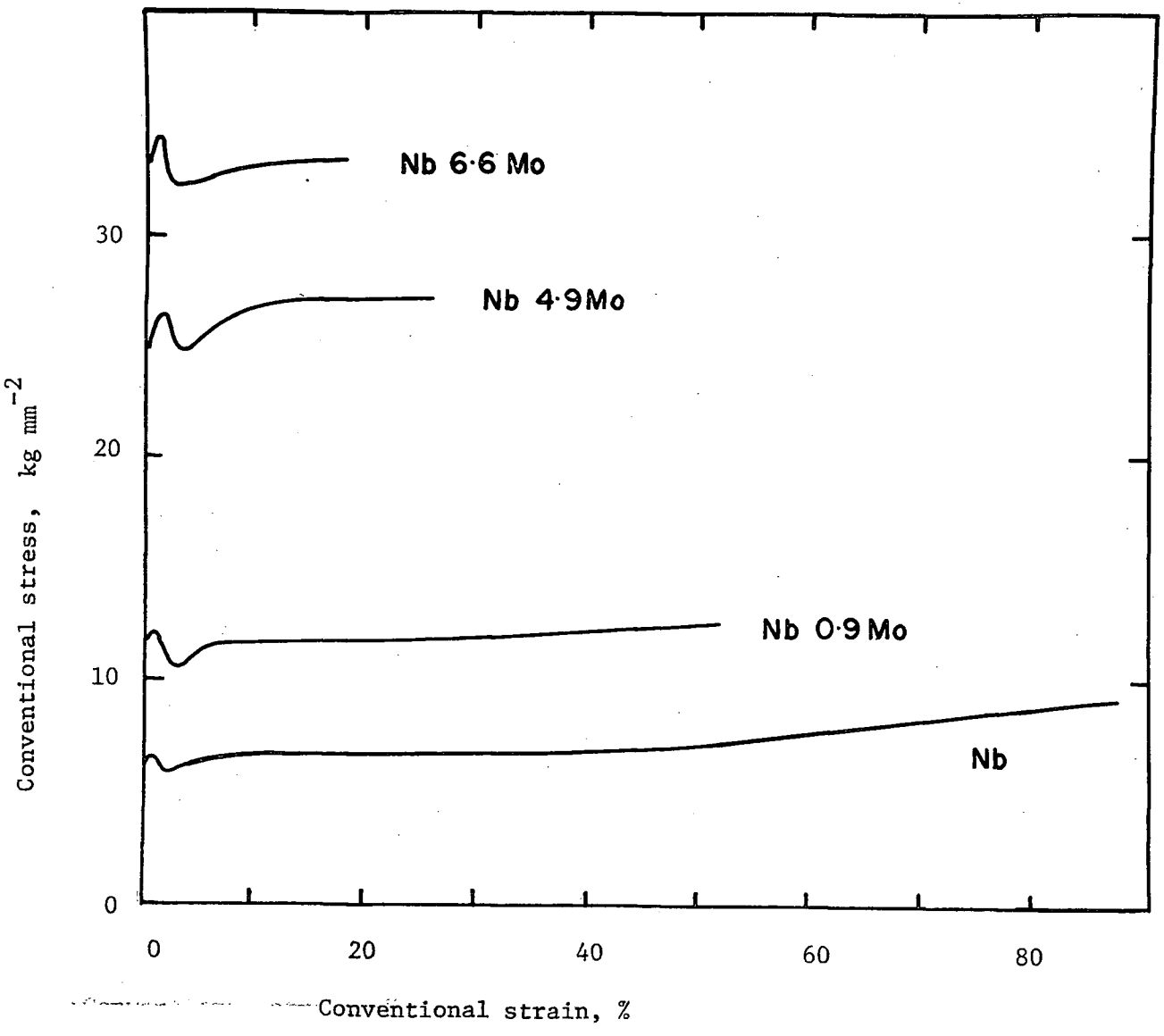

Fig 11. Conventional stress - conventional strain curves for NbMo alloys at 295°K.

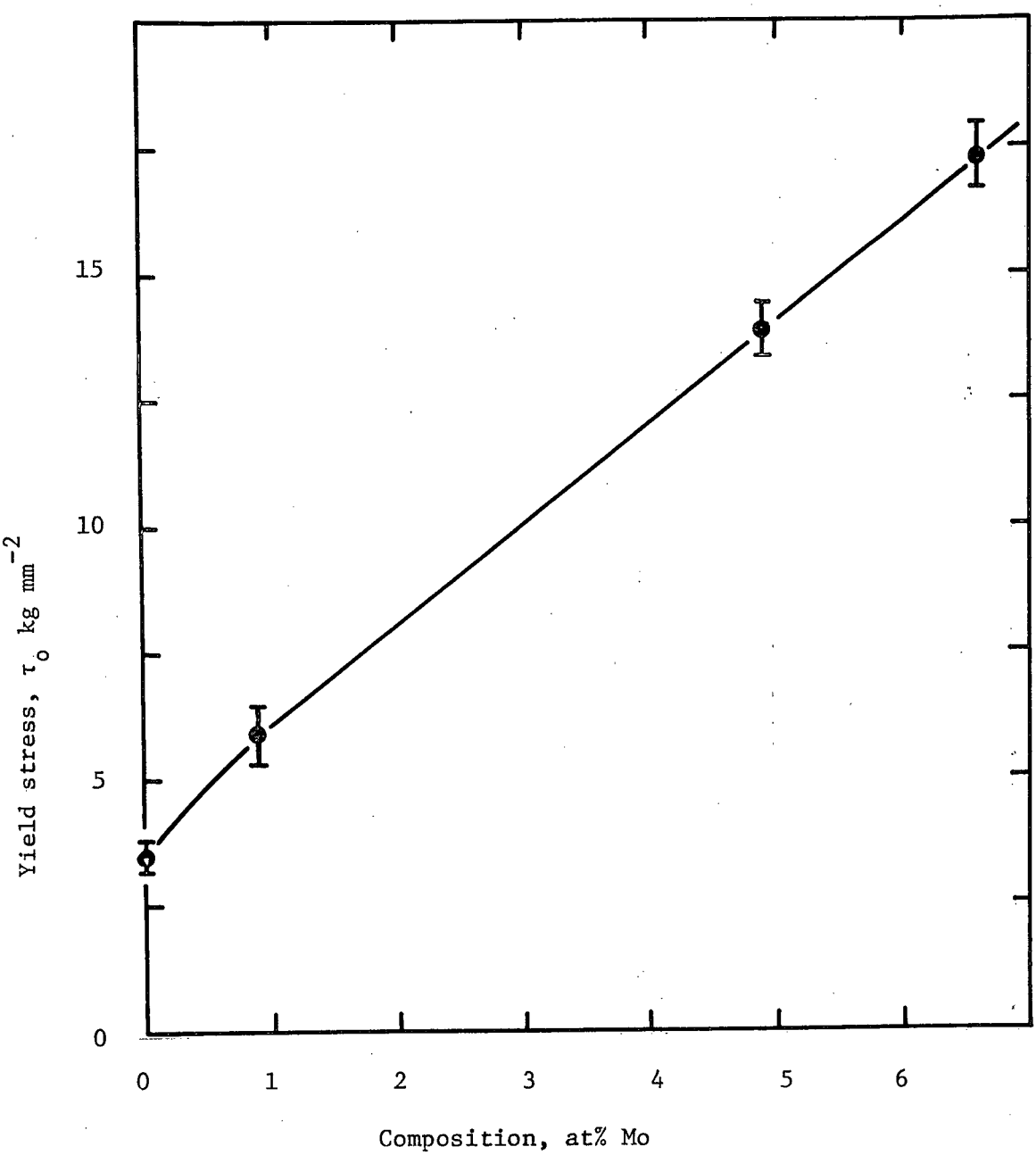

Fig 12. Yield stress of NbMo alloys deformed at 295°K.

4.1.2.2 Discussion

4.1.2.2.1 Uniformity of deformation

It was shown above that a condition for deformation at yield to be stable is

$$\Omega \geq \sigma_o$$

After the initial perturbation at yield, the same criterion should apply, and if deformation does subsequently remain uniform then Ω is given by $\frac{d\sigma}{d\varepsilon}$, which can be obtained from the observed flow curve $\sigma(\varepsilon)$. At any stress σ, the stability condition therefore becomes

$$\frac{d\sigma}{d\varepsilon} = \sigma$$

In terms of $\tau(\gamma)$, since

$$\sigma = \frac{\tau}{s}$$

$$\varepsilon = s.\gamma$$

the condition is given by

$$\frac{d\tau}{d\gamma} = \theta = s.\tau$$

where θ is the slope of the flow curve and the Schmid factor s is approximately constant ($\sim$0.5) during flow.

Consider Fig 13 which is an idealized flow curve $\tau(\gamma)$ for a Nb single crystal, obtained under conditions of uniform flow. This curve can also be expressed as a plot of $\tau(\theta)$, shown as case A in the figure. It can be seen that deformation remains stable (ie uniform) until $\tau(\theta)$ crosses the line $\tau = \frac{\theta}{s}$ at a stress τ_{II}, at which point deformation becomes non-uniform.

The form of $\tau(\theta)$ can be considered to represent the basic response of the material to deformation. This response will only be obtained in a tensile test if deformation remains stable,

$$\text{ie} \quad \theta > \sim \frac{\tau}{2}$$

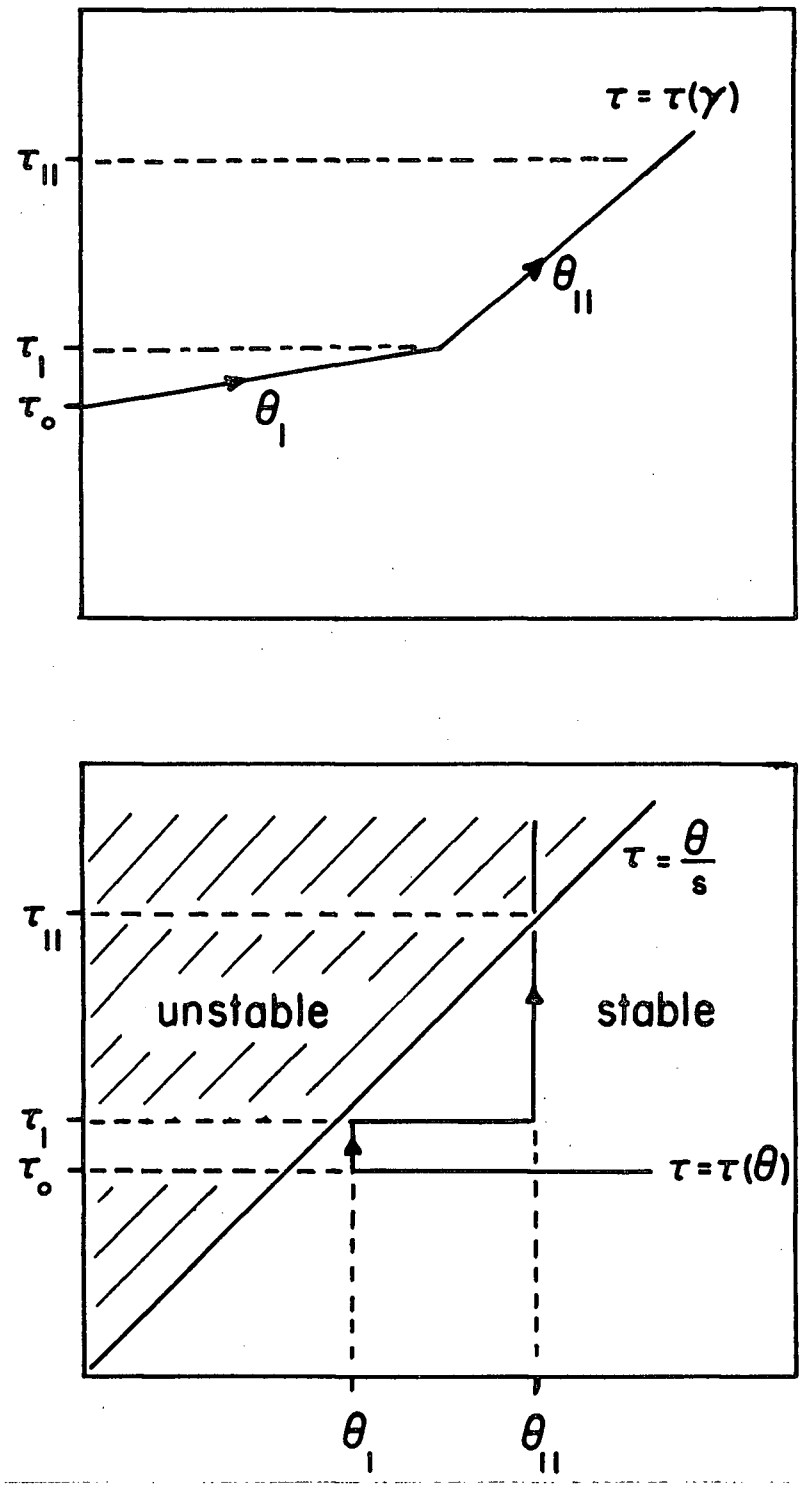

Case A

Fig 13. Idealized flow curve expressed as $\tau(\gamma)$ and $\tau(\theta)$.

For the Nb and NbTa crystals this condition was satisfied in stage II but not always in stage I (Fig 10). There is therefore a possibility that deformation in stage I might have been unstable.

The effect of an increase in alloy content or a decrease in temperature is to increase the level of the flow stress. Unless there is a corresponding increase in the work hardening parameters, deformation may become unstable at a much earlier stage as shown by the diagrams in Fig 14.

In case B, necking starts to occur during stage I but the localized onset of stage II stabilizes the neck. Therefore a deformation front will pass down the gauge length during "stage I". The observed work hardening slope in this region is meaningless.

In case C, necking will occur immediately after yield. Deformation will never become stabilized, so a Luders failure will result. Again the observed work hardening slope is meaningless.

For the NbMo alloys, deformation became more non-uniform as the solute content increased, and the behaviour predicted in cases B and C was in fact observed.

It also follows from the stability argument that the total strain to failure will depend on the true work hardening rate rather than on the intrinsic ductility of the material; this is confirmed by observations of the reduction of area at failure, which in all cases was 100%.

Similar considerations can be expected to apply during low temperature deformation.

The arguments which have been expressed above are applicable in principle to both single crystal and polycrystal deformation. However the situation represented by case B can occur only in the deformation of single crystals, because this requires a work hardening rate which increases with strain.

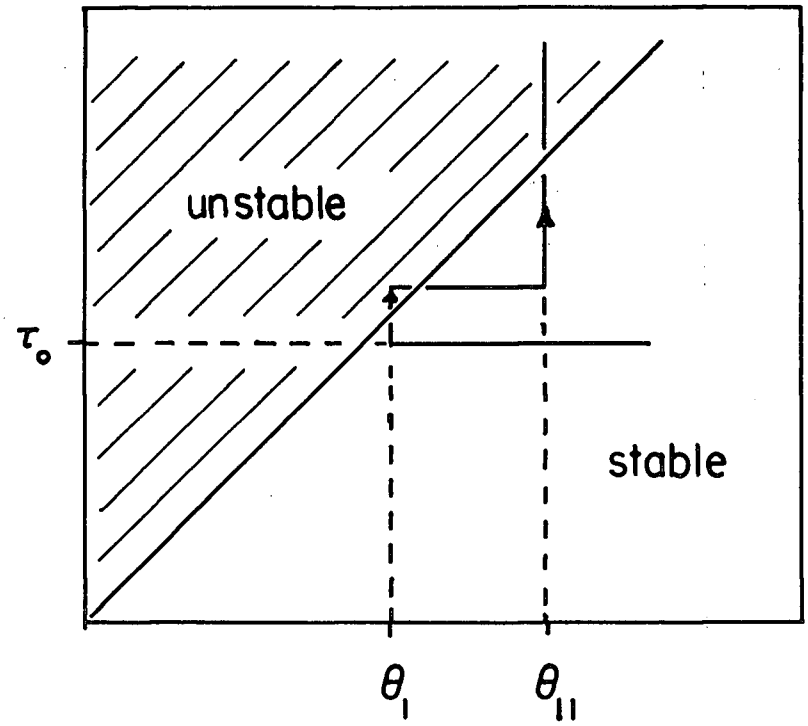

Case B

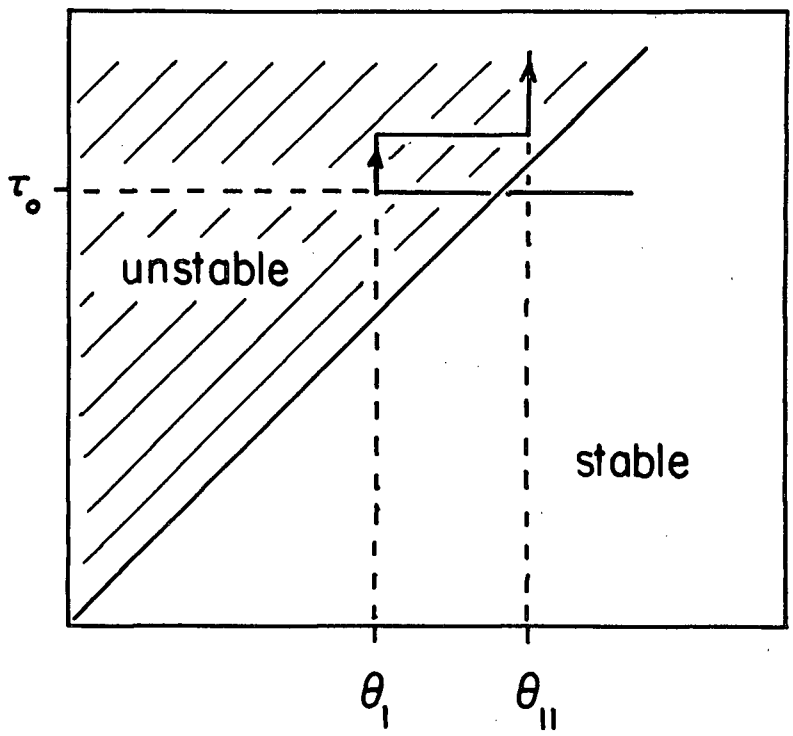

Case C

Fig 14. Effect of increase in yield stress on stability of tensile deformation.

4.1.2.2.2 Flow parameters

Peters and Hendrickson (1966) have obtained critical shear stress data for crystals having a composition range extending from pure Nb to pure Ta; their results are shown in Fig 15a. They obtained a value of 2.5 kg mm^{-2} for τ_o in pure Nb compared with τ_o = 3.4 kg mm^{-2} obtained in this work. The lower value is a consequence of the [001] orientation which they used (Hendrickson (1969)). Their crystals were in general slightly less pure than those used in this study. To facilitate comparison of the hardening effects, 0.9 kg mm^{-2} has been subtracted from the values in Fig 15a to give agreement with the τ_o values for pure Nb in Fig 10.

Peters and Hendrickson claimed that their results indicated a linear variation in τ_o from pure Nb to pure Ta. This gives a hardening rate of 0.023 kg $mm^{-2}at\%^{-1}$, which predicts a hardening of 0.11 kg mm^{-2} in a 5 at% Ta alloy. Since the corresponding increase obtained in this work was 0.9 kg mm^{-2}, it is evident that most of the hardening occurs at low solute concentrations. The data of Arsenault (1969) indicates that addition of Nb to pure Ta at room temperature also produces hardening, so there exists a positive deviation from the linear relationship suggested by Peters and Hendrickson.

A solution hardening study of Nb with Ta has recently been performed by Kostorz (1968). Crystals containing 1.8 at% Ta and 11 at% Ta were deformed in compression between 295°K and 573°K. Kostorz used a different yield parameter and obtained a value of τ_o = 2.2 kg mm^{-2} for pure Nb at 295°K. The yield parameters obtained by him at 295°K are shown as a function of $c^{\frac{1}{2}}$ in Fig 15b and compared with the tensile data obtained in this study, after subtraction of 1.2 kg mm^{-2} to give agreement with pure Nb. The hardening effects are very similar and indicate parabolic

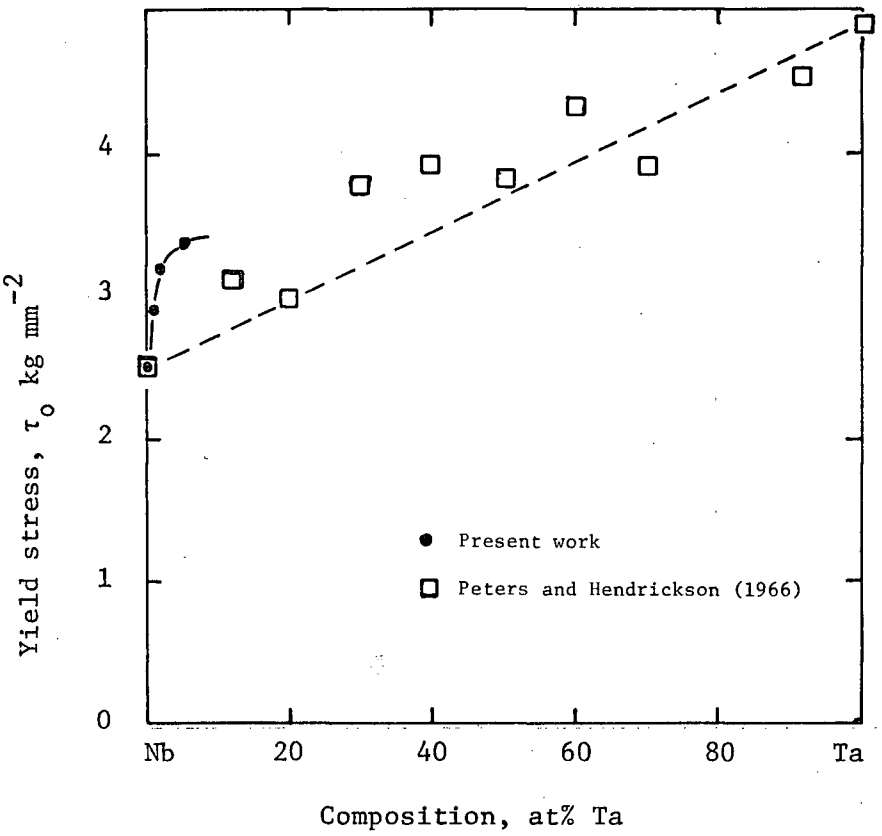

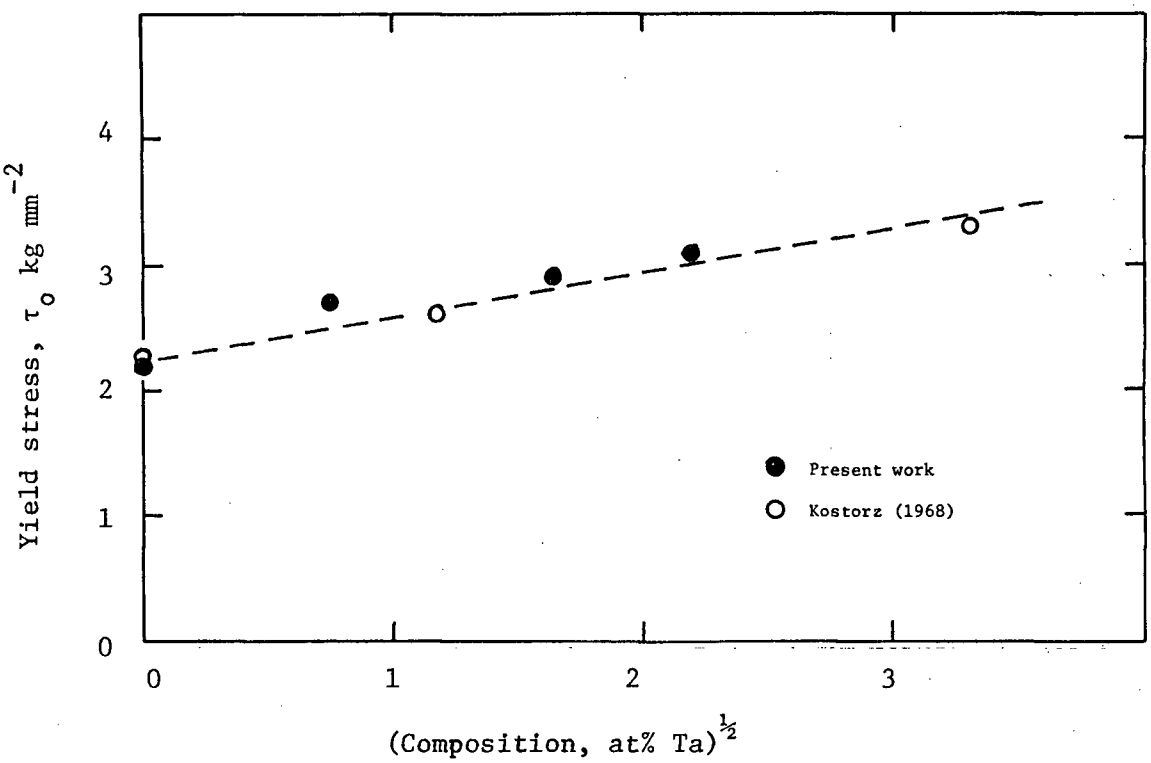

Fig 15. Comparison of yield stress data for NbTa alloys with:
a) linear hardening, Peters and Hendrickson
b) parabolic hardening, Kostorz

hardening, although it should be recalled that the overall effect is small.

Milne and Smallman (1968) have studied the tensile deformation characteristics of NbMo alloys over the complete composition range. Although the crystals were not seeded for a specific orientation, several specimens were oriented in the middle of the stereographic triangle. The values of τ_o for these specimens are shown in Fig 16, together with the results of this study. The values of τ_o for pure Nb are in agreement. The trend observed at low Mo concentrations is seen to continue up to a maximum at the equiatomic composition.

Very few results have been published on the effect of solute on the hardening parameters of bcc metals: most tests have been performed in compression; in tension, alloying usually induces non-uniform deformation, preventing a determination of θ_I and θ_{II}. In the NbTa alloys studied here, deformation did remain uniform so that the hardening results, though limited, are of interest. There appears to be no effect of Ta in the easy glide region; indeed, no solution hardening theory would predict an influence of solute on the hardening rate in stage I. Since solute might influence the operation of secondary systems, there could be an effect on stage II: the results indicate a slight increase in θ_{II} upon alloying. This is in agreement with the very limited data obtained by Arsenault and Lawley (1967) for addition of Nb to Ta at this temperature.

4.2 Tensile behaviour at other than 295°K

The Nb alloys were deformed in tension at temperatures between 77°K and 500°K. Several different modes of plastic deformation were observed: the NbTa alloys deformed by slip at all temperatures, and in addition

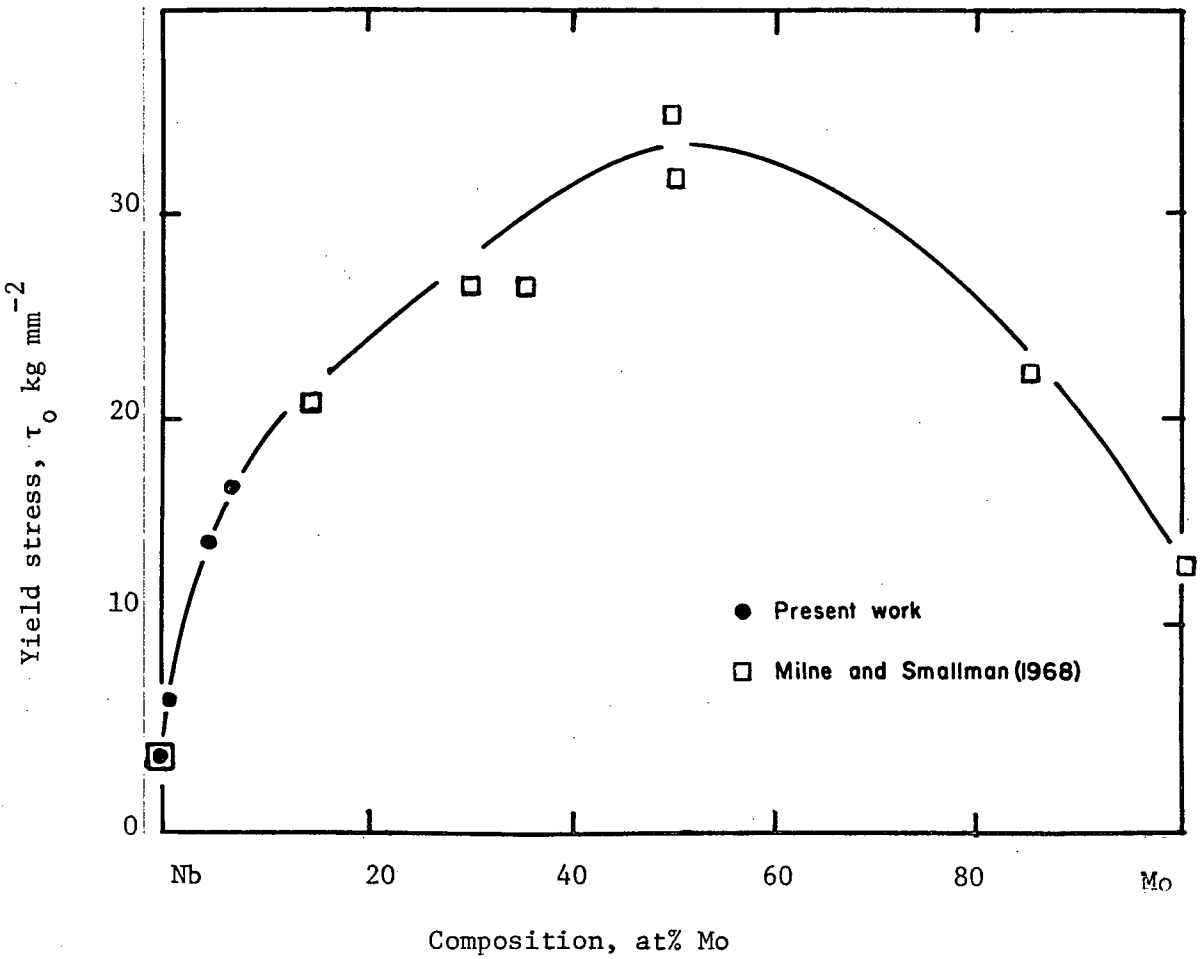

Fig 16. Comparison of yield stress data for NbMo alloys with data of Milne and Smallman.

twinning was common at 77°K; in the NbMo alloys twinning or cleavage failure, without any evidence of slip, always occurred at low temperatures.

4.2.1 Slip

4.2.1.1 Results

Fig 17 shows the values of τ_o obtained at different temperatures for those specimens which showed a detectable amount of plastic flow. In the case of the NbTa alloys at 77°K, τ_o was taken to be the stress at 0.1% shear strain. The curves for Nb 0.5 Ta and Nb 1.7 Ta have been omitted for clarity.

Above room temperature, deformation was uniform and Nb 6.6 Mo was the only alloy to show an upper yield point. At low temperatures, deformation was observed to become increasingly non-uniform: after a large initial yield point, flow often took place under a continuously decreasing load.

It can be seen from Fig 17 that as the temperature is reduced, the NbTa alloys show a transition from solute hardening to solute softening, although the effect is never very marked. There is no evidence for a similar behaviour in the NbMo alloys.

It is customary to divide the $\tau_o(T)$ curve into two regions:

a) a thermal region, where the flow stress is a sensitive function of temperature,

b) an athermal region, where the flow stress τ_μ is relatively insensitive to temperature, and varies in the same manner as the shear modulus, μ .

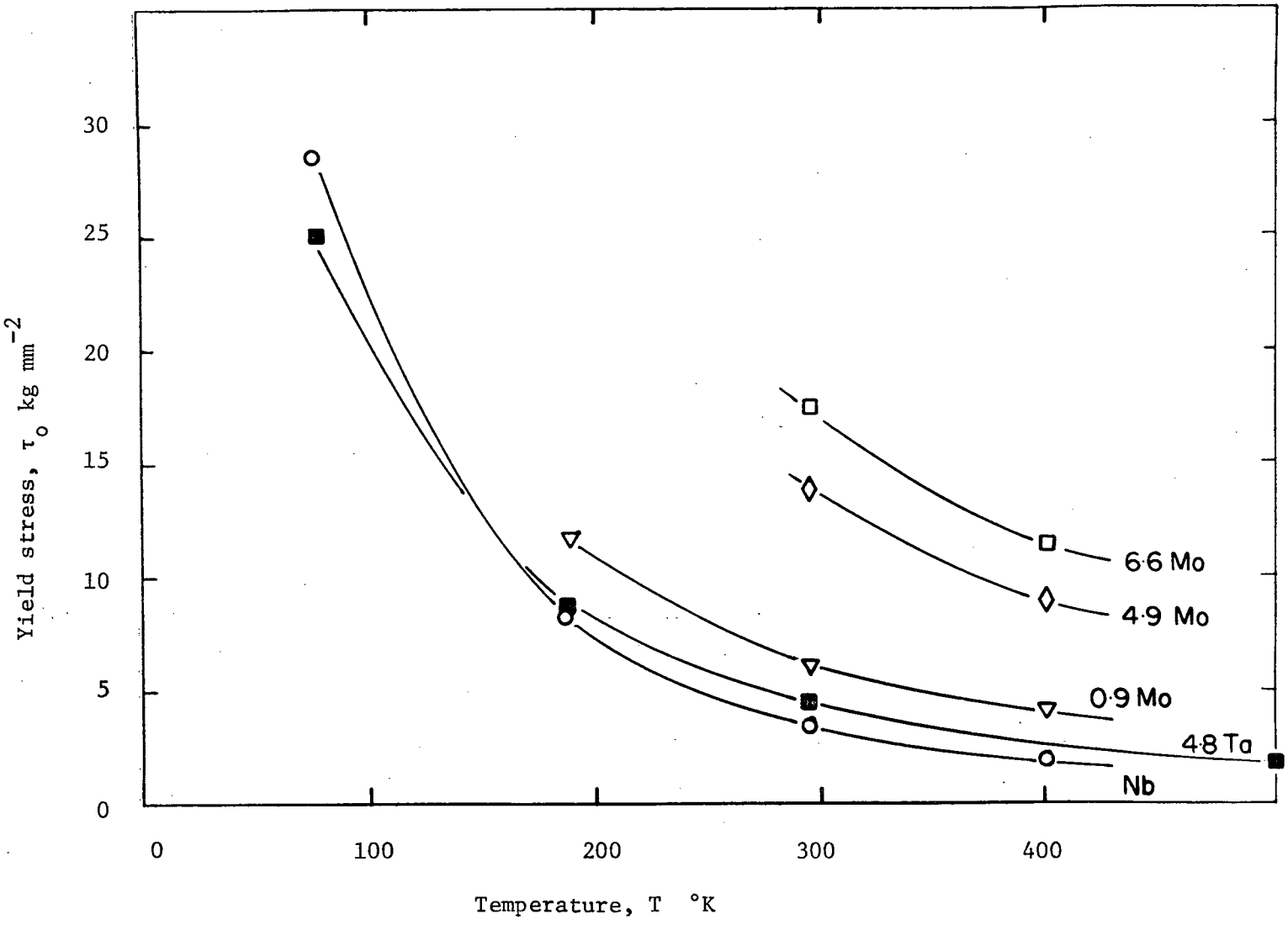

Fig 17. Yield stress as a function of temperature for Nb and Nb alloys.

The components of the flow stress in the thermal region are called the thermal stress τ^* and athermal stress τ_μ. The transition temperature T_o, at which τ^* falls to zero, depends on the mathematical definition used to determine it. Using the condition

$$\frac{1}{\tau}\left(\frac{d\tau}{dT}\right)_{T_o} = \frac{1}{\mu}\left(\frac{d\mu}{dT}\right)_{T_o}$$

the following values for T_o were obtained:

Nb	420°K
Nb 5 Ta	460
Nb 0.7 Mo	500
Nb 6 Mo	550

From Fig 17 it can now be seen that the main effect of alloying is on the overall stress level determined by τ_μ, rather than on the temperature sensitivity of the flow stress determined by τ^*.

At 77°K, two of the six NbTa specimens did not twin before yield so that a complete flow curve was obtained. Flow was wavy right up to the maximum load, as illustrated in Fig 18. The fractured specimen showed a local reduction in area at three places along the gauge. One of these was the fracture site, which showed intense slip and about 90% reduction in area. It is notable that localized failure did not occur after the first upper yield point, and that the specimen was subsequently capable of exhibiting a high work hardening rate.

4.2.1.2 Discussion

4.2.1.2.1 Work hardening and uniformity of deformation

The arguments presented to explain the change of yield point with

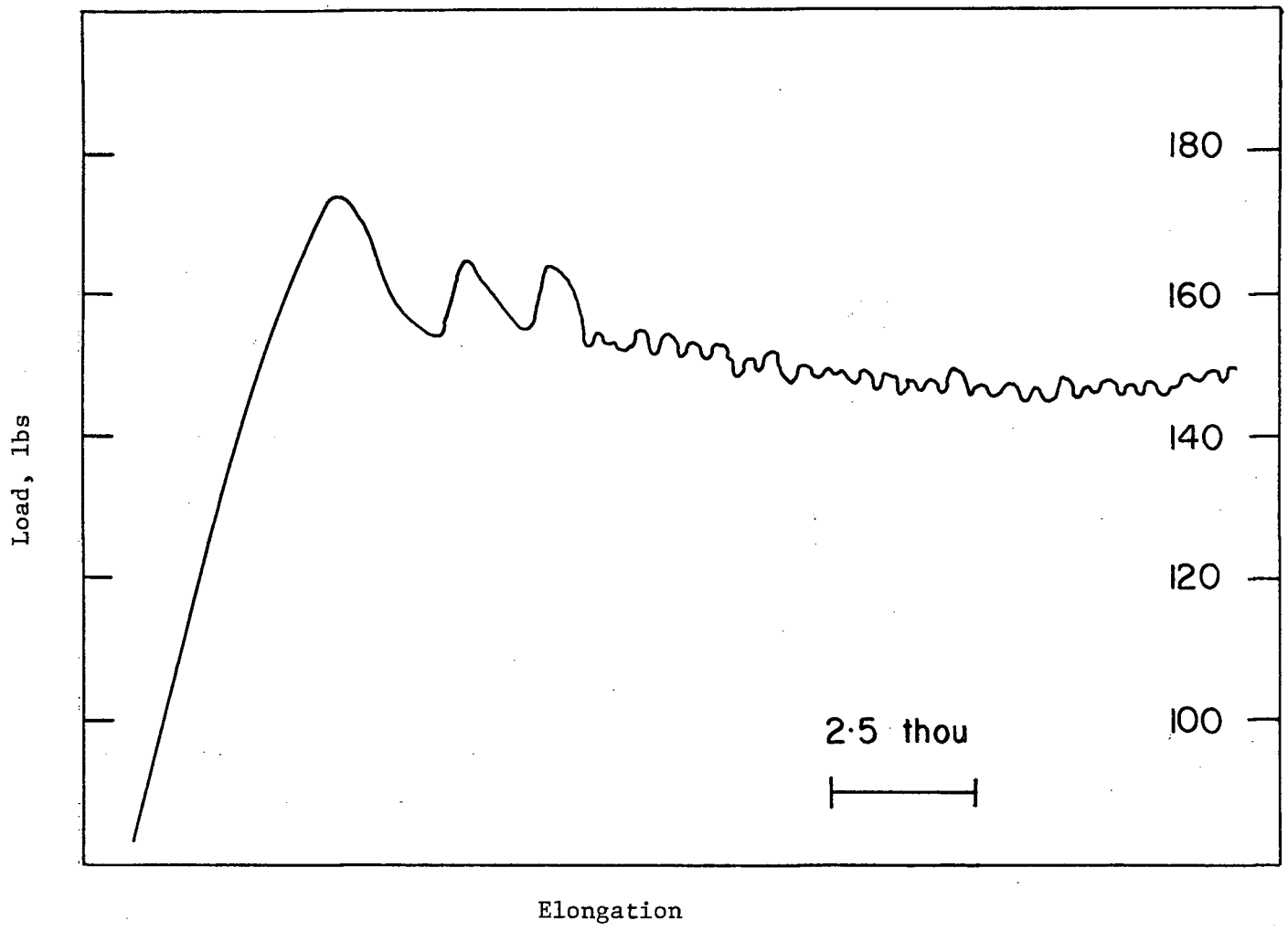

Fig 18. Initial part of load-elongation plot obtained during deformation of Nb 0.5 Ta at 77 °K.

(Load subsequently increased to 171 lbs.)

alloying (stability theory) can also predict the increase in yield drop at low temperatures and its disappearance at high temperatures, if it is assumed that the work hardening rate does not change significantly with temperature.

Since two-stage hardening is observed only at room temperature and above, the hardening rates below room temperature must be compared with stage II hardening rates above 295°K. However, because of the onset of non-uniform deformation, the determination of work hardening rates becomes doubtful at low temperatures. This difficulty is reflected in the results of Mitchell et al (1963), who obtained scattered data consistent with either of the following possibilities:

a) the values of θ_{II} may increase slightly at low temperatures. They rejected this possibility on the grounds that the apparent values of θ_{II} were too high because of the observed occurrence of non-uniform deformation. However it is also possible that non-uniform deformation may lead to apparent values of θ_{II} which are too low.

b) a maximum in the value of θ_{II} may occur at about 250°K. They favoured this possibility; similar behaviour has been reported by Mordike (1962) and by Keh and Weissman (1963). However the maximum always appears to coincide with the point of rapid increase in yield stress (and onset of restricted ductility), with the accompanying possibility of non-uniform deformation. In compression testing, deformation may initially be stable even at low temperatures, and it has then been observed that the work hardening rate (in Mo) does increase with decreasing temperature (Prekel and Conrad (1968)).

In the case of the two NbTa alloys which were ductile at 77°K, the work hardening rate must have been sufficiently high to stabilize a neck once it had formed. It is suggested that the three large yield drops observed in Fig 18 correspond to the onset of localized deformation in the three regions observed on the specimen after failure. At 77°K, both interstitial and substitutional atoms are essentially immobile (Thomas and Leak (1954)); it therefore appears that no mechanism such as dynamic strain aging could account for the wavy flow. The effect could be a result of successive localized slip and hardening, suggesting that deformation occurred very close to the stability condition. Since the yield stress was high, stability would require an increase in work hardening rate above the room temperature value.

4.2.1.2.2 Solute hardening and softening

The onset of solution softening at low temperatures and at small solute concentrations has been frequently observed in single crystal bcc alloy systems (eg Mitchell and Raffo (1967)). The reduced temperature sensitivity of the dilute alloy produces a minimum in the yield stress versus composition curve. The effect has been observed up to 175°K in the case of TaRe alloys (Raffo and Mitchell (1968)), and up to 220°K in WRe alloys (Raffo (1969)). This latter observation was unusual in that at 77°K, continuous softening occurred up to a composition of 25 at% Re; the minimum yield stress in other systems is usually at 1 - 4 at% solute.

Solution softening has also been reported in bcc interstitial solutions at low temperatures (Christ et al (1969)). The effect has been studied recently in Nb single crystals by Ravi and Gibala (1969), who added controlled amounts of oxygen.

As Fig 17 shows, the effect was observed in the NbTa alloys, in which slight continuous softening occurred up to 4.8 at% Ta at 77°K; there must be a minimum at some higher Ta concentration because pure Ta is stronger than pure Nb. Unfortunately, because of the onset of brittle fracture at low temperatures, it was not possible to investigate a solution softening effect in the NbMo alloys. However Statham (1968) has observed softening of Nb crystals by addition of 2 at% Mo when tested in compression at 77°K. It is therefore probable that a softening would have been observed in NbMo at 77°K if plastic flow had occurred; a reduction in twinning stress was in fact observed (see Fig 20).

Various arguments have been presented to explain the solution softening effect. One group of authors (Raffo and Mitchell (1968), Arsenault (1969)) considers that solute atoms produce a localized reduction in the Peierls stress. The minimum in the stress versus composition curve $\tau_o(c)$, is then a consequence of a continuously decreasing thermal component $\tau^*(c)$, and a continuously increasing athermal component $\tau_\mu(c)$. At low temperatures, $\tau^*(c)$ initially predominates; at high temperatures it is negligible and solution hardening occurs.

However the published data is not completely consistent with this interpretation. Fig 19 shows the composition dependence of yield stress for TaRe alloys observed by Mitchell and Raffo (1967) at 77°K and 623°K. According to the above interpretation, the two curves are represented by the equations:

$$\tau(c)_{77} = \tau^*(c)_{77} + \tau_\mu(c)_{77} \qquad (1)$$

and

$$\tau(c)_{623} = \tau^*(c)_{623} + \tau_\mu(c)_{623} \qquad (2)$$

since $\tau^* = 0$ for $T > T_o$.

Since τ_μ is not very dependent on temperature,

$$\tau_\mu(c)_{77} \simeq \tau_\mu(c)_{623}$$

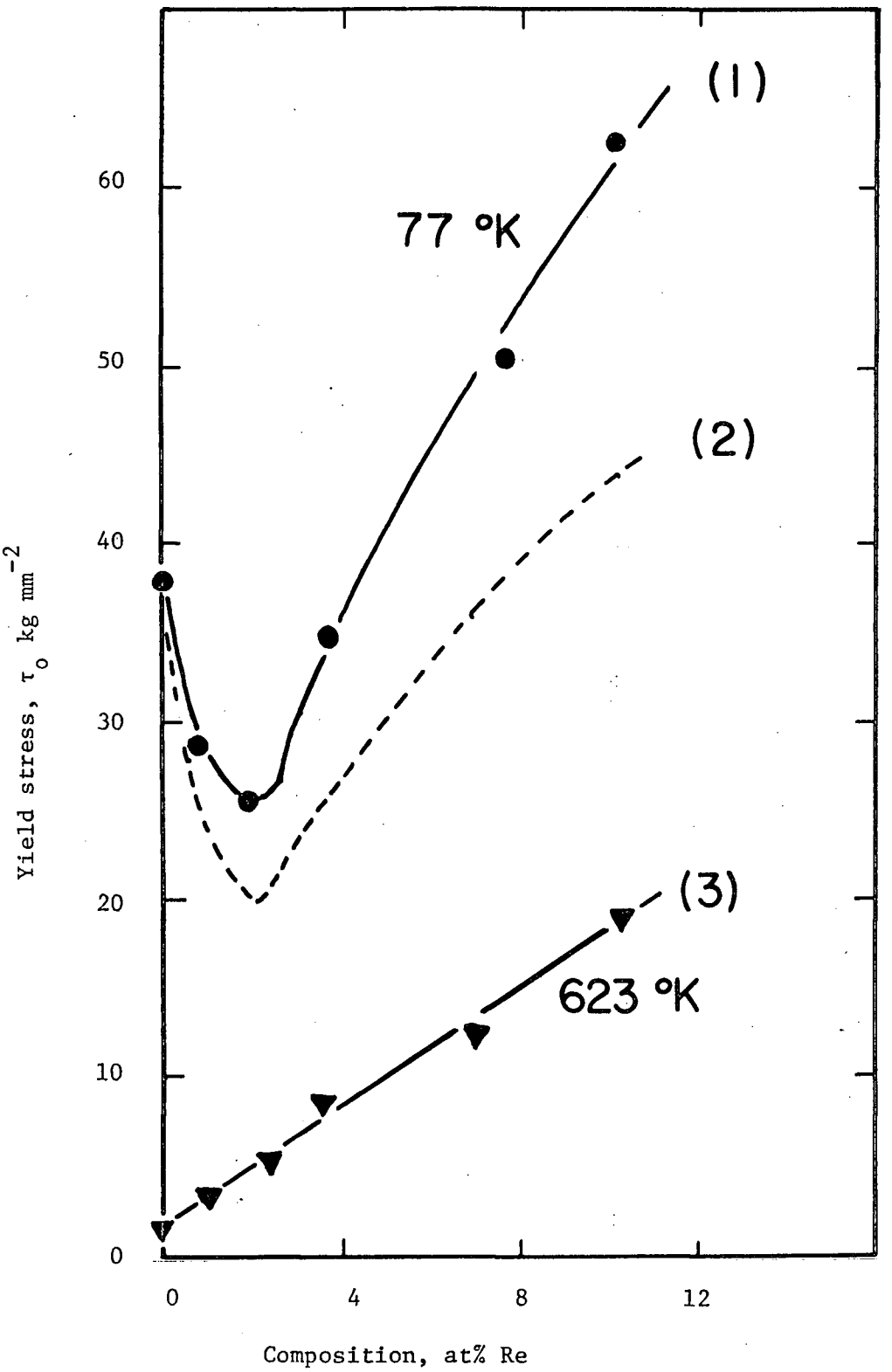

Fig 19. Composition dependence of yield stress for TaRe alloys.

(after Mitchell and Raffo (1967))

therefore from equations (1) and (2)

$$\tau^*(c)_{77} \simeq \tau(c)_{77} - \tau(c)_{623} \qquad (3)$$

This equation (3) is represented by the dotted curve in Fig 19. It can be seen that there is no possible way in which τ^* can continuously decrease with additional solute, as the theory assumes.

The microstrain technique can usefully be applied to this problem and further discussion will be delayed until the microstrain results have been presented.

4.2.2 Twinning

At 77°K, sporadic twinning was observed in pure Nb and in the NbTa alloys. The accompanying load drop and audible click were correlated with the formation of a visible twin right across the specimen. Frequently the operation of one twin system was followed by a second. Fig 21 is a micrograph showing two intersecting sets of twins. The twin systems were identified using the technique outlined in A.3.3 and were found to be $(\bar{1}12)$ $[1\bar{1}1]$ and $(\bar{1}\bar{1}2)$ $[111]$.

For the orientation used, there are six possible twin systems which give an extension on twinning; the observed systems were the two with the largest Schmid factors (0.378 and 0.359 respectively). In the remaining cases, the stress at which twinning started was resolved on the most favourable twin system. Although twinning started at different points on the flow curve, the values of resolved twinning stress were quite consistent; this indicates that a critical stress exists in order for twinning to occur. The results are shown in Fig 20. It can be seen that addition of solute reduces the twinning stress at 77°K, just as it reduces the yield stress at that temperature.

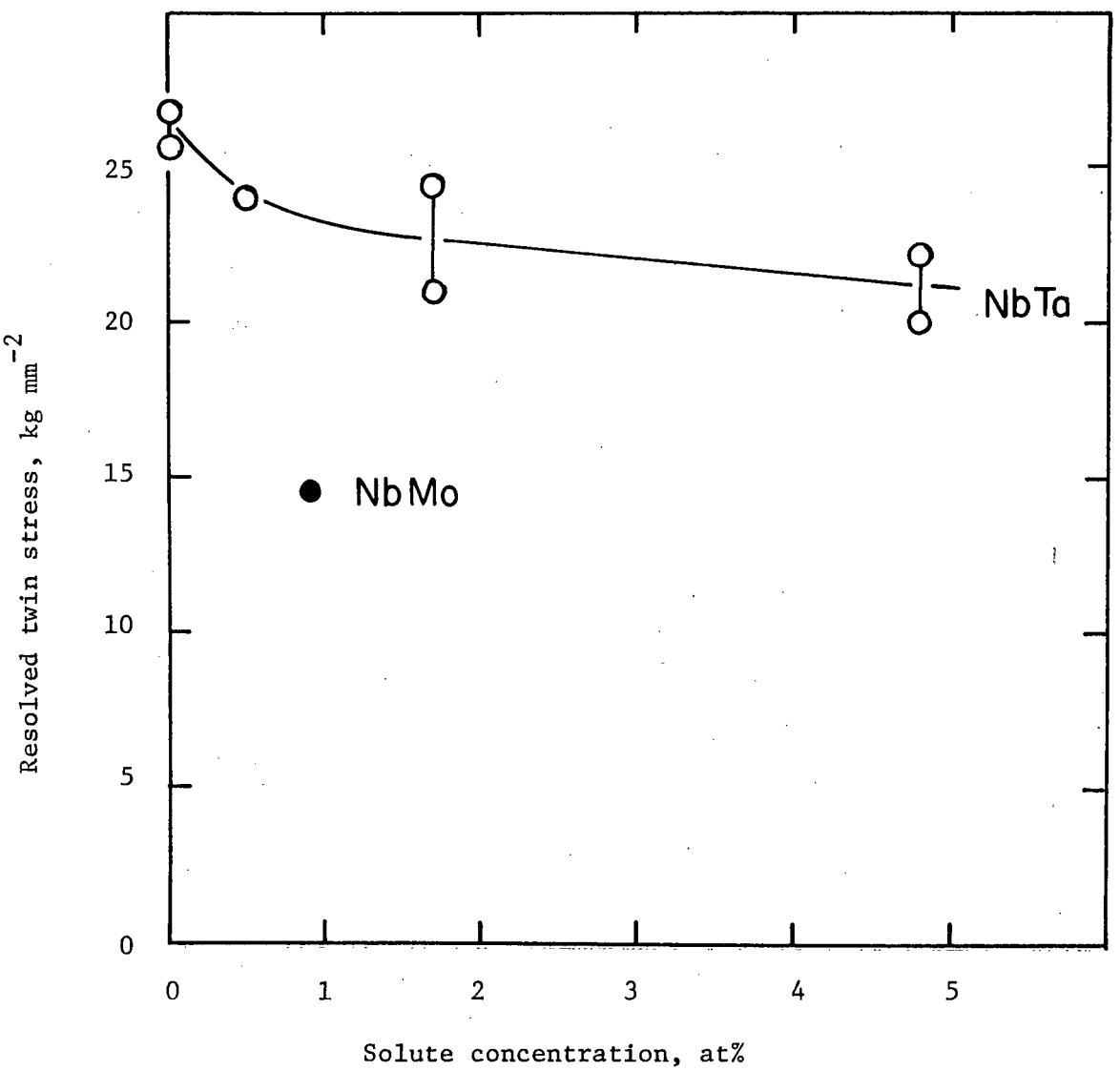

Fig 20. Resolved twin stresses in Nb alloys at 77 °K.

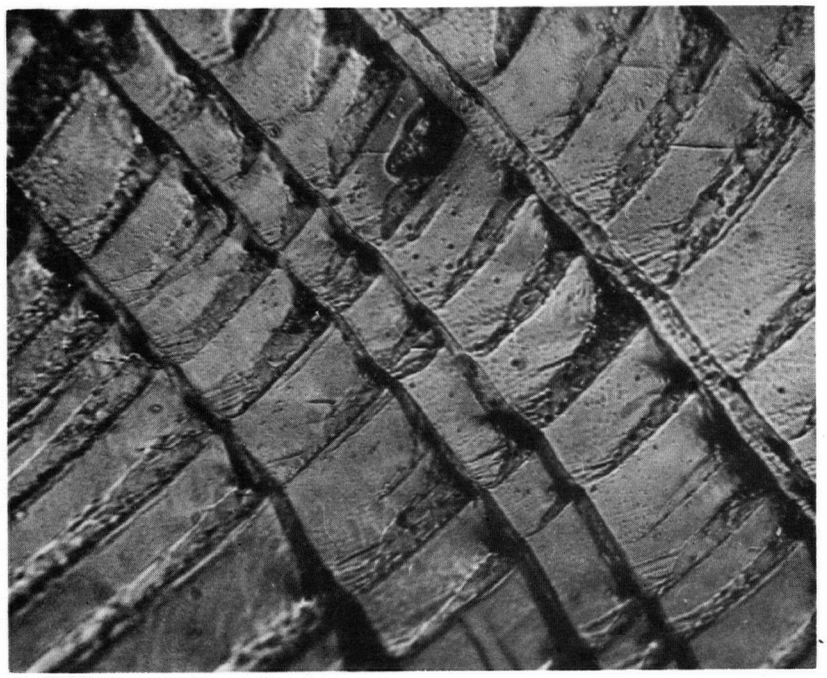

Fig 21. Intersecting twins in Nb 4.8 Ta alloy (x600).

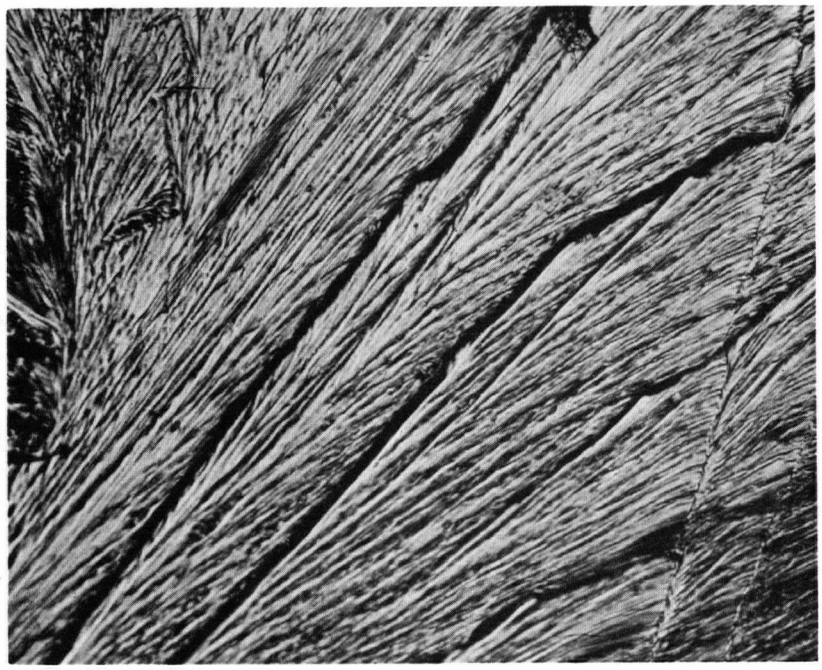

Fig 22. (001) Cleavage plane in Nb 6.6 Mo alloy (x230).

The only Mo alloy tested twinned without yielding, at a much lower stress than did pure Nb.

Twinning has frequently been reported in Nb crystals deformed at 77°K (eg Bowen et al (1967)). The incidence of twinning appears to increase as interstitial impurities are removed. Although twinning was observed in both the NbMo and NbTa alloys, it may be suppressed at higher solute concentrations since Milne and Smallman (1968) did not observe twinning in Nb 50 Mo.

Twinning at 77°K could be prevented by prestraining the crystals at room temperature.

4.2.3 Cleavage

At 190°K, the more concentrated Mo alloys failed by cleavage at the specimen shoulders, without any indication of plastic flow. Even prestraining the crystals at room temperature did not prevent brittle fracture. Since the stress concentration at the grips initiated the failure, cleavage stresses were not determined.

The cleavage plane was found by Laue back-reflection photography to be (001) in all cases. This is the usual cleavage plane in bcc metals. A photomicrograph of the fracture surface is shown in Fig 22. The surface is not smooth but is covered with steps or "river lines" radiating from the fracture initiation site. These observations are identical to those reported by Raffo and Mitchell (1968) on cleavage in TaRe single crystals.

4.3 Slip line observations at 295°K

4.3.1 Results

Slip line observations were made on the cylindrical tensile specimens, and the operative slip systems were determined by measuring the traces (see A.3.3). Even though the specimens were oriented for single slip, slight activity was often observed on a second system immediately after yield. However the amount of this slip did not appear to increase, and in stage I there was always one principal system, $[1\bar{1}1]\psi$. The value of ψ was determined for all the alloys.

The slip traces were observed to be wavy on one face and straight on a face at 90° to the first. The wavy lines appear on the face from which edge dislocations emerge, and trace the motion of screw dislocations. Similarly the straight lines depict the motion of edge dislocations, and these lines disappear at a position exactly perpendicular to the Burgers vector. Fig 23 shows typical micrographs, taken from the positions shown, approximately 90° apart.

There were no significant differences in the form of slip traces observed in pure Nb and in the alloys.

With pure Nb and the NbTa alloys, the onset of stage II agreed theoretically with that expected from the movement of the tensile axis during deformation. However the position of the tensile axis subsequently overshot the [001] - [101] symmetry boundary by 7 - 10°. Slip on the conjugate system was observed in stage II.

The results of the slip determinations in the alloys are shown in Table II. The original orientation is indicated by the angle χ, which is the angle between the maximum resolved shear stress plane and the (011) reference plane. Since slip was observed to be always in the $[1\bar{1}1]$ direction,

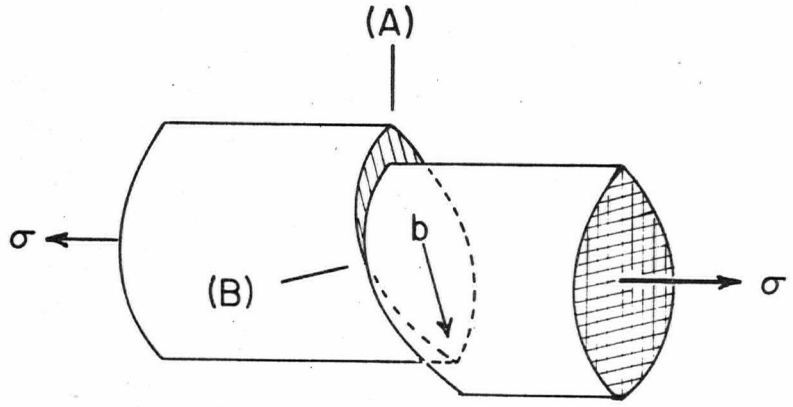

(A)

Nb 4.8 Ta alloy
(x600)

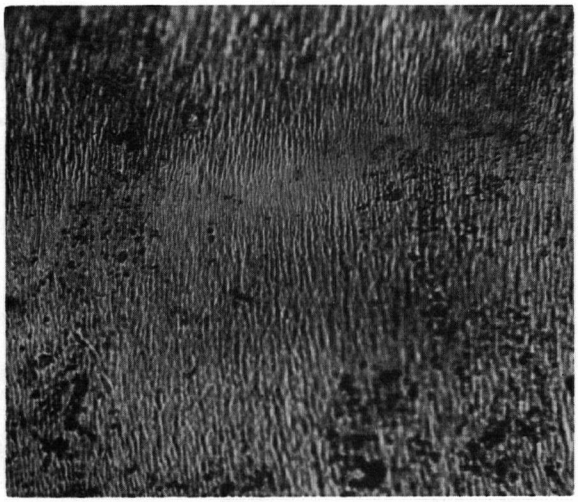

(B)

Nb 4.9 Mo alloy
(x600)

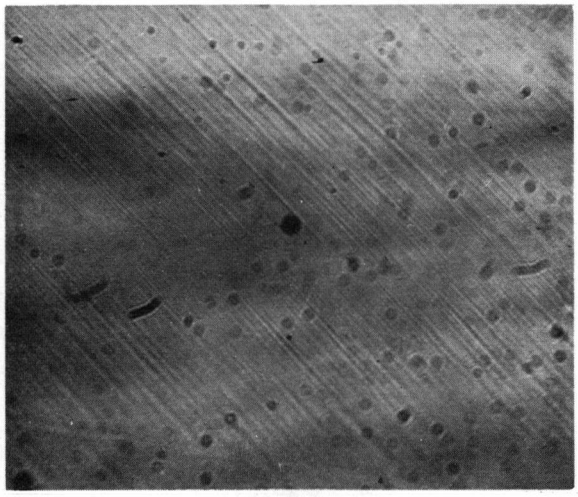

Fig 23. Slip line observations in Nb alloys deformed into stage I, from (A) and (B).

Table II. Crystallography of slip in Nb alloys at 295°K.

Specimen	Orientation χ°	Slip parameter ψ°	Stage II overshoot (°)
A33	6	6	9
A34	6	4	7
B42	10	14	7
B43	10	20	9
C41	3	0	10
C44	3	13	9
D42	10	14	8
J22	-4	3	-
J24	-4	-4	-
K22	8	14	-
K23	8	6	-
L31	7	7	-
L33	7	2	-

the tensile axis moves during deformation along a great circle towards $[1\bar{1}1]$ and χ is therefore independent of strain.

Fig 24 includes the observed slip parameter ψ compared with the values expected if slip were crystallographic. It can be seen that slip did not usually occur on (011). In addition, there could be some clustering about (143) and (132). However, if an error of $\pm 2°$ is admitted in ψ, then only 54% of the cases can be described as crystallographic compared with 48% if ψ was randomly distributed between $-5°$ and $+20°$. Therefore slip cannot be described as being crystallographic.

There is no evidence for any dependence of ψ on alloy content.

4.3.2 Discussion

There appear to be no reports of slip line studies on NbTa or NbMo alloys. This is because most workers have been concerned with measurements of τ_o. It is usual to resolve the yield stress onto the (011) plane, which is a reasonable approximation for crystals oriented in the middle of the stereographic triangle.

Milne and Smallman (1968) found slip line analysis on NbMo alloys to be impossible because of the confusion of surface markings on their samples. They determined slip systems by asterism analysis. In no cases did they observe slip on (011); the usual slip plane was reported to be (132) or (143). This is in agreement with the present results although the possibility of crystallographic slip on these planes is discounted.

Slip on any plane could be produced by composite slip on different {011} planes (Maddin and Chen (1953)), but there is some evidence that {112} could also be a discrete slip plane (see A.3.2). It is evident from the slip line results and from Fig 23(A) that cross-slip was prevalent in the deformation of the Nb alloys. This differs from the observations of Mitchell

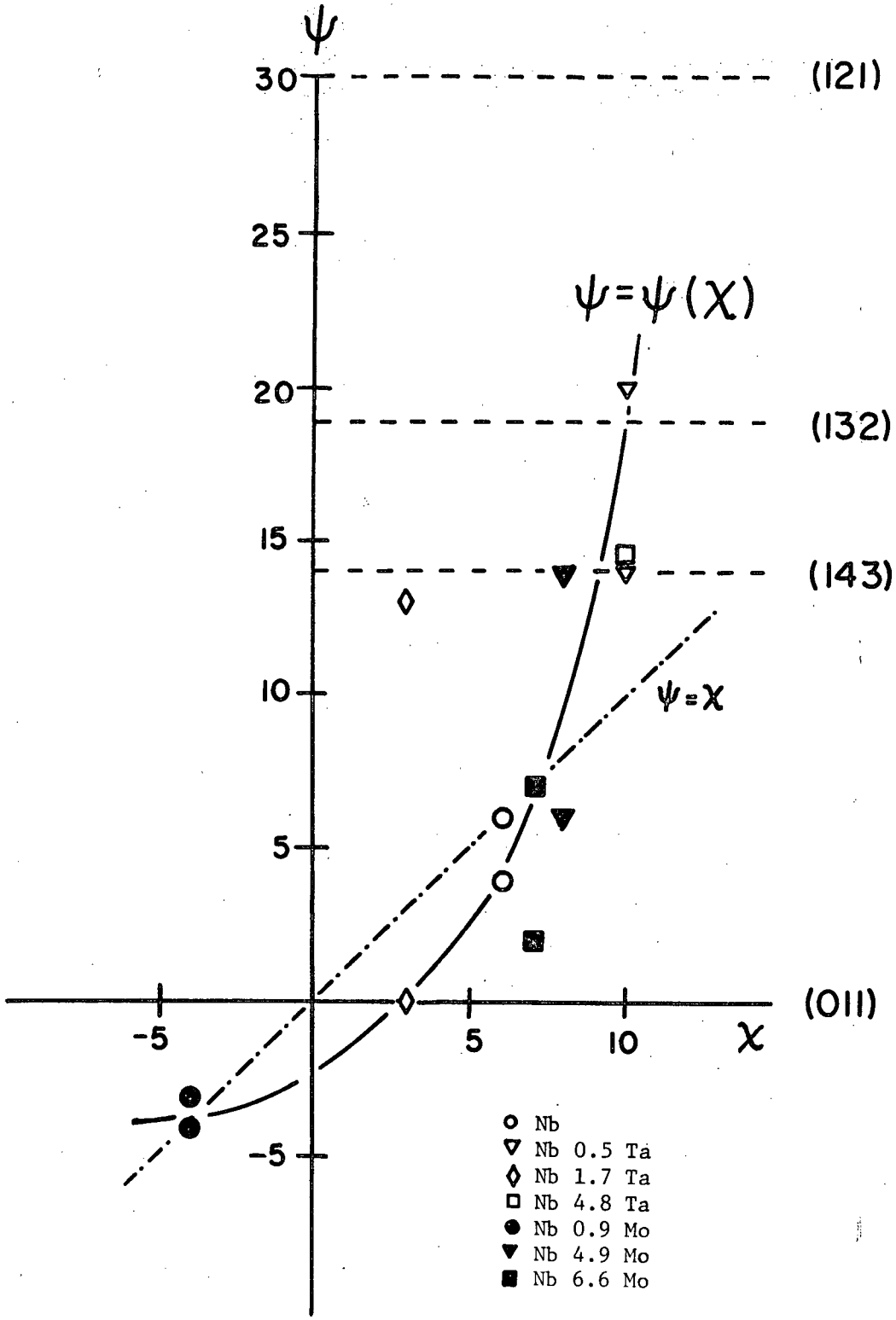

Fig 24. Results of slip line analyses on Nb alloys expressed as $\psi(\chi)$.

and Raffo (1967) on TaRe alloys. They reported slip on (011) in all the alloys, whereas pure Ta slipped on the maximum resolved shear stress plane.

It is usual to express an observed orientation dependence of slip in terms of $\psi(\chi)$ curves. Although the crystals tested here had similar orientations, there was a spread of 14° in the measured χ values. The positions of $\psi(\chi)$ are shown in Fig 24 and there is seen to be a definite orientation dependence, although it does not take a simple form. For intermediate orientations ($5° < \chi < 10°$) the slip plane is close to the maximum resolved shear stress plane ($\psi = \chi$). At low χ there are deviations towards (011) and at high χ, deviations away from (011).

5. MICRODEFORMATION OF PURE NIOBIUM CRYSTALS

5.1 Introduction

5.1.1 Microstrain observations

By load cycling specimens to successively higher stresses, different points in the yielding process can be identified: the elastic limit, τ_e, is the stress at which reversible dislocation motion first occurs; the anelastic limit, τ_a, is the stress at which irreversible dislocation motion first occurs; the macroscopic flow stress, τ_f^o, is the relatively constant stress at which gross plastic flow occurs. The elastic and anelastic limits depend on the sensitivity of the strain measurement; a strain sensitivity of 10^{-6} has usually been taken as standard.

In order to establish a hysteresis loop and obtain reversible dislocation motion it is necessary to create a "directional" internal stress field (with stress component τ_i^d) which will allow dislocations to return to their original positions when the applied stress is removed. This may be accomplished by prestraining the annealed material; further, a supply of mobile dislocations is thereby obtained in crystals where the dislocations may have been locked.

Before prestraining, an internal stress field exists in an annealed crystal. This will be termed an "adirectional" stress field (with stress component τ_i^o) in that it opposes the motion of dislocations irrespective of their direction of motion (cf a "drag stress"). The relative magnitudes of τ_i^d and τ_i^o are not specified.

The following idealized model illustrates the manner in which a stable hysteresis loop is established in an annealed crystal where τ_i^d is

initially zero. Suppose dislocations move when the effective stress on them (τ_x) reaches a critical value τ_s ($\geq \tau_i^o$). At any applied stress τ, the effective stress is given by

$$\tau_x = \tau - \tau_i^d$$

Consider load cycling to successively higher stresses as shown in the diagrams of Fig 25.

In A, at a stress $\tau = \Delta\tau$, $\tau_i^d = 0$. Therefore $\tau_x = \Delta\tau$, which is less than τ_s and so no dislocation motion occurs.

In B, dislocations first move when $\tau = \tau_x = \tau_s$ and they continue to do so as long as the load increases. When straining is stopped at $\tau = \tau_s + \Delta\tau$, $\tau_i^d = \Delta\tau$. If there is no relaxation on unloading then $\tau_i^d = \Delta\tau$ at $\tau = 0$ and therefore

$$\tau_x = -\Delta\tau$$

This stress is still less than τ_s and the dislocations do not move. No reversible dislocation motion has yet occurred.

In C, at $\tau = \tau_s + \Delta\tau$, $\tau_i^d = \Delta\tau$. Therefore $\tau = \tau_s$ and dislocations move again. When straining is stopped at $\tau = 2\tau_s + \Delta\tau$, $\tau_i^d = \tau_s + \Delta\tau$. On unloading to $\tau = \Delta\tau$, $\tau_x = \Delta\tau - (\tau_s + \Delta\tau) = -\tau_s$.

Therefore dislocations now move backwards until at $\tau = 0$ $\tau_x = -\tau_s$ and $\tau_i^d = \tau_s$.

A stable hysteresis loop, as in D, has now been formed and reversible dislocation motion will always occur when

$$\tau_x = \tau_s = \tau - (-\tau_s)$$

By definition this applied stress is τ_e and

$$\tau_e = 2\tau_s \geq 2\tau_i^o$$

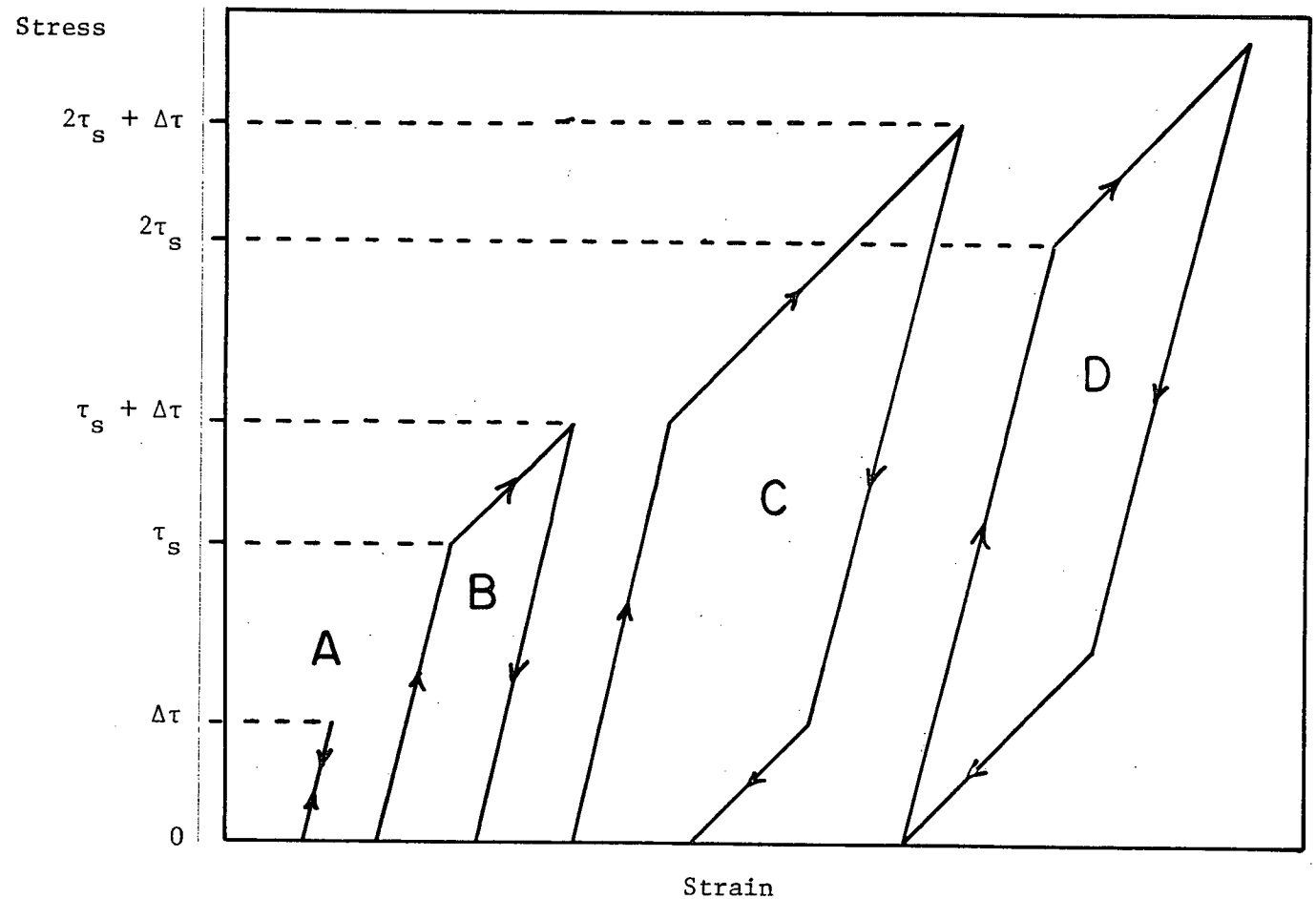

Fig 25. Model for formation of a stable hysteresis loop.

The hysteresis loop will remain stable until irreversible dislocation motion occurs at a stress τ_a, at which the loop does not close.

5.1.2 Previous work

The microstrain technique was first applied to the study of yielding and flow in bcc metals by Brown and his co-workers (Brown and Ekvall (1962)). The procedure they adopted is indicated schematically in Fig 26a. The elastic limit, τ_e, is the stress at which a loop was first formed and the anelastic limit, τ_a, is the stress at which permanent set first occurred. Brown and Ekvall and later, Kossowsky and Brown (1966), investigated the dependence of τ_e and τ_a on purity, temperature, and prestrain. They identified τ_e with the stress to move existing kinks on dislocations; τ_a was identified with a Peierls stress to move screw dislocations.

The uniqueness of τ_e depends very much on the form of the hysteresis loops; in tension, specimen alignment is critical and it is unlikely that anelastic deformation is completely uniform. In compression, Meakin (1967) observed hysteresis loops that were parallelipipeds rather than being of lenticular shape (see Fig 26b); the values of τ_e were typically less than one-tenth of the values reported for tension.

Meakin suggested that the τ_e observed in compression represents the true elastic limit. In fact, up to this stress the modulus agreed with the "dynamic modulus" calculated from the dynamically determined elastic constants (see A.5.1). Above τ_e the extensive linear anelastic strain contribution gave a smaller "relaxed modulus" which was typically 30% - 50% of the dynamic value. Meakin further suggested that in the case of tensile deformation the true elastic limit was not observed and that the apparent value reported by Brown and Ekvall coincided with a deviation from the

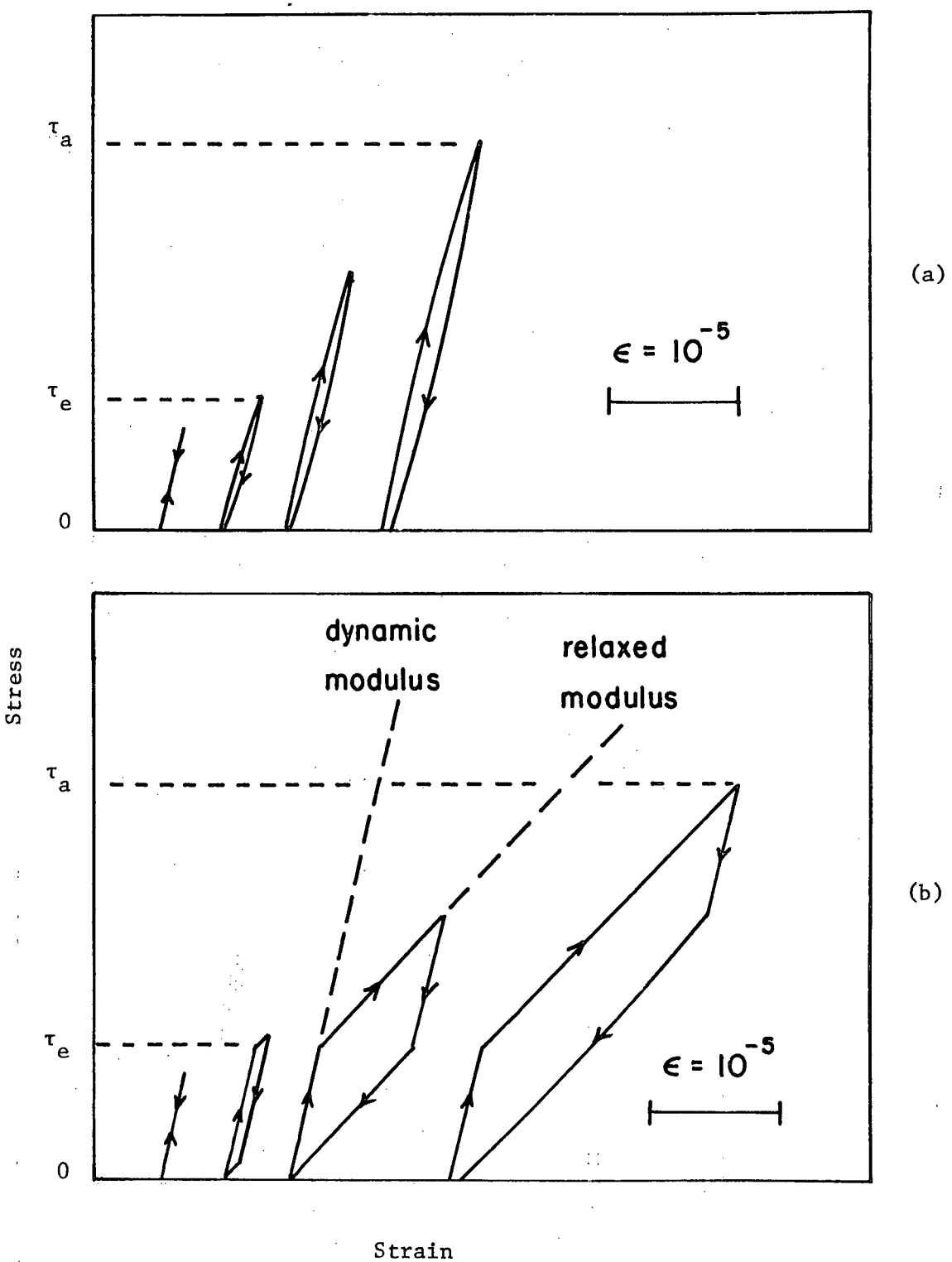

Fig 26. Types of hysteresis loops observed in:
a) tension b) compression (Meakin (1967))

relaxed modulus rather than from the dynamic modulus.

It is quite possible that in tension the true elastic limit is not observed, but nevertheless the observed modulus cannot be identified with the relaxed modulus observed in compression. In all the cases examined in this work, the observed modulus in tension agreed with the calculated dynamic modulus to within 10%.

In this study no attempt was made to identify an elastic limit. The nature of plastic flow from the anelastic limit, which can be identified unequivocally, up to macroflow was considered to be of greater interest. Previous methods for determining such a microflow curve have had disadvantages. For example, Stoloff et al(1965) and Davies and Ku (1966) constructed curves by load cycling right up to macroflow, but this method records some strain which occurs at stresses below the maximum reached in any cycle. On the other hand, Carnahan et al (1967) used continuous straining but, in the determination of plastic shear strain, could not allow for non-linear anelastic deformation occurring before microyield. Such strains are of the same order as the plastic strains in the region of microyield. The technique adopted in this work overcomes both of these difficulties.

5.1.3 Experimental procedure

The transition from micro to macroyielding was observed during tensile deformation of crystals which had a capacitance extensometer attached directly to the specimen gauge length (see A.4 for experimental details). The onset of yielding was determined by load cycling up to the stress at which permanent set first occurred (anelastic limit or microyield stress, τ_a). This point also defined the elastic slope (or more correctly, the "anelastic slope") of the microflow curve which was subsequently obtained by continuous straining up to the macroflow stress, τ_f^o. This is defined as

the applied stress when gross plastic deformation occurs at a rate determined by the crosshead speed. Thus τ_f^o is asymptotically approached after yielding, but the strain to reach τ_f^o is not specified. At room temperature τ_f^o is the same as the prestrain stress, τ_f, as obtained from the macroscopic flow curve.

The method used to determine the microflow curve $\tau(\gamma)$ is indicated schematically in Fig 27. A small positive load was taken as the base stress level to maintain alignment. A resulting microflow curve, plotted as $\tau(\log \gamma)$, is shown in Fig 28. For any test, the vertical line forming part of the "L" motif represents the strain sensitivity limit for the test; the horizontal line represents the highest stress reached before a permanent set was observed. The circled point represents the value obtained by load cycling, and the remaining points have been calculated from the continuous loading curve. This method of expressing microflow curves avoids the tendency to extrapolate the microyield stress to zero strain, which is tempting when curves are plotted on a linear strain scale (see 6.2.1).

5.1.4 Reproducibility of microflow

Although some microflow experiments were performed directly on as-grown crystals, it was usual to prestrain the crystals into stage I before testing. The microflow curve was found to be reproducible in this region provided the crystal was prestrained at the flow stress τ_f before each determination. If the specimen was given a small prestrain to a stress τ_b below the flow stress, then the subsequent apparent microyield stres τ_a' was increased. The behaviour is indicated schematically in Fig 29. This means that, in any microyield determination, the apparent microyield stress passes through a maximum as the prestrain stress increases from τ_a to τ_f. Such behaviour, though not investigated quantitatively, is important as a

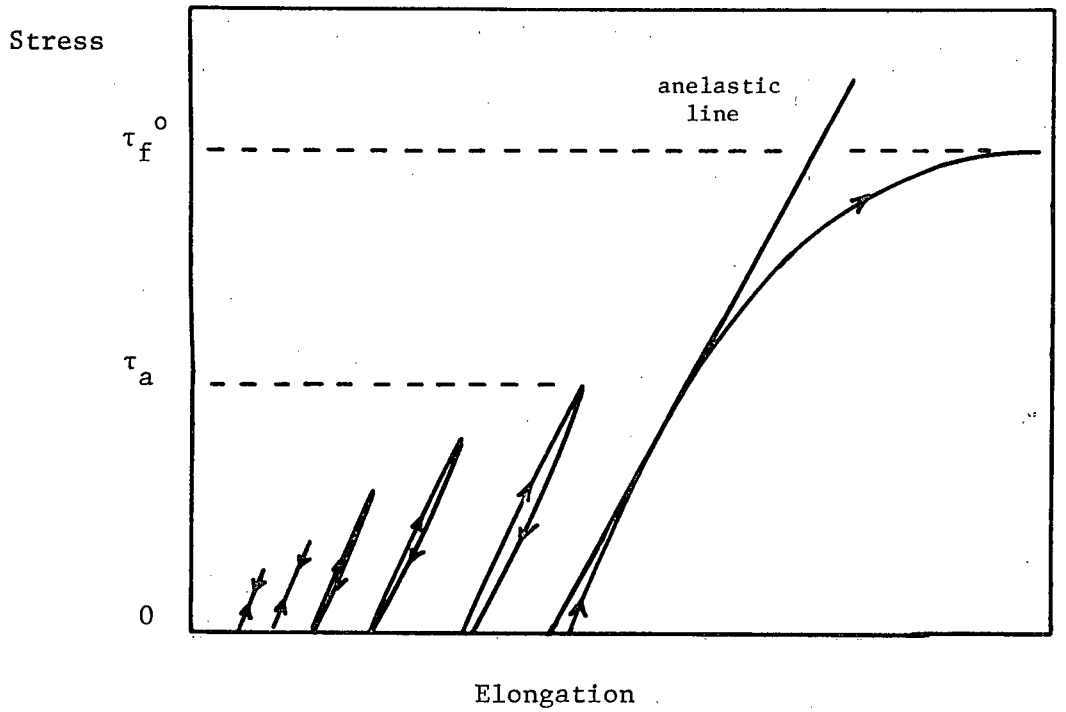

Fig 27. Technique for obtaining microflow curves.

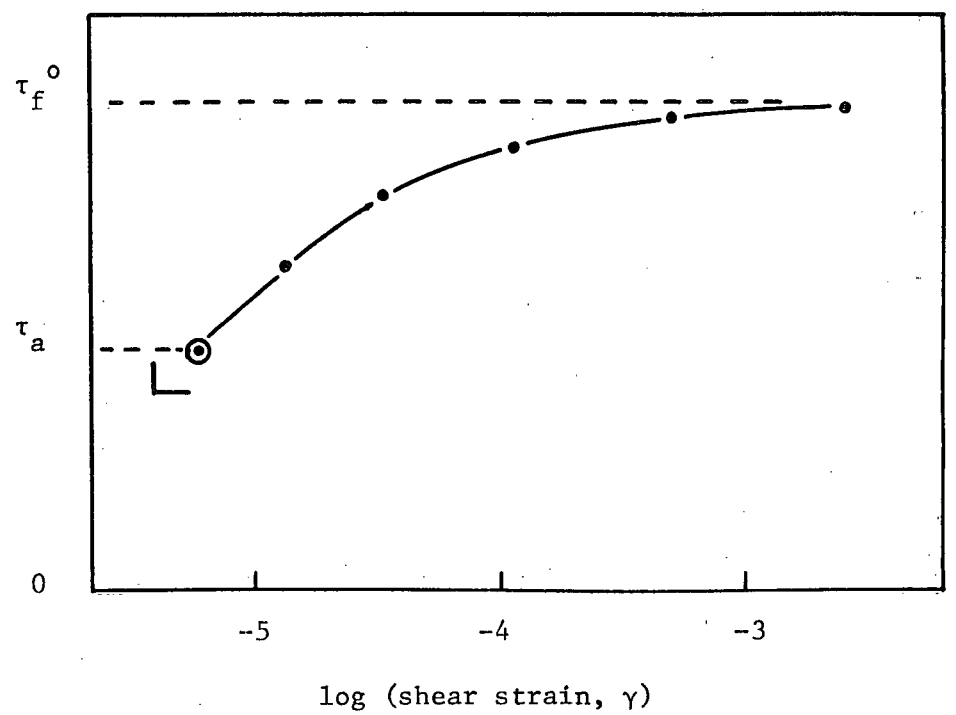

Fig 28. Representation of microflow data.

manifestation of a hardening process in the microstrain region which ceases at the flow stress. It is also suggested that the maximum value of τ_a' would represent a stress at which dislocation multiplication becomes significant.

5.1.5 Discussion of microflow

It has been seen that τ_a' is very sensitive to the prestrain stress τ_b, although the strain involved in prestraining to τ_b is very small ($\gamma \simeq 10^{-4}$). The dislocation motion involved is so small relative to that required to produce a similar hardening in the macroflow region, that the effect cannot be due to any gross change in dislocation density. Furthermore, even when the microyield stress is raised, the subsequent asymptotic flow stress is unaffected, which again suggests that the effect is due to a significant change in a small fraction of the dislocations rather than to a change in the overall dislocation structure.

One of the difficulties associated with the interpretation of microyield values is that it is not known how many dislocations are involved in microyielding. Thus the particular strain at which τ_a is measured could be produced by a small number of dislocations moving a large distance, or by a large number of dislocations moving a small distance. Since only a small fraction of the total dislocations move, a change in this proportion could account for the observed change in microyield stress between τ_a and τ_a'.

One possibility is that prestraining to τ_b after unloading from τ_f increases the number of dislocations which can move at a given stress, but it is not physically acceptable to suppose that they then require a higher stress to produce the same strain. On the other hand prestraining could decrease the number of dislocations which can move at the particular stress. It would then be required that the stress to move them increase

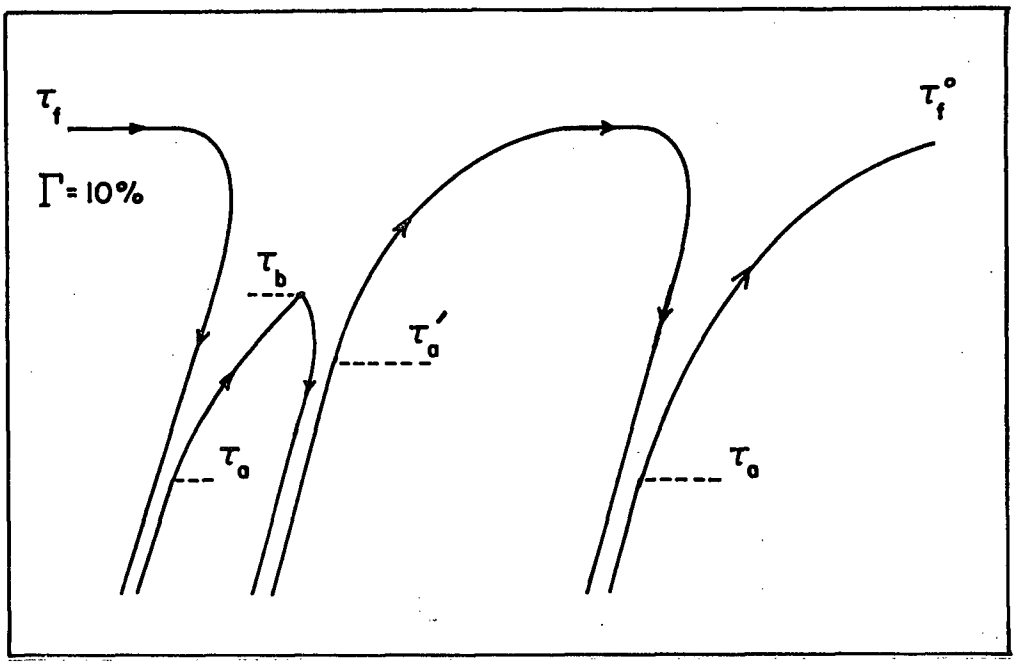

Fig 29. Schematic description of microflow behaviour observed during stage I deformation at 295 °K.

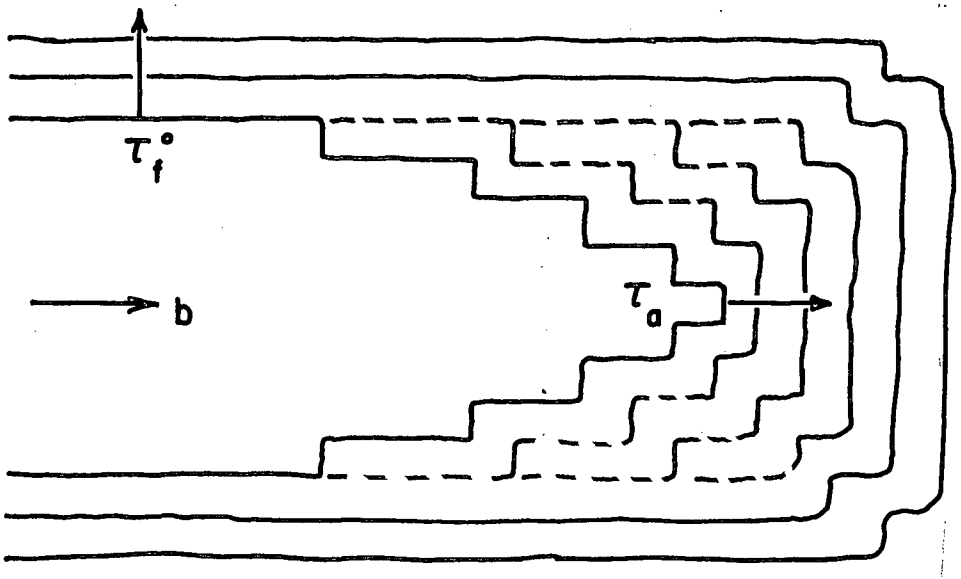

Fig 30. Model for movement of a dislocation half-loop in the microflow region.

quite rapidly with the distance moved. There appear to be two possible explanations for this stress increase:

a) The mean value of the fluctuating internal stress field could increase as dislocations move from their equilibrium positions. On straining above τ_a some dislocations would be stopped or pass out of the crystal, thereby reducing the mobile dislocation density. On unloading and reloading, the remaining dislocations would have to move further through the internal stress field, producing a larger microyield stress τ_a'. On restraining at the flow stress, dislocation multiplication would again produce a distribution of moveable dislocations in equilibrium with the internal stress field.

b) If it is realized that a dislocation line cannot end inside a crystal, and that consequently most dislocations must be in the form of loops or networks, then the possibility exists that a loop may not expand uniformly at a given stress. Thus if only a particular part of a dislocation loop can move at τ_a, the proportion of this part will decrease as the loop expands. Therefore after unloading and reloading it will be necessary to apply a higher stres τ_a' to move a different portion of the dislocation loop. Further straining at the flow stress will move the whole loop, which will subsequently take up an "equilibrium" configuration again.

The second suggestion has fewer independent requirements and can be supported indirectly by evidence obtained from transmission electron microscopy. Solomon and McMahon (1968) have examined dislocation rearrangements at 77°K in the microstrain region of Fe polycrystals prestrained

at room temperature. They observed that there is a tendency for the dislocations to align in the screw orientation. Thus at 77°K the edge components of the dislocation tangles move preferentially and consequently become exhausted. On continued straining at higher stresses, the screw dislocations move. These observations have also been reported in Mo single crystals by Lawley and Gaigher (1964) and in Fe single crystals by Keh (1968). On the basis of these experiments, Solomon and McMahon accounted for the observed decrease in microplastic response on successive loading cycles at 77°K; it is therefore proposed that a similar exhaustion hardening of edge dislocations accounts for the preliminary microflow observations reported here at 295°K. The suggested model is shown in Fig 30 which illustrates the relative motion of edge and screw components in a dislocation loop during straining in the microflow region.

5.2 Results

5.2.1 Deformation at 295°K

Fig 31 includes microflow curves for a Nb crystal (A62) in two different conditions: as-grown and prestrained 10% to the beginning of stage I. It can be seen that although straining has increased the macroflow stress as expected, it has decreased the microyield value. Fig 32 shows microflow curves for the same crystal at strains corresponding roughly to the beginning and end of uniform stage I deformation. Further straining has increased both the microyield and macroflow values.

Fig 31 also shows microflow data for two as-grown crystals to illustrate the effect of purity. The lowest curve has been plotted from the data of Bowen et al (1967) who used ultra-high vacuum purified material (specimen 55/6, tested in compression). For the less pure as-grown crystal, A62,

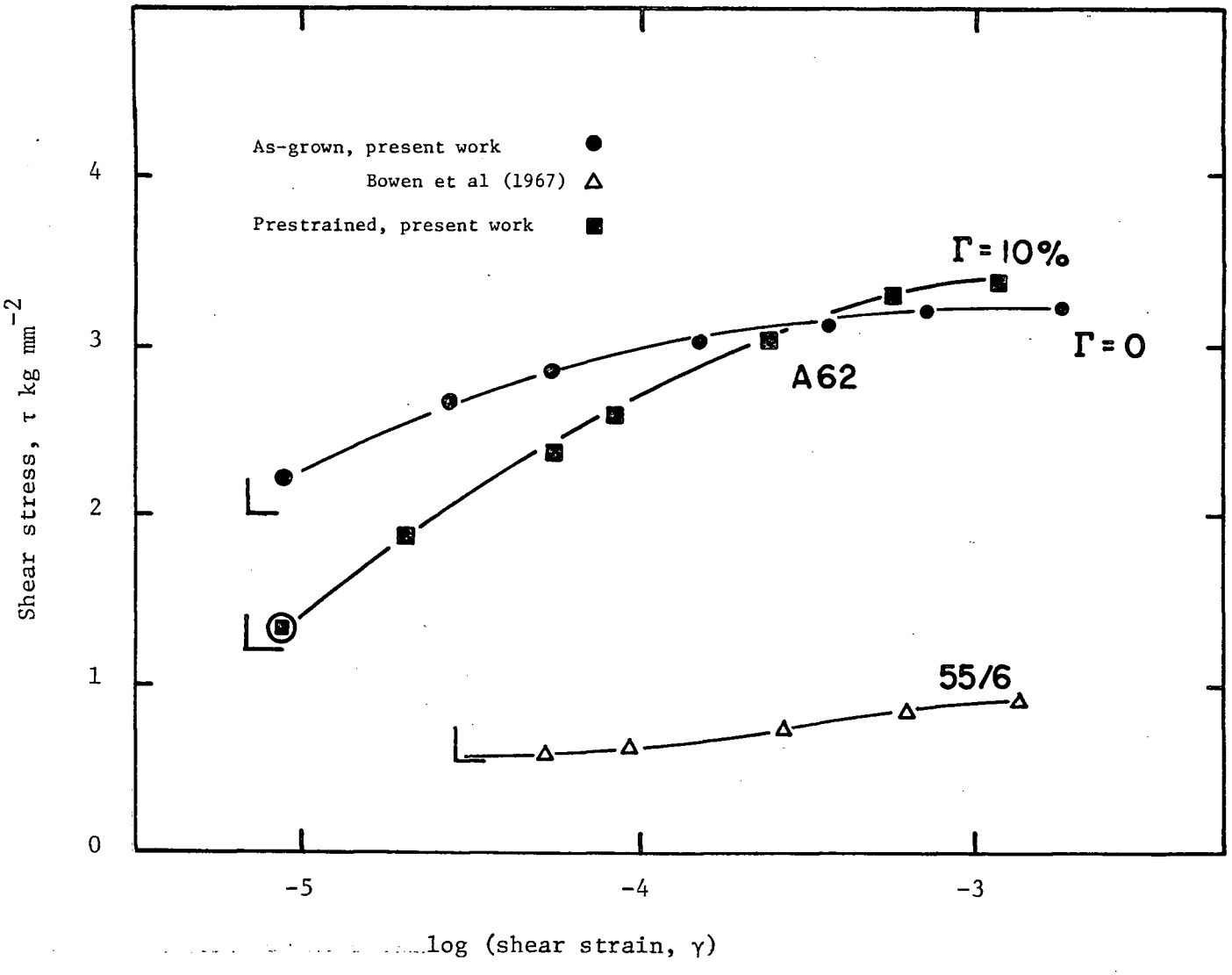

Fig 31. Microflow curves at 295 °K for Nb crystals in different conditions.

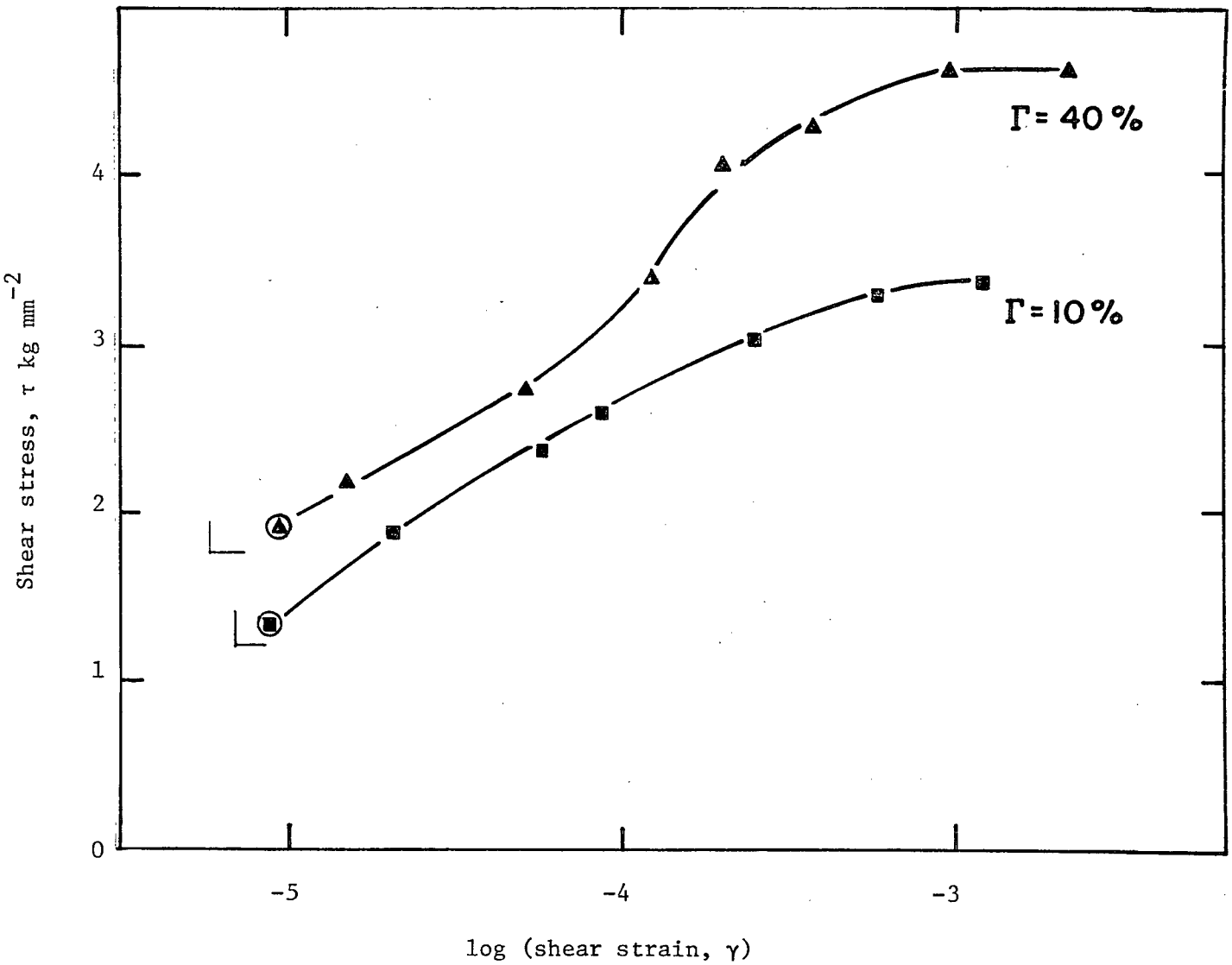

Fig 32. Microflow curves at 295 ° K for a Nb crystal with different prestrains.

both the micro and macroflow values are at least three times greater than for specimen 55/6. Specimen A62 subsequently showed a yield drop; specimen 55/6 did not.

5.2.2 Deformation at 160°K

Fig 33 shows microflow curves for crystals in different conditions tested at 160°K: as-grown (A63), prestrained at 295°K (A64), and high purity as-grown (55/4) which has again been plotted from the data of Bowen et al. It can be seen that at 160°K the effect of purity is far less pronounced than at 295°K (Fig 31) and that the impure prestrained crystal has deformed at a lower stress than the high purity as-grown specimen.

Microyield values at the given strain sensitivities are shown in Fig 34 as a function of temperature. The temperature sensitivity of the microyield stress ($\frac{d\tau_a}{dT}$) in the prestrained crystals is considerably less than it is in the as-grown crystals which in turn is less than the temperature sensitivity of the macroyield stress ($\frac{d\tau_o}{dT}$) (see Fig 35).

Since the stress τ_f^o is, by definition, asymptotically approached after yielding, it can be seen that the plastic strain to reach τ_f^o increases as the temperature decreases. This is a consequence of the greater slope of the microflow curve at low temperatures. For example, at 295°K (Fig 31) the asymptotic flow stress τ_f^o is reached after about $\gamma = 0.1\%$, but at 160°K (Fig 33) the stress does not reach τ_f^o (which is close to the unprestrained flow stress at 160°K) until about $\gamma = 5\%$. These effects are illustrated in Fig 35 which shows the flow stress at various strains as a function of temperature. It can be seen that at very low temperatures the asymptotic flow stress after prestraining will never reach the unprestrained flow stress.

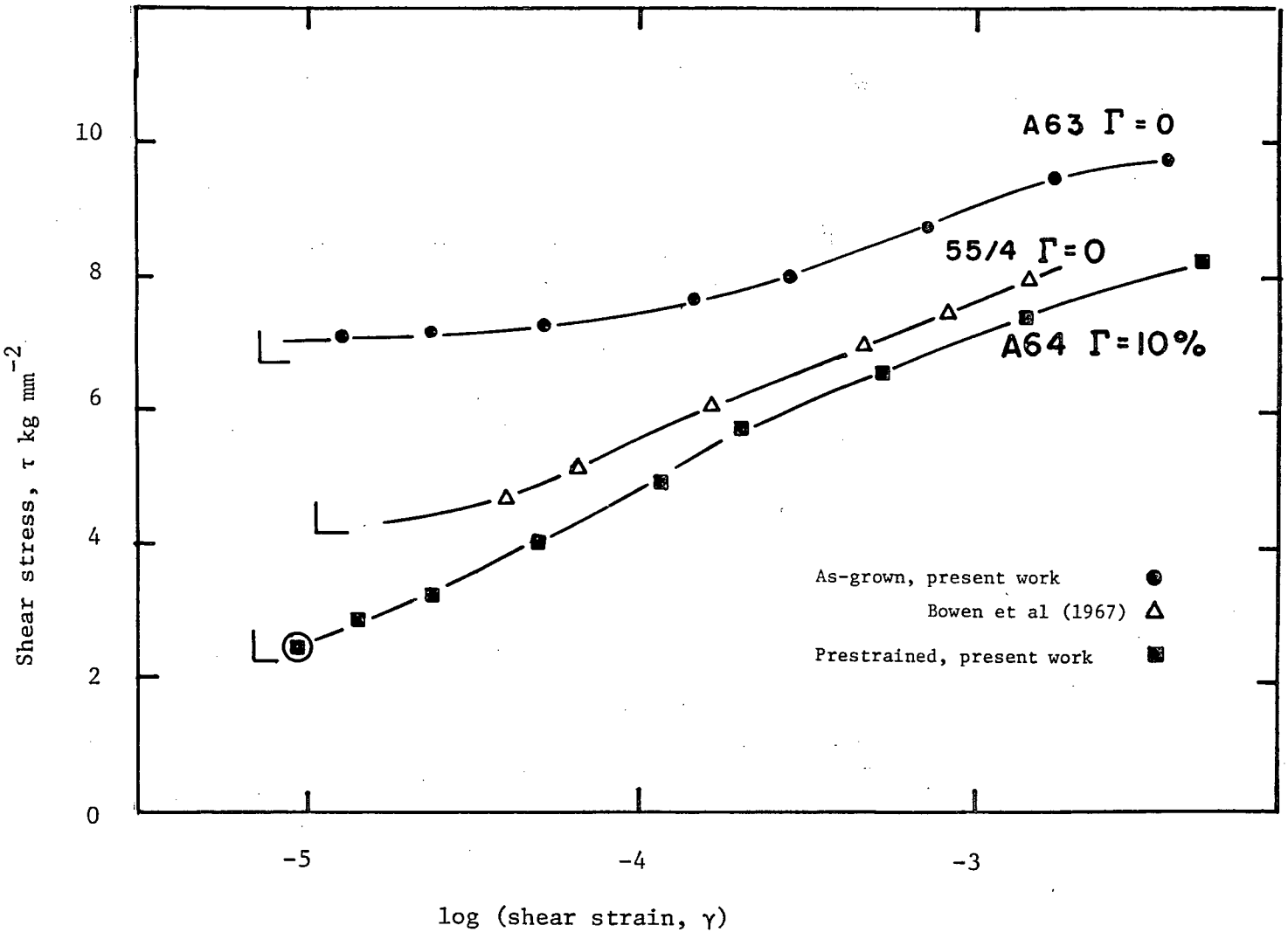

Fig 33. Microflow curves at 160°K for Nb crystals in different conditions.

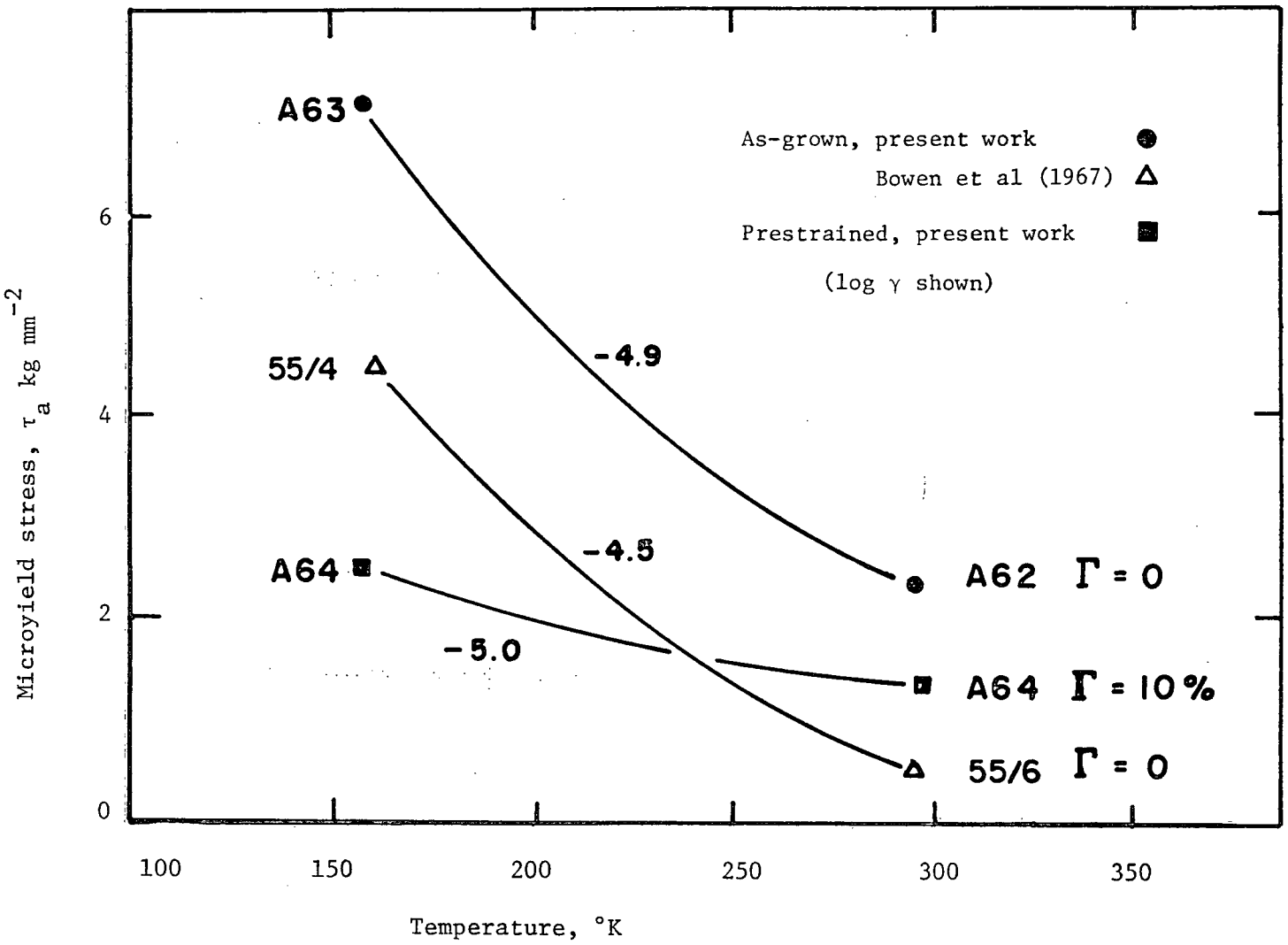

Fig 34. Microyield stresses at 160°K and 295°K for Nb crystals in different conditions.

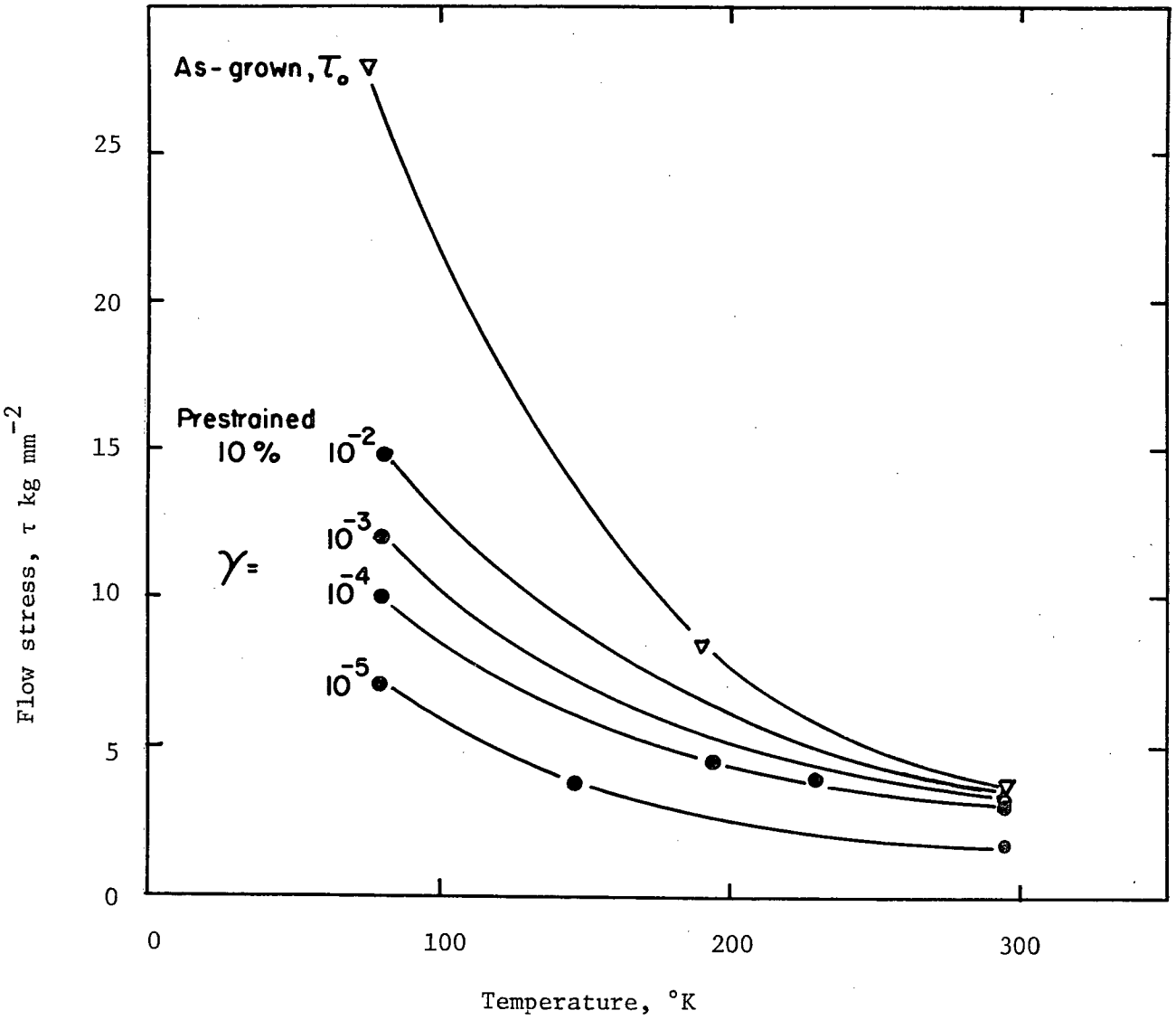

Fig 35. Flow stress at various strains as a function of temperature.

5.2.3 Strain-rate during microflow

For a given strain the slope of the microflow curve varies with temperature, and as a consequence the true plastic strain-rate will also vary with temperature. This is true because the constant crosshead rate $\dot{X}$ can always be expressed as the sum of the plastic strain-rate of the specimen $\dot{\varepsilon}_{p\ell}$ and the elastic strain-rate of the specimen plus machine $\dot{\varepsilon}_{e\ell}$:

ie $$\dot{X} = \dot{\varepsilon}_{p\ell} + \dot{\varepsilon}_{e\ell} \qquad (1)$$

By Hookes Law,

$$\dot{\varepsilon}_{e\ell} = \frac{1}{M}.\dot{\sigma} \qquad (2)$$

where M is an elastic modulus.

Changing from $\sigma(\varepsilon)$ to $\tau(\gamma)$, and substituting (2) in (1) gives

$$\dot{X} = \frac{1}{M.s}\frac{d\tau}{dt} + s\frac{d\gamma}{dt}$$

But

$$\frac{d\tau}{dt} = \frac{d\tau}{d\gamma}.\frac{d\gamma}{dt}$$

therefore

$$\dot{\gamma} = \frac{\dot{X}}{s + \frac{1}{M.s}(\frac{d\tau}{d\gamma})} \qquad (3)$$

Equation (3) shows that the true plastic strain-rate is a function of the slope of the microflow curve $(\frac{d\tau}{d\gamma})$. In fact, throughout straining in a tensile test, the plastic strain-rate will increase continuously from zero in the elastic region $(\frac{d\tau}{d\gamma} \to \infty)$ to a constant value determined by the crosshead speed at the asymptotic flow stress $(\frac{d\tau}{d\gamma} = 0)$.

In this work, it was possible to determine the true plastic strain-rate at any strain by combining the load-elongation data from the X-Y recorder with the load-time data from the Instron chart. It was found that at room temperature, the strain-rate was a similar function of strain for all specimens. An example is shown in Fig 36. At 77°K the strain-rate

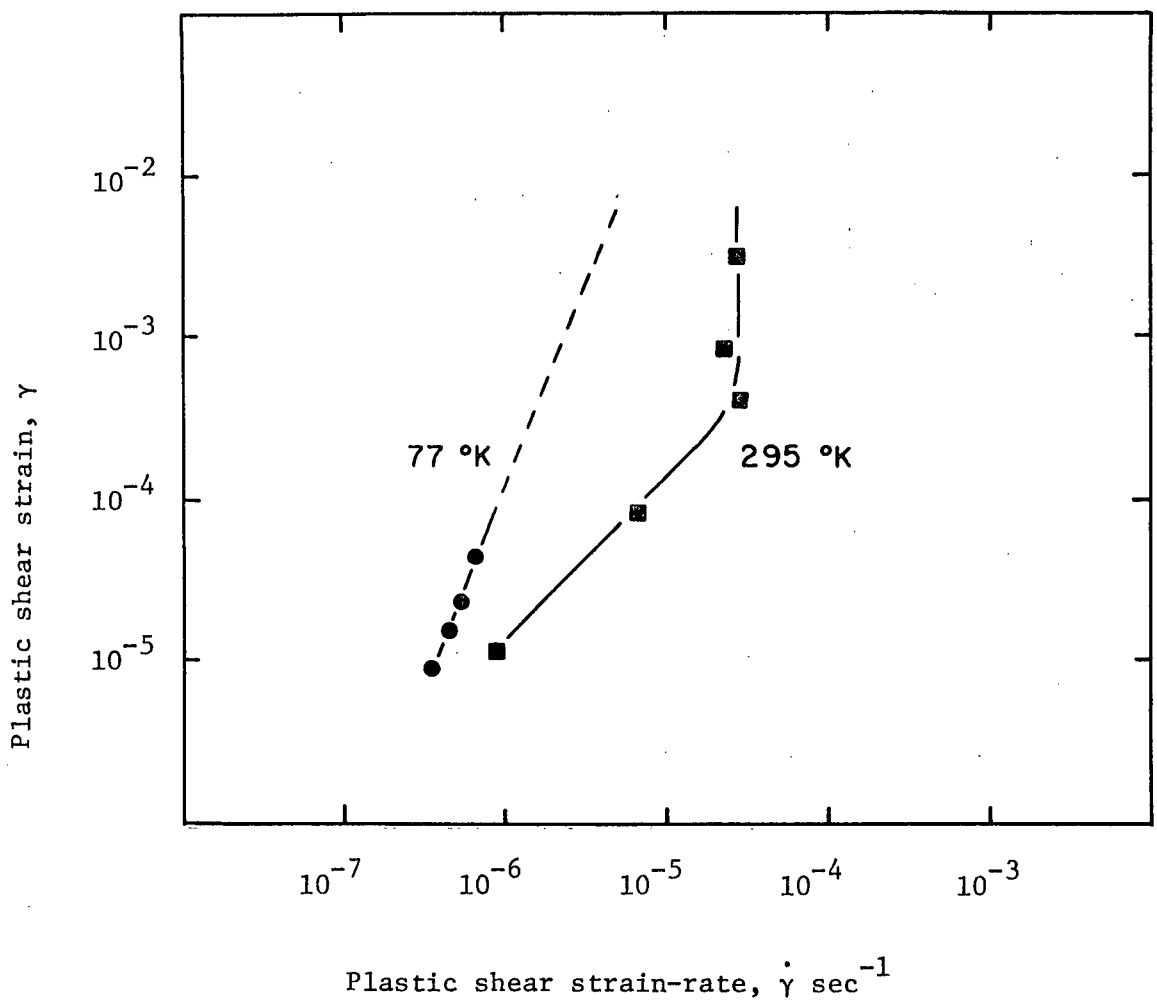

Fig 36. Instantaneous strain and strain-rate during microflow at 295°K and 77°K (Nb 4.8 Ta alloy).

does not increase as rapidly with strain as at 295°K, although the strain-rate at microyield is about the same at both temperatures. The maximum range of strain-rate over the whole microflow curve is about two orders of magnitude.

5.3 Discussion

5.3.1 Deformation at 295°K

The difference between the microflow curves for as-grown and prestrained crystals is of considerable interest (Fig 31). The increase in stress level at large strains ($\gamma \simeq 10^{-3}$) is readily explained by the expected increase in total dislocation density with prestrain. However the stress to produce a permanent plastic strain of $\gamma \simeq 10^{-5}$ has been almost halved by the prior deformation. As suggested in 5.1.5, this behaviour could be a consequence of a large increase in the number of dislocations which can move at low stresses. The behaviour is therefore similar to the effects observed in the preliminary microflow investigations of straining in stage I (see 5.1.4). It was found that the apparent microyield stress was very sensitive to the initial distribution of mobile dislocations.

It is generally supposed that dislocations move whenever the effective stress on them (τ^*) reaches a critical value given by the difference between the applied stress τ and the internal stress τ_μ. However, since the microflow stress is very dependent on the distribution of mobile dislocations, it is clearly impossible to assign a constant value to the internal stress during microflow. Only at large strains is it possible to assign a value to the internal stress; it has been confirmed that τ_μ is then independent of the initial distribution of mobile dislocations.

The concept of τ_μ could however be retained by considering both the "directional" and "adirectional" aspects of the internal stress field (on a scale involving larger dislocation motion than that previously considered in 5.1.1), defined by τ_μ^d and τ_μ^o, respectively. Thus, the value of τ_μ^d would be very dependent on the instantaneous distribution of moving dislocations: it would increase during microflow and decrease on unloading through relaxation. The adirectional component τ_μ^o would be independent of strain in the microflow region and would be influenced by, for example, the overall dislocation structure and the presence of solute atoms. It further follows that it is not possible to consider the effective stress τ^* in the microflow region of prestrained crystals.

The dependence of microyield on the local mobile dislocation density is not usually considered when interpreting microflow observations. For example, Prekel and Conrad (1968) and Stein (1968) have assumed that the same velocity versus stress relation for dislocations can account for the whole flow curve from microyield to macroflow. In other words, the whole microflow curve is simply a consequence of the increasing strain-rate during microflow (see 5.2.3) together with the strain-rate sensitivity (or dislocation velocity characteristics) of the material. In order to examine this hypothesis the strain-rate sensitivity of macroflow for prestrained crystals has been investigated in 3.4. (It was, in fact, found to be the same as that of as-grown crystals, which shows immediately that the as-grown and prestrained microflow curves cannot both be accounted for in terms of a strain-rate effect.)

Since the strain-rate during microflow has been established as a function of strain (Fig 36), it is possible to compare the stress versus strain-rate relation expected from macroflow experiments, with that observed from the microflow curves. This comparison is shown in Fig 37: the dashed

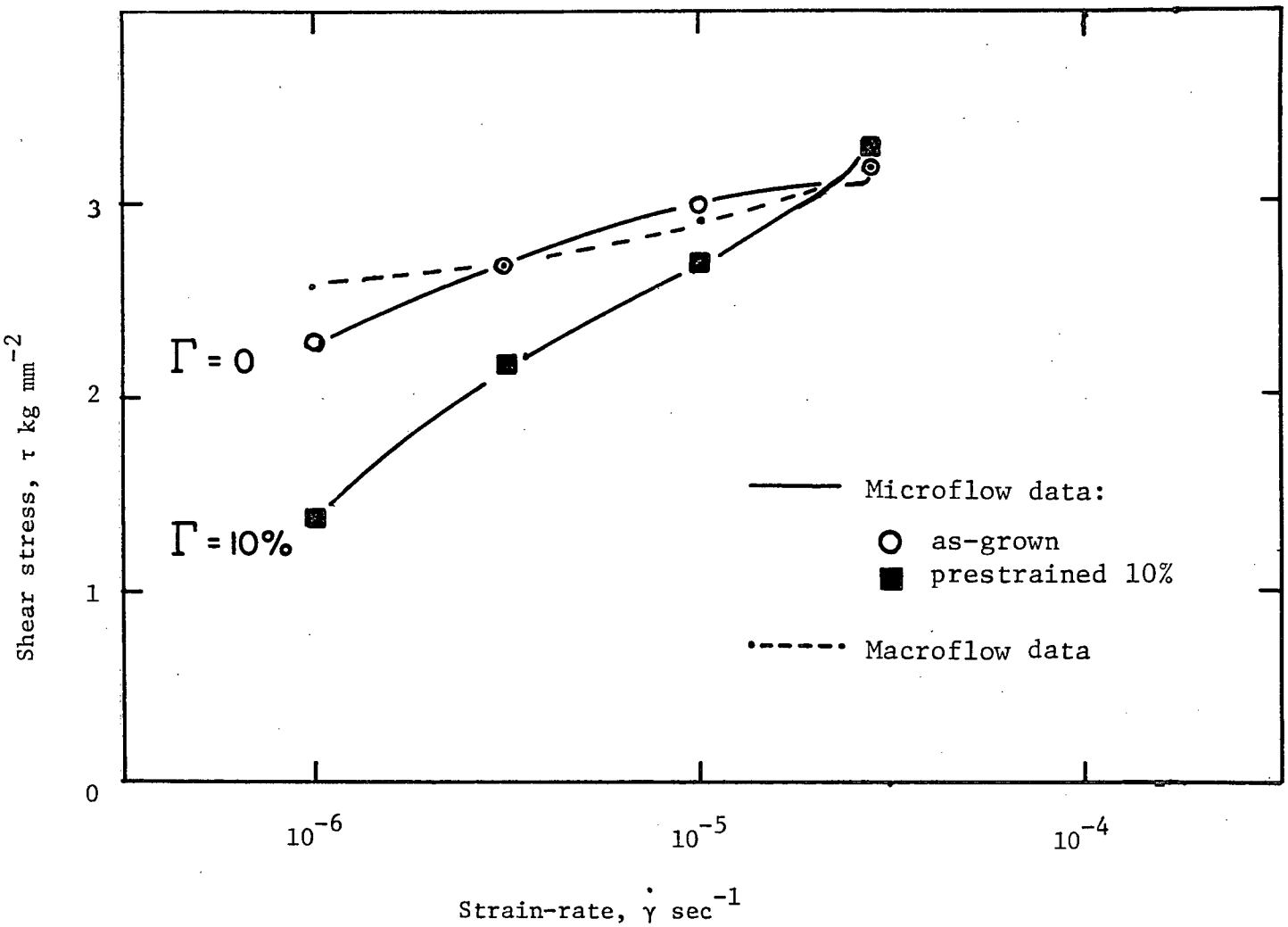

Fig 37. Comparison of observed microflow data at 295°K with macroflow predictions.

curve represents the expected strain-rate sensitivity of the flow stress (obtained from Fig 6) for crystal A62 which has an as-grown macroflow stress of 3.2 kg mm^{-2} (Fig 31) at a strain-rate of log $\dot{\gamma}$ = -4.55 (Fig 36); the solid curves show the observed stress versus strain-rate relations (obtained from Figs 31 and 36) for the same crystal in the as-grown and prestrained conditions.

It can be seen that the strain-rate sensitivity hypothesis (dashed curve) has predicted the observed microflow curve for the as-grown crystal, but there is a marked discrepancy in the case of the prestrained crystal. It therefore appears that for a prestrained crystal, the description of microplastic flow purely in terms of a strain-rate effect is incorrect. The discrepancy becomes more noticeable if comparisons are made at lower temperatures. The agreement between microflow and macroflow data in the case of as-grown crystals probably indicates that the same dislocation motion is involved in both cases. This would be expected if most dislocations in the as-grown crystal were initially locked and if microflow then represented mainly the multiplication and motion of screws.

5.3.2 Deformation at 160°K

As Fig 33 shows, the difference between the microflow characteristics of as-grown (A63) and prestrained (A64) crystals becomes more marked at low temperatures. Since the microyield stress in the prestrained crystal is about one-third of the value in the as-grown crystal, prestraining has clearly increased the number of dislocations capable of moving at low stresses. However it is quite striking to observe that at 160°K the prestrained impure crystal (A64) has a lower microyield stress than even the high purity specimen (55/4). This was not the case at 295°K. It therefore appears that at 160°K, prestraining is a more effective way of reducing the

effect of interstitials on those dislocations that move, than is increasing the purity. This would seem to be strong support for the recent suggestion of Kelly (1969) that even in the highest purity bcc materials, there are more than enough interstitials to effectively lock most of the dislocations, at least at low temperatures.

The role of interstitials in the deformation mechanisms of bcc metals may indeed be very important. Those workers who have studied only as-grown crystals and who claim that a Peierls mechanism is operative have taken support from the agreement betweeen data in the microflow and macroflow regions (Bowen et al (1967), Prekel and Conrad (1968)) while accepting other evidence for a Peierls mechanism in the macroflow region. However the alternative claim can now be made that, since impurity effects are so dominant in the microstrain region, they may be the dominant effect in macroflow as well.

5.2.3 Temperature sensitivity

It can be seen from Fig 34 that the temperature sensitivity of the microyield stress is the same in as-grown crystals of different purity, but is much less in impure prestrained crystals.

The decreased temperature sensitivity in prestrained crystals was first reported by Brown and Ekvall (1962). They concluded that the stress to move dislocations (Peierls stress) is not very temperature sensitive, and that the increasing temperature dependence at higher strains is a consequence of the temperature dependence of dislocation multiplication in the microflow region.

However another interpretation is that the fraction of dislocation line which moves may vary with temperature. As discussed in 5.1.5,

there is evidence (Solomon and McMahon (1968)) that at low temperatures the edge components have a higher mobility at small stresses. As the edge components become exhausted it is necessary for the screw components to move as well. For reasons still to be discussed, the screws require considerably higher stresses to move. This behaviour would give rise to the variation with strain of the temperature sensitivity of microflow as shown in Fig 35.

It therefore appears that if microyield in a fairly pure prestrained material represents the relatively uncomplicated motion of edge dislocations, then microstrain experiments will be very useful in determining the effects of impurities and alloying elements on dislocation motion.

6. MICRODEFORMATION OF NIOBIUM ALLOY CRYSTALS

6.1 Results

6.1.1 Deformation at 295°K

Microflow curves were obtained for the Nb alloys after prestraining $\Gamma = 15\%$ into stage I.

Typical curves for NbTa crystals are shown in Fig 38. The effect of the Ta addition has been to increase both the microyield and macroflow stresses by a comparable amount. This means that the effect of solute on the flow stress is not very dependent on the strain sensitivity, as illustrated in Fig 39. It should be noted that there is no evidence for a decreasing solute dependence of flow at high strain sensitivities.

Typical microflow curves for NbMo alloys are shown in Fig 40. Alloying has produced a very large increase in microyield stress and, as with the NbTa alloys, the concentration dependence of the flow stress is independent of the strain sensitivity (Fig 41).

6.1.2 Deformation below 295°K

Because of the low temperature brittleness of the NbMo alloys, experiments were performed only on the NbTa alloys.

Typical microflow curves for a Nb 4.8 Ta alloy deformed at various temperatures are shown in Fig 42. The form of the curves is qualitatively the same as that of pure Nb. In order to ascertain any effect of Ta, the microyield values are compared with pure Nb in Fig 43. It can be seen that the temperature sensitivity of microyield at very low temperatures is smaller for the alloy, which has a lower microyield value at 77°K. This behaviour is similar to that observed in the macroflow region (Fig 17).

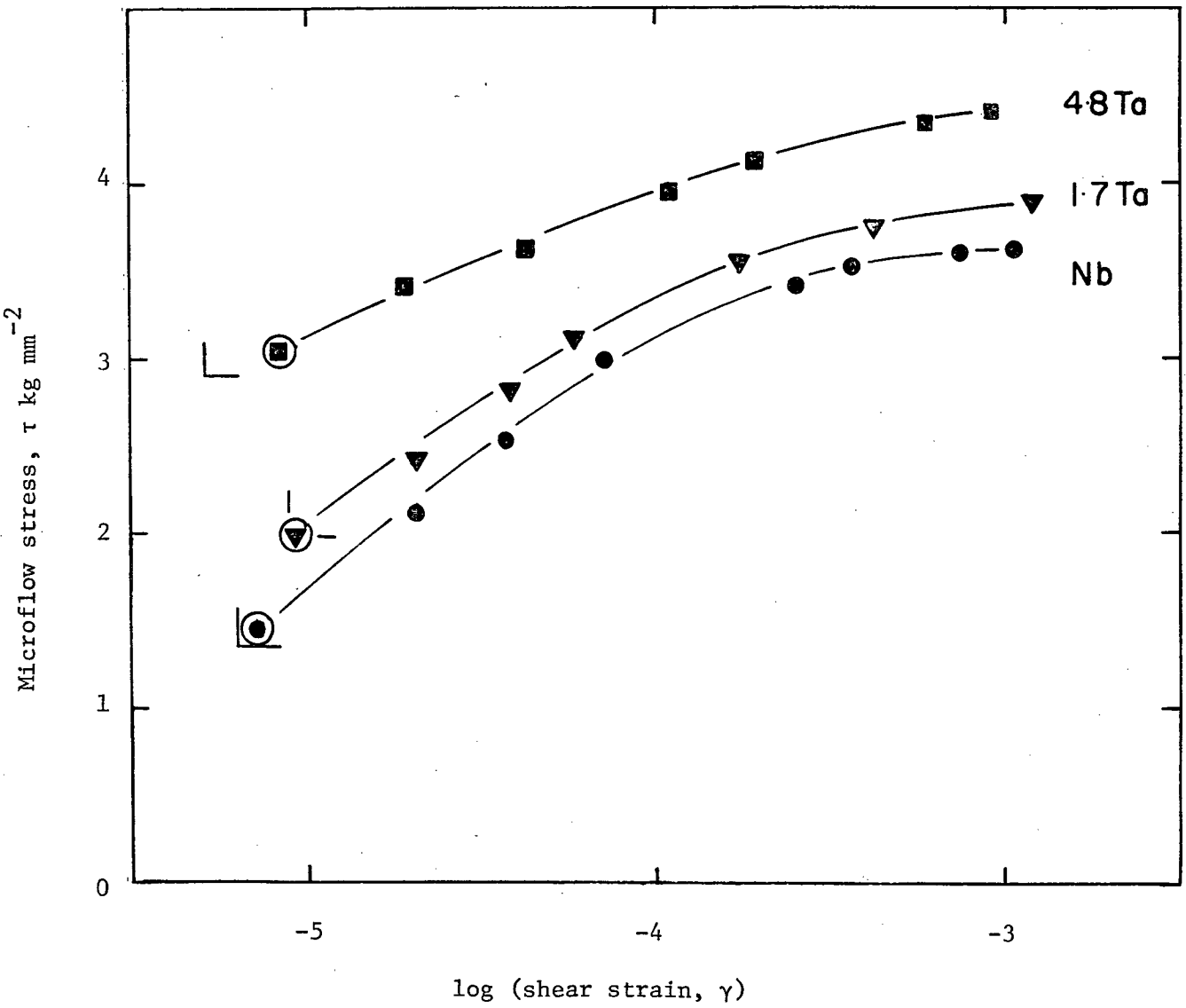

Fig 38. Microflow curves for NbTa alloys deformed at 295°K.

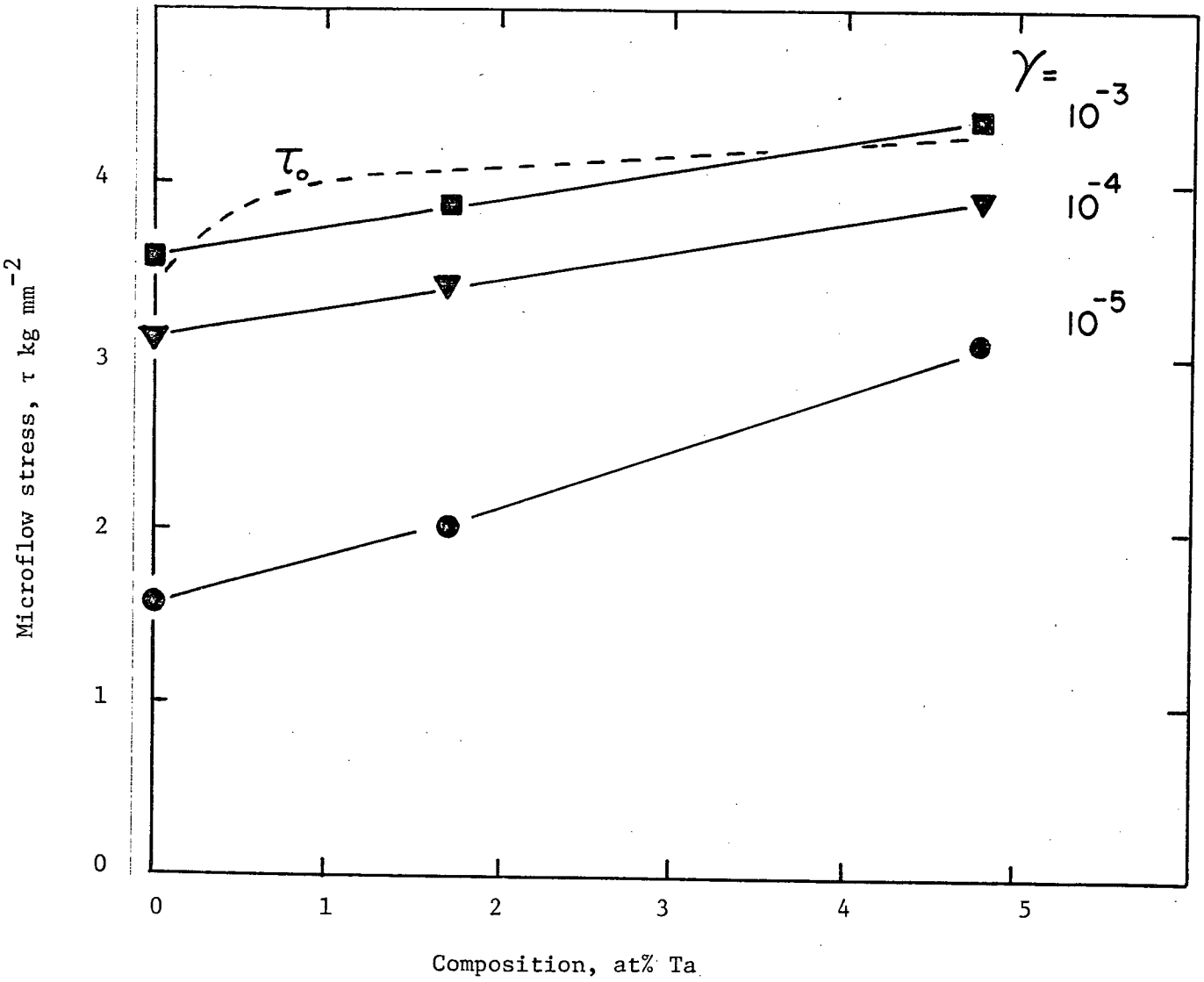

Fig 39. Microflow stress at different strains for NbTa alloys deformed at 295°K.

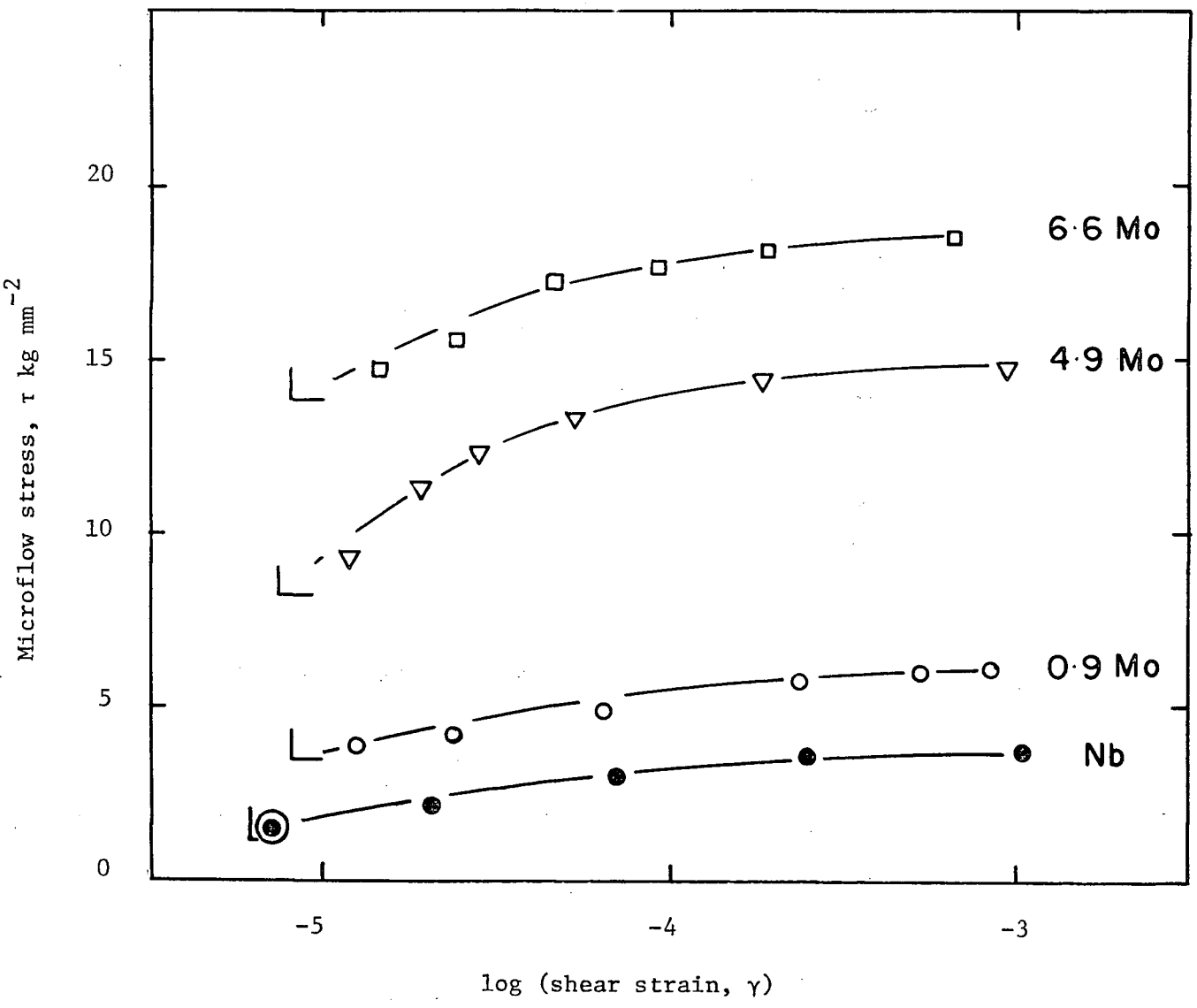

Fig 40. Microflow curves for NbMo alloys deformed at 295°K.

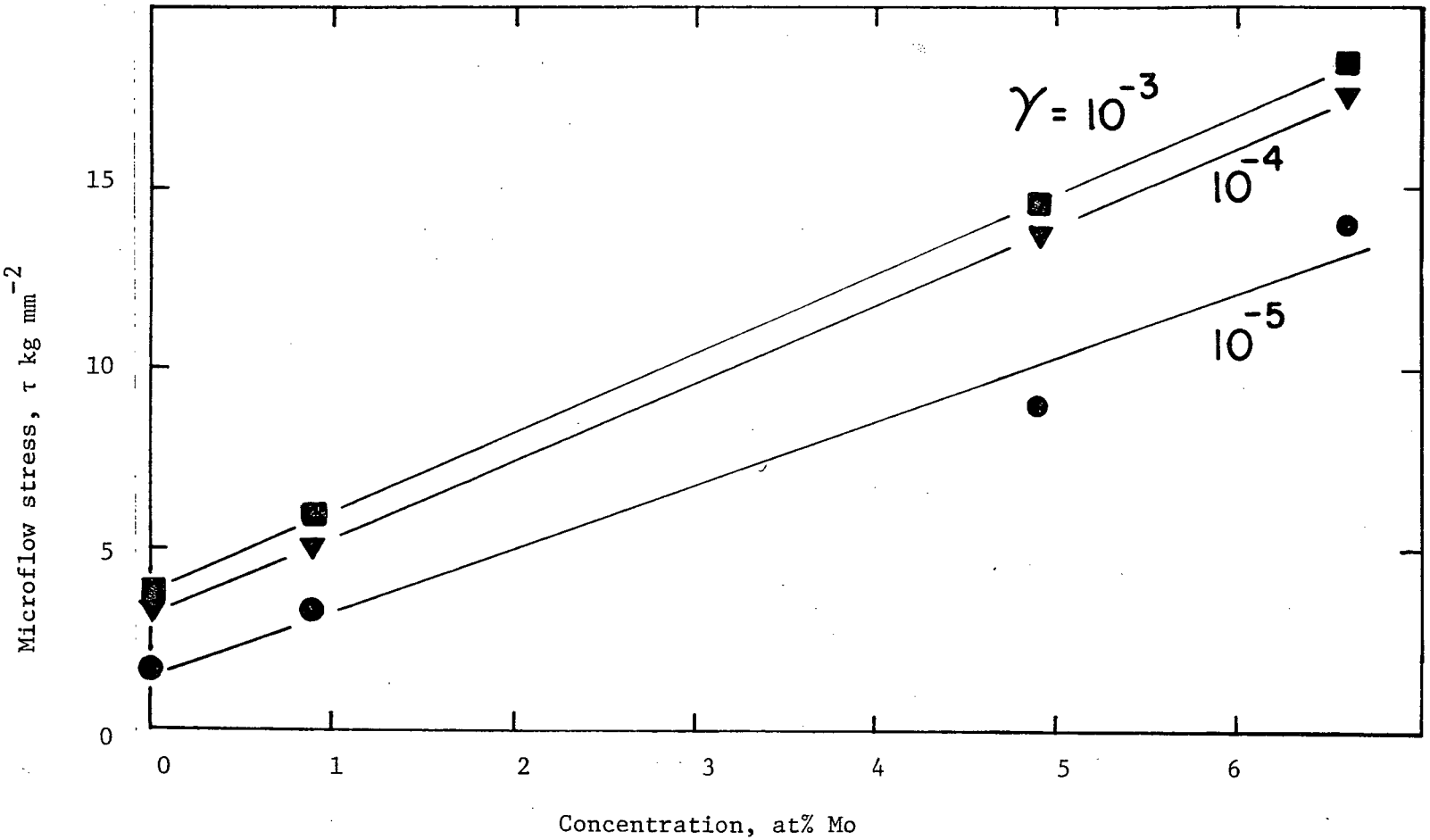

Fig 41. Microflow stress at different strains for NbMo alloys deformed at 295°K.

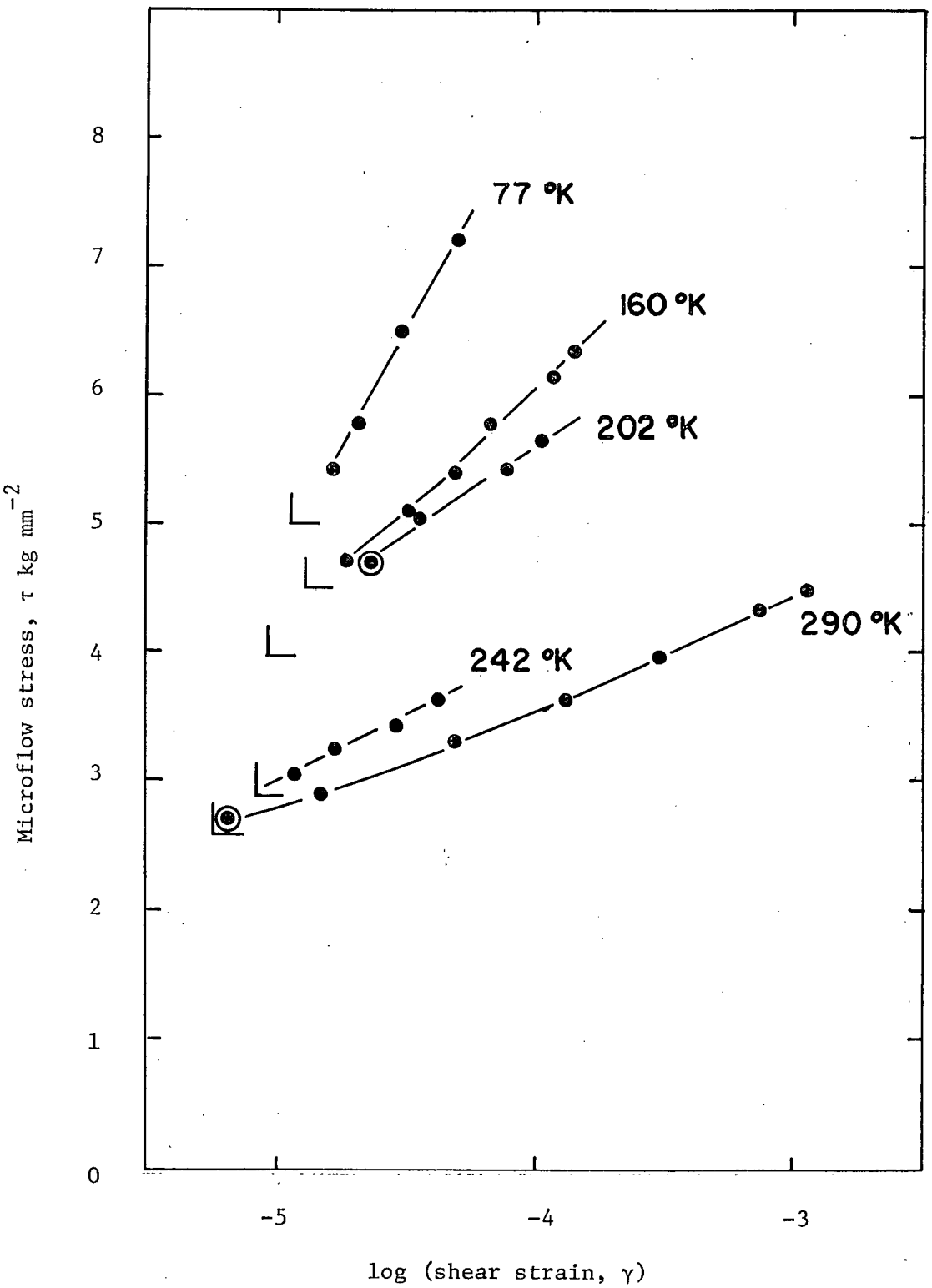

Fig 42. Microflow curves for a Nb 4.8 Ta alloy at low temperatures.

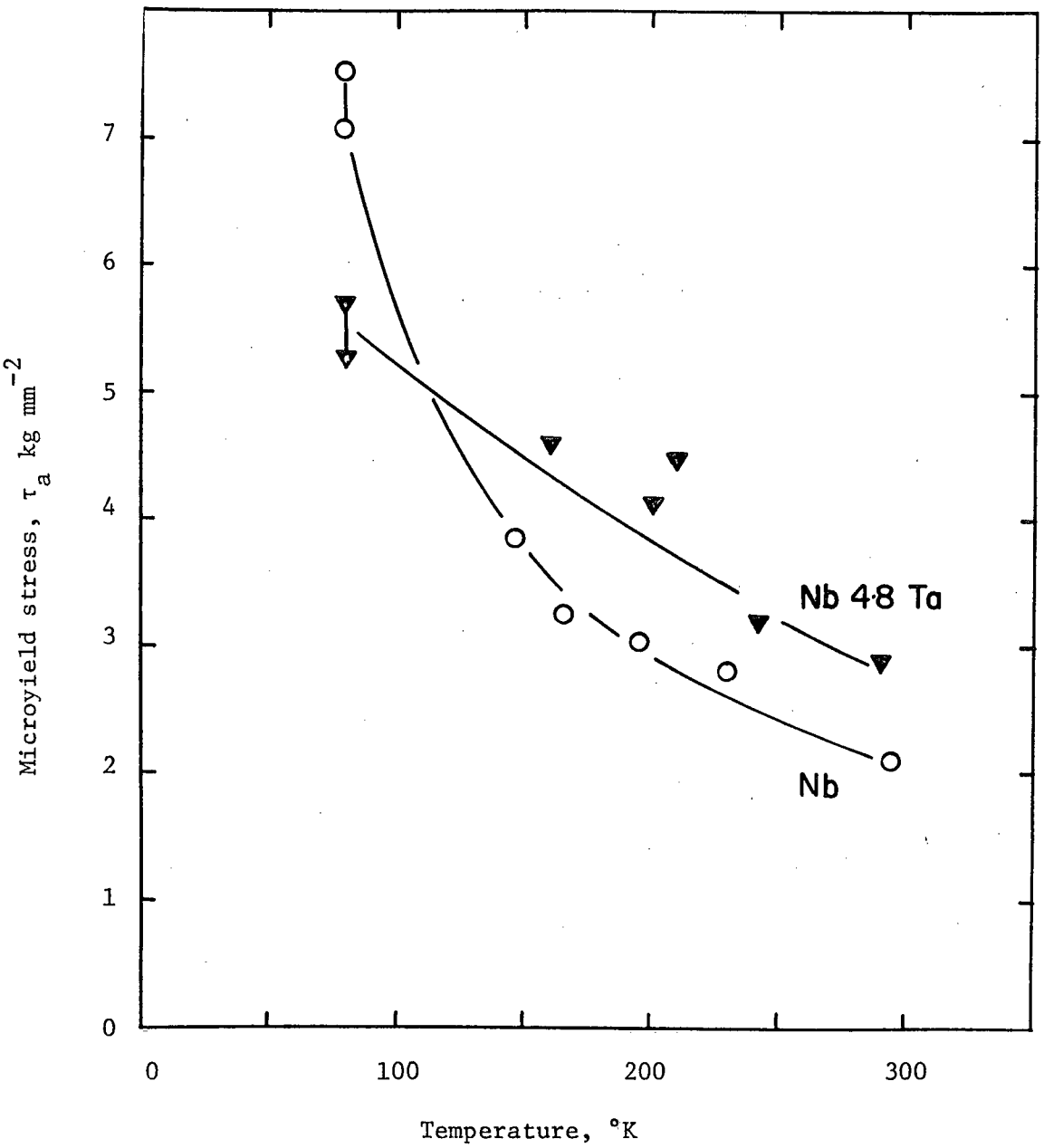

Fig 43. Microyield values (logγ = -4.8) for Nb and Nb 4.8 Ta crystals as a function of temperature.

6.2 Discussion

6.2.1 Deformation at 295°K

Microstrain experiments on bcc alloys have previously been performed by workers at the Ford Motor Company (Stoloff et al (1965), Davies and Ku (1966)) on substitutional alloys, and by Solomon and McMahon (1968) on interstitial alloys. In all cases the tests were performed on Fe-base polycrystals.

The results obtained by Davies and Ku were in general different both from those obtained in the present work on substitutional alloys and from those of Solomon and McMahon on interstitial alloys.

The technique used by Davies and Ku (and by Stoloff et al) to obtain microflow curves has already been criticized. However the stress at which they first recorded plastic strain should be a valid observation (although even this will be questioned later). Davies and Ku expressed their microflow curves on a linear strain scale and frequently made unjustifiable extrapolations to zero strain. In some cases, alternative conclusions become tenable when their data is plotted more suitably. However in the case of FeNi alloys the results are still very different from those obtained here for NbTa alloys (Fig 38) and NbMo alloys (Fig 40); Fig 44a illustrates a strong concentration dependence of flow at high strains which is considerably reduced at microyield. A similar though less pronounced behaviour was observed with FeC alloys.

From their treatment of the data, Davies and Ku claimed that the stress to move dislocations in Fe is independent of solute; solute restricts the ability of screws to cross slip and multiply so that macroflow is very concentration dependent. (This proposition would require that the directional

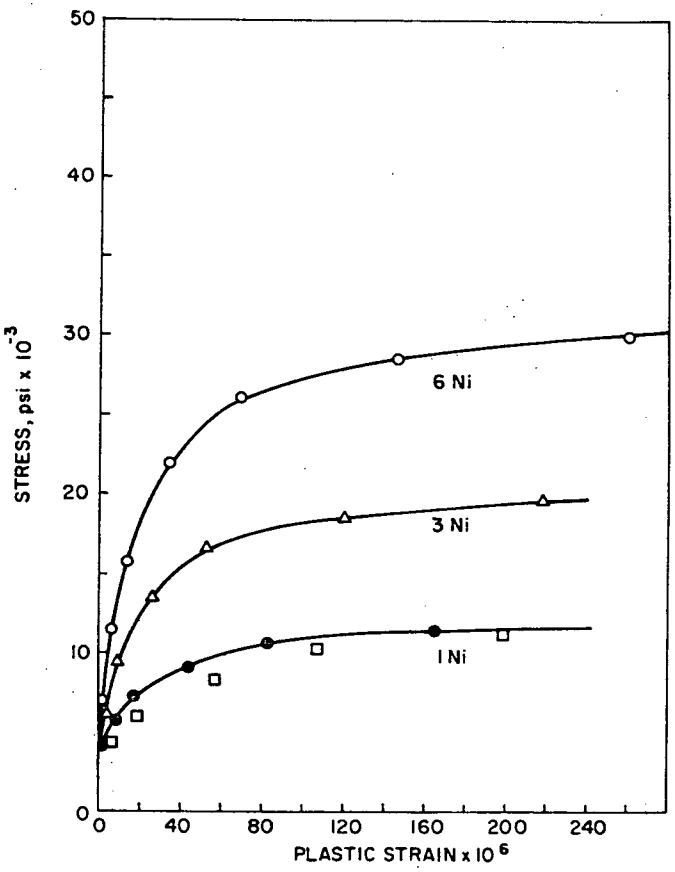

a) FeNi (from Davies and Ku (1966))

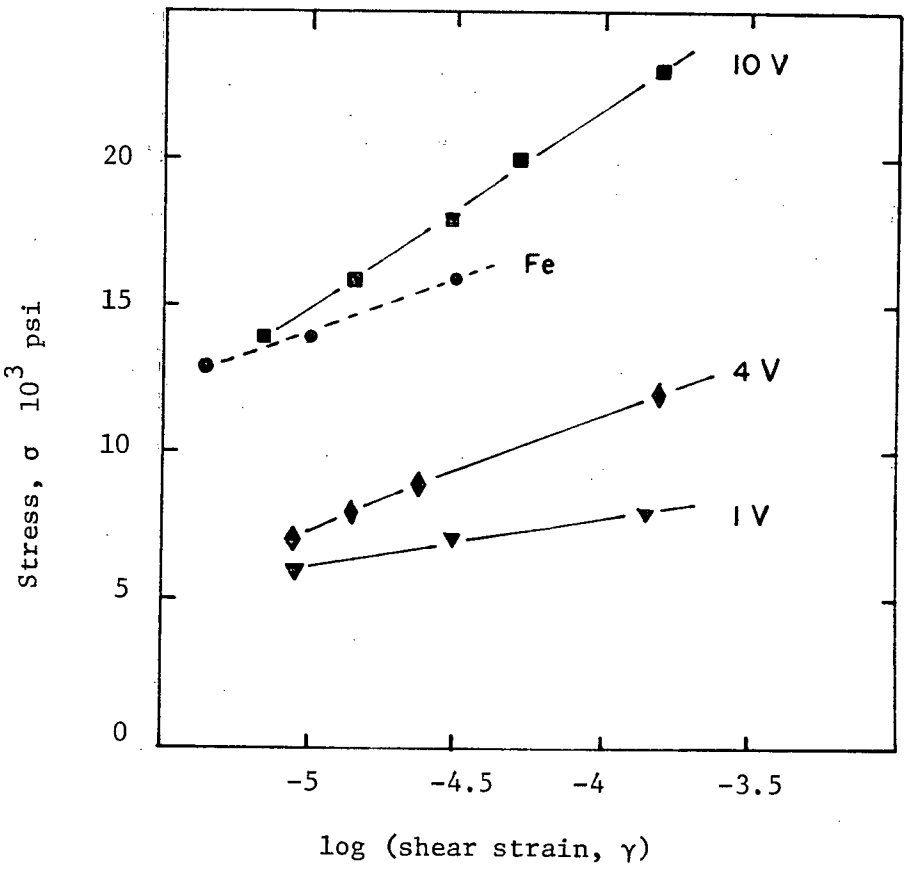

b) FeV (after Stoloff et al (1965))

Fig 44. Microflow data for polycrystalline Fe alloys deformed at 295°K.

internal stress component τ_μ^d be very concentration dependent.) They further proposed that the importance of dislocation multiplication is a fairly general phenomenon in determining the macroflow characteristics of bcc metals. Thus Davies and Gilbert (1967) found no orientation dependence of flow at microyield in Mo single crystals and attributed the effect at macroyield to dislocation multiplication during microflow.

The importance of dislocation multiplication as a rate-controlling mechanism in bcc deformation is an interesting suggestion, but it is not supported by the results of the present work or by those of Solomon and McMahon. These workers obtained values of σ_e and σ_a for various prestrained polycrystalline FeC alloys, and found a marked dependence of σ_a on C content. Their results are shown in Table III and are compared with those of Davies and Ku. Figs 45a and 45b have been taken from the work of Solomon and McMahon and show the microyield stress σ_a and macroflow stress σ_f at 77°K and 300°K for different FeC alloys. The results indicate that when the amount of C in the lattice increases, the microyield stress increases and approaches the flow stress. (The FeTi alloy contains relatively little C in the lattice since it is associated with the Ti.) On the other hand Davies and Ku did not observe a significant increase in microyield stress with added C.

In trying to resolve the above discrepancies, it is considered significant that Davies and Ku did not use prestrained specimens. They did not observe an initial yield point and therefore concluded that there was no dislocation locking. However, they used specimens in the form of strip only 0.006 inches thick, and it is common for yield points to be obscured in the presence of stress concentrations (Hutchison (1963)). As was indicated in 5.1.1, it is possible, in specimens which have not been prestrained, to obtain some plastic strain on the first loading at a stress

Table III. Comparison of microflow data for FeC alloys at 300°K obtained by Davies and Ku (1966) and Solomon and McMahon (1968).

Davies and Ku (unprestrained)			Solomon and McMahon (prestrained)			
		σ_a			σ_a	σ_e
Fe "pure"	(Q)	4	FeTi	(FC)	7	4
Fe 0.008% C	(Q)	3	Fe 0.006% (C + N)	(FC)	18	5
				(QA)	18	5
Fe 0.014% C	(Q)	5				
Fe 0.02% C	(Q)	8	Fe 0.035% (C + N)	(FC)	27	7
				(QA)	50	5
Fe 3.2% Si		32	Fe 3.1% Si	(FC)	40	27

Units: 10^3 psi, compositions in wt%

Q: quenched and held at -80°C

QA: quenched and aged 1 hour at 60°C

FC: furnace cooled

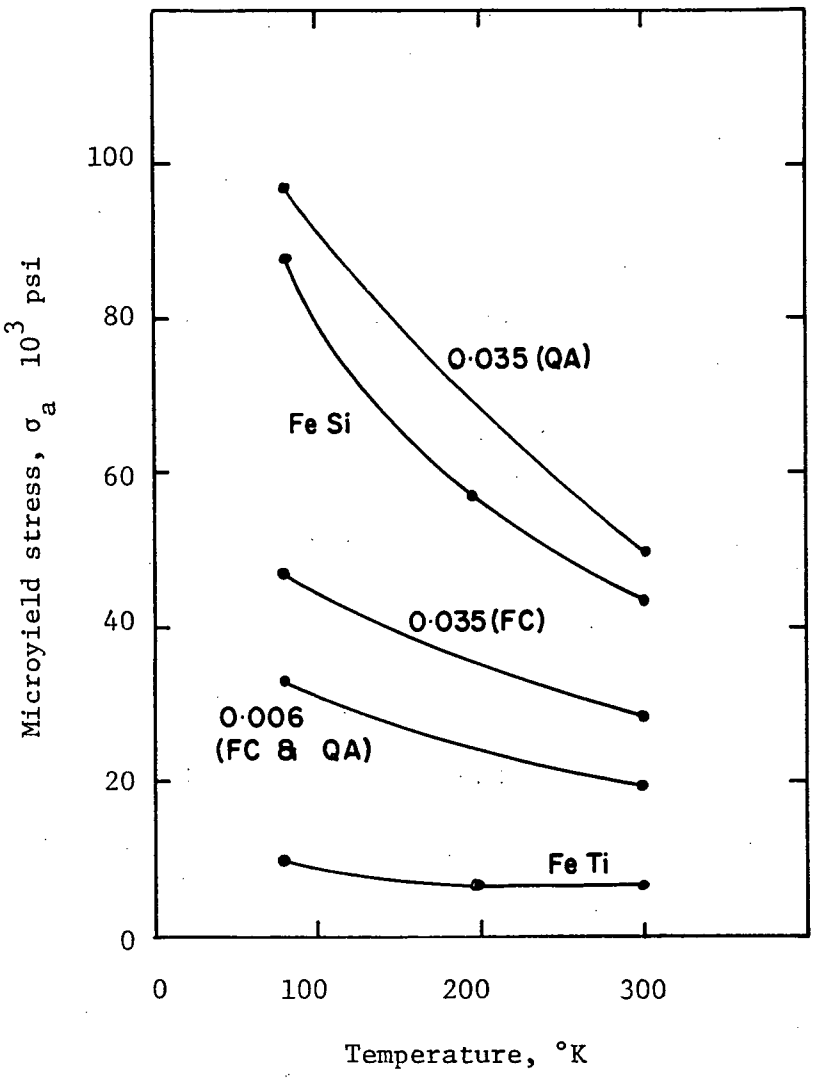

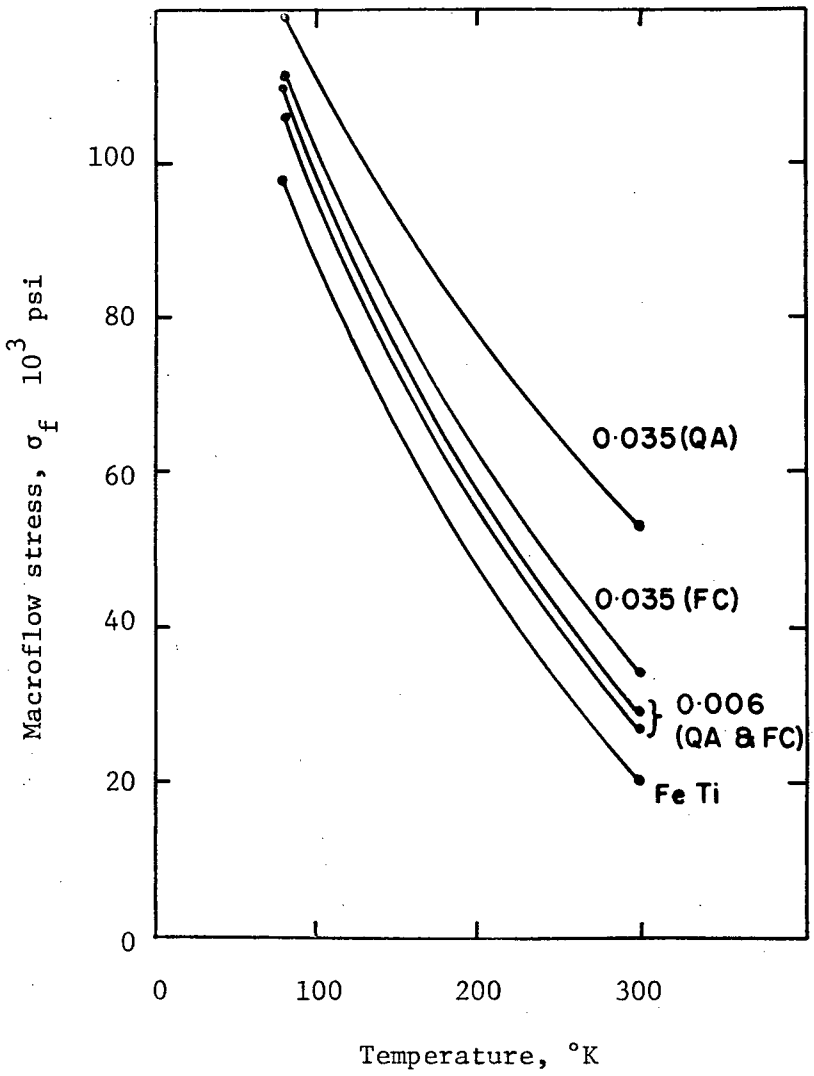

Fig 45. Temperature variation, in various prestrained Fe alloys, of:
a) microyield stress b) macroflow stress (after Solomon and McMahon (1968))
(Alloys identified in Table III)

corresponding to σ_e, before the establishment of a stable hysteresis loop. It is therefore quite possible that the "microyield" values of Davies and Ku correspond to σ_e rather than to σ_a. In fact, Solomon and McMahon found that σ_e was relatively independent of C content, and there is remarkable agreement between their σ_e values and the σ_a values of Davies and Ku, as shown in Table III.

This explanation of the anomalous microflow curves obtained by Davies and Ku is further supported by previous results reported by the same workers (Stoloff et al (1965)). In a study of microyielding in FeV and FeCo alloys, they used cylindrical specimens and prestrained them before testing. Their microflow curves for FeV alloys have been replotted in Fig 44b (in the manner adopted for this work), from which it can be seen that the microyield stress is very dependent on solute concentration, up to additions of 10%. This is now in agreement with the results of the present work, in which solute has been observed to raise the overall level of the microflow curve. It follows that the effect of solute is to increase the adirectional internal stress component τ_μ^o, with little effect on τ_μ^d. This is contrary to the proposition of Davies and Ku, and their suggestion that the main effect of solute is to restrict cross-slip of screw dislocations must be refuted. The present conclusion is in agreement with the results of slip line observations on the Nb alloys. There was no visible change in slip line structure and no tendency for slip to be restricted to {011}.

6.2.2 Deformation below 295°K

The results of low temperature microstrain experiments on NbTa crystals show that the softening observed in macroflow is also observed in the microflow region. Although the error in any yield determination

is greater at microyield than at macroyield, it is probable that the softening is greater at high strain sensitivities.

The softening of bcc metals has been frequently reported even at room temperature. For example, Fig 44b showed the effect of small additions of V to Fe polycrystals. Stoloff et al (1965) performed similar microstrain experiments at 77°K and found an even greater softening effect. Transmission electron microscopy revealed an increasing volume fraction of particles in the higher alloy specimens. Although these could not be analyzed it was concluded that they were compounds of V with C and N. An interaction between the solvent metal or solute metal with interstitials has been suggested for many other bcc systems; for example, VTi alloys (Fraser and Lund (1962)), and many alloys of Cr (Allen and Jaffee (1963)).

Since softening is observed during microstrain as well as macrostrain, it is suggested that the motion of both edge and screw dislocations is affected. This suggestion eliminates any interpretations based solely on the properties of screw dislocations.

7. THEORY OF PLASTIC FLOW IN NIOBIUM AND NIOBIUM ALLOY CRYSTALS

7.1 Mechanisms of deformation in pure niobium

7.1.1 Introduction

The exact nature of the mechanisms controlling the low temperature flow stress of bcc metals has still to be determined. As recent discussions have shown (Nabarro (1968)), there is at present no theory capable of explaining all the observations. Two extreme views are that the flow stress is controlled solely either by the intrinsic nature of dislocations in the bcc lattice (Peierls mechanism) (Conrad (1963)), or by the interaction of residual impurities with dislocations (impurity mechanism) (Fleischer (1967)). In most cases it is not possible to distinguish between the predictions of these theories by conventional mechanical testing. This has led to the use of many additional techniques such as transmission electron microscopy, dislocation displacement, internal friction, microstrain, and stress relaxation studies. However the limitations of such supplementary techniques are not sufficiently well understood for conclusive interpretation of the results to be made in favour of either theory.

The difficulties have been complicated by the recent discovery of unique characteristics of bcc metals such as the asymmetry of slip and the failure of the Schmid law of resolved shear stress. Furthermore, the experiments have been performed on a wide variety of both pure and impure bcc single crystals and polycrystals. As a result, the proponents have been forced to modify their particular theories to such an extent that they cease to have any predictive capabilities; it becomes hard to define what the theories really are. This complexity is reflected in the

terminology which has developed: modified-, pseudo-, or modified pseudo-Peierls stress.

The limitations of terminology are probably significant in the current controversy. For example, if it were established that screw dislocation motion involved an impurity-controlled recombination of partials and subsequent transfer to the next potential energy valley, would the process be described as a Peierls mechanism or an impurity mechanism? This comment illustrates the possible interdependence of specific mehanisms; present theories are incapable of accounting for this possibility. The following discusssion will consider all those factors which are significant in controlling deformation, rather than assuming that one mechanism is the complete solution.

7.1.2 Discussion

The microstrain evidence presented for pure Nb has indicated that, even in the highest purity materials tested to date, the effect of impurities is significant. It is therefore fallacious to assume that impurity effects can be neglected a priori, even if the material is extremely pure. Also the "effective" impurity content can differ from the analyzed impurity content: interstitials may be associated with solute atoms (eg FeTi alloys), or with solvent atoms (depending on the magnitude of the solubility limit), or with each other (in the form of clusters rather than as single atoms). The common practice of quoting impurity contents in weight fractions (wt ppm) and solute contents in atom fractions appears deliberately deceptive. Thus an impurity level of only 5 ppm hydrogen in niobium actually constitutes a Nb 0.05 at% H alloy.

In the work on FeC alloys, there was found to be a very marked effect of interstitials on the temperature dependence of τ_a, which has

been identified with a stress at which edge dislocations move. On the other hand, the effect of interstitials on the temperature dependence of the flow stress τ_f was relatively small. It is possible that the relative insensitivity of $\frac{d\tau_f}{dT}$ to impurities could result from the saturation of a screw dislocation-interstitial interaction at very low concentrations. This would require that the interaction between dislocations and interstitials be much stronger for screws than for edges. It would then be necessary to achieve a considerable increase in overall purity for the flow stress τ_f to show a similar dependence on purity as the microyield stress τ_a. In fact, as was shown in Fig 5, there is strong evidence for a decrease in $\frac{d\tau_f}{dT}$ with increasing purity at low temperatures.

Although the $\tau_o(T)$ curve can be divided into thermal and athermal regions, the assignment of thermal and athermal stress components at temperatures below T_o requires caution. It has been seen that a unique value cannot be ascribed to the internal stress field τ_μ during microflow, because the flow stress is influenced by the particular distribution of moving dislocations. The constant effect of τ_μ can be felt only when dislocations move long distances through the crystal at the asymptotic flow stress τ_f^o in a prestrained crystal. At 295°K this stress is reached after a strain of about $\gamma = 10^{-3}$. However at low temperatures the strain to reach τ_f^o may be much larger, so the influence of the particular dislocation distribution may be felt even at macrostrains ($\gamma > 10^{-3}$). To the extent that this is true, the apparent value of τ_μ will be temperature dependent. In fact the assumption that τ_μ varies with temperature only as the shear modulus implies that work hardening (given by $\frac{d\tau}{d\gamma}$) is independent of temperature; this is certainly not the case (see Fig 42).

Thus although the dislocation density (which influences τ_μ^o) has been found to be independent of deformation temperature (Keh and Weissman (1963)), there is a change in dislocation configuration (Lawley and Gaigher (1964)) which could influence τ_μ^d. Also the relaxation of dislocation groups during deformation at low temperatures could be slower than at high temperatures.

Another difficulty with the interpretation of τ_μ even at temperatures near T_o, is that τ_μ can be applied to dislocation interactions over both short and long distances. Consider the effect of two obstacles to dislocation motion which could influence τ_μ: the overall dislocation structure and single solute atoms. The influence of a dislocation group can be felt over long distances, and is usually described as the internal stress field (proportional to $\rho^{\frac{1}{2}}$). This interaction should be similar for both edges and screws. However another contribution to the internal stress field arises from the presence of solute atoms. The effect of a single solute atom on a dislocation line is felt only at close distances of approach and the interaction could well be different for edges and screws (eg Fleischer (1963) model). Both these interactions are effective at temperatures above T_o; they can be overcome only by an applied stress. They are therefore described as "long range" interactions, although the dislocation may feel the solute atom only at very close distances.

It is of interest to note that this difficulty with the spacial extent of an interaction does not arise in the statistical theory of the flow stress developed by Kocks (1966, 1967). His theory describes the flow stress in terms of an effective obstacle spacing through which dislocations must pass and the hardness of the obstacles themselves. When, as in the above case, different kinds of obstacles can contribute to the flow stress, Kocks (1968) found that their contributions are additive

whenever the spacings of the respective obstacles differ significantly, irrespective of the distance over which the obstacle-dislocation interaction occurs.

There appear to be the following possible contributions to the temperature dependence of the flow stress of bcc metals:

a) short range interstitial-dislocation interaction, which will be further discussed later,

b) temperature dependent "long range" stress, which has been discussed above,

c) inherent lattice friction.

This last possibility is often expressed in terms of the restriction of screw dislocation motion at low temperatures. Although dissociation of dislocations in bcc crystals must be extremely slight if it occurs at all, the concept of partials existing on planes other than the glide plane has been quite successful in explaining both the anisotropy of critical shear stress with respect to the sense of shear, and the orientation dependence of the resolved shear stress (Kroupa and Vitek (1967)). Screw dislocation motion has been thought to occur by thermally activated transitions from sessile to glissile configurations of the dissociated screws (Bowen et al (1967)). This theory is in agreement with the observed restriction of slip to {011} planes at low temperatures, since it is possible that the reduced ability for cross-slip produces a large increase in flow stress. It is agreed that the motion of screw dislocations is rate-controlling at low temperatures, but it is not necessarily true that the high flow stress is a consequence of the restricted ability of screws to cross slip. For instance the addition of 6.6 at% Mo to Nb produced a six times increase in flow stress at room temperature without any apparent change in the wavy slip traces left by screw dislocations.

7.2 Mechanisms for deformation of niobium alloys

7.2.1 Substitutional effects

7.2.1.1 Introduction

The change of flow stress on alloying a pure metal is due to an interaction between the solute atoms and the dislocations. The possible interactions have been established for fcc metals and to a lesser extent for hcp metals (Haasen (1965)). There is relatively little data available on bcc substitutional alloys, but some attempts have been made to determine the important interactions (Harris (1966), Kostorz (1969)). Since there appear to be no additional effects involved in bcc alloys, the mechanisms established for fcc systems have been tabulated and their relative importance indicated for both fcc and bcc substitutional alloys (Table IV).

The table shows that in bcc alloys the important interactions are due to the size and modulus differences of the solute atom and possibly also to an interaction with the dislocation core. The size and modulus differences are "long range" effects, in that the interaction can be overcome only by an applied stress, at least at moderate temperatures. Therefore in the region of T_o (450 - 550°K for Nb alloys) only the long range interactions can produce hardening.

The core interaction is a "short range" effect and, being capable of thermal activation, will be apparent only at low temperatures.

7.2.1.2 Long range interactions

The effect of the different size of the solute atom is measured by the size misfit, δ, defined as the relative change of lattice parameter

Table IV. Possible interactions between solute atoms and dislocations in fcc and bcc metals.

Solute effect	Range of interaction	Importance of interaction	
		fcc	bcc
Size difference	long	moderate	large
Modulus difference	long	large	small
Core interaction	short	moderate	may be moderate
Chemical interaction	short	moderate	negligible
Short range order	short	small	very small
Grown-in dislocation density (indirect effect)	-	very small	very small

on alloying:

$$\delta = \frac{1}{a}\left(\frac{da}{dc}\right) \qquad (1)$$

Similarly, the modulus defect, η, is defined as the relative change in shear modulus on alloying:

$$\eta = \frac{1}{\mu}\left(\frac{d\mu}{dc}\right) \qquad (2)$$

The necessity for both these parameters was first recognized by Fleischer (1961,1963). He used a model for the long range elastic interaction between dislocations and solute atoms to derive an expression for the critical resolved shear stress of an alloy, given by

$$\tau_o = Z.\mu.\varepsilon^{3/2}.c^{1/2} \qquad (3)$$

where c is the atom fraction of solute

μ is shear modulus

Z is a numerical constant ($\simeq \frac{1}{760}$)

ε is a misfit parameter.

Equation (3) has been found to be a good description of the parabolic hardeing behaviour observed in copper-base and silver-base alloys (Haasen (1968)). To obtain the best correlation, the misfit parameter combines the effect of size and modulus differences, and is given by

$$\varepsilon = \left| \eta' - \alpha.\delta \right|$$

where $\eta' = \dfrac{\eta}{1 + \frac{|\eta|}{2}}$

and $\alpha = +3$ is appropriate for an interaction between solute atoms and screw dislocations.

It has therefore been concluded that in Cu and Ag alloys the hardening is produced by an elastic interaction between solute atoms

and screw dislocations. Furthermore, the modulus effect produces about 75% of the total hardening. (To a first approximation, a size effect alone does not predict any interaction with screws; the original Mott and Nabarro (1948) theory considered only size effects.)

The applicability of equation (3) has since been tested for bcc alloys. Harris (1966) found that in polycrystalline Nb solid solutions, in contrast to fcc alloys, the size misfit rather than the modulus defect was the dominant factor. Raffo and Mitchell (1968) reviewed several single crystal studies and concluded that hardening was due only to the interaction of misfitting solute atoms with edge dislocations (cf Mott and Nabarro). However this clearly cannot account for the observed hardening in NbTa alloys, for which δ is zero.

A more recent attempt by Kostorz (1969) to correlate experimental data with equation (3) has indicated the importance of both δ and η in determining the solution hardening of bcc solid solutions. However so many ad hoc modifications were required for particular alloy systems, that serious doubts must be expressed as to the applicability of the Fleischer analysis. Although, as Kostorz suggested, it is true that much more data on bcc solid solutions is required, it also appears that correlation of data on the lines he has attempted will become even more complicated than at present. The following are specific criticisms of the methods adopted to date:

a) It is clear that hardening does not always follow a parabolic law (NbMo, present work; TaRe, Mitchell and Raffo (1967)); therefore in such cases correlation with equation (3) should not be attempted.

b) In the absence of experimental data, the modulus defect is usually calculated assuming a linear variation of the modulus between the pure components of an alloy showing complete solid solubility. This could be a source of error, but more important is the lack of consistency in the expressions used for the modulus.

The following table shows the different expressions which have been used by various workers; there is a large discrepancy in the value of η calculated, as an example, for NbTa alloys.

				η
Harris:	Youngs modulus	=	$\frac{1}{S_{11}}$	= -0.07
Mitchell and Raffo:	Shear modulus on (011) in $[1\bar{1}1]$	=	$\frac{1}{3}(C_{11} - C_{12} + C_{44})$	= +0.36
Kostorz:	Voigts average shear modulus	=	$(C_{44} \cdot \frac{C_{11} - C_{12}}{2})^{\frac{1}{2}}$	= +0.64

It is suggested that Voigts average shear modulus (see A.5.2) is the best expression to use; the expression used by Mitchell and Raffo concerns the operative slip system, which does not enter into the calculation of the dislocation-solute interaction in the Fleischer model.

c) The Fleischer model allows variations in the misfit parameter ε depending on whether edge or screw dislocation interactions are considered to be dominant. However if it becomes necessary to consider different combinations of edge and screw interactions for different alloy systems (Kostorz (1969)), there are then so many independent variables that the model ceases to have any predictive value.

It is important to recall that the microstrain experiments on NbTa and NbMo alloys revealed the same concentration dependence of microyield as macroflow. Assuming that microyield represents the motion of edges

and macroflow represents the motion of screws, this is experimental evidence for a similar interaction of solute with both edges and screws.

At present there seems to be no satisfactory theory for substitutional solution hardening in bcc alloys. It is possible that the statistical theory of alloy hardening, which has been applied to dispersion and precipitation hardened alloys (Kocks (1969)), could be extended to the case of solution hardening. However the applicability of the theory becomes increasingly limited as the penetrability of the obstacles to dislocation motion increases; single solute atoms represent the most unfavourable case. Kocks has recognized that the statistical theory is not applicable to deformation by the spreading of a Luders band, which often occurs in alloys. His theory suggests that this mode of deformation may be a consequence of the greater mobility of screw dislocations so that the edges are rate-controlling. This is not supported by the results of the present work: the formation of a Luders band has been shown to be a geometrical phenomenon determined by the relative values of yield stress and work hardening rate; screw dislocations are rate-controlling in both pure Nb and the alloys.

7.2.1.3 Short range interaction

At low temperatures as the effect of thermal activation is reduced, a possible interaction between solute atoms and the dislocation core becomes evident. Thus solution softening has been observed in NbTa alloys at 77°K and has been reported in many other bcc systems.

It has been commonly supposed that addition of solute leads to a reduction in the Peierls stress (Mitchell and Raffo (1967)). However it was shown in 4.2.1.2.2 that this possibility would still require a minimum in the Peierls stress versus concentration curve; arguments to

explain the effect of solute can only predict a continuous decrease in Peierls stress (Arsenault (1967)).

Ravi and Gibala (1969) have presented data obtained by Koss (1969) for the critical resolved shear stress of NbW single crystals at low temperatures (Fig 46). It is possible to extrapolate the alloy curves to zero solute, giving a value for pure Nb which is very close to the purest materials tested to date. Similar extrapolations were possible with the NbO single crystal alloys studied by Ravi and Gibala. In particular, they observed that the effect was not reversible: addition of solute produced softening but subsequent purification did not produce hardening. They concluded that in both cases the softening was due to association of interstitial atoms (with either substitutional solute atoms or with other interstitial atoms), leading to a reduction in the number of barriers over which the dislocation must pass. At higher solute concentrations the association reaction becomes saturated and hardening occurs.

This conclusion is in agreement with the role of interstitials already outlined in this discusssion. Possible dislocation-interstitial interactions will be further discussed below.

7.2.2 Interstitial effects

The importance of interstitials in Nb has become increasingly evident during the preceeding discussions of plastic deformation. The role of interstitials has, however, also been inferred from other experiments. In internal friction studies, a Snoek damping peak is observed when the frequency of the stress equals the frequency at which the interstitials jump from one site to another. Of particular interest is the result of detailed analysis of damping curves (Gibala and Wert (1966)),

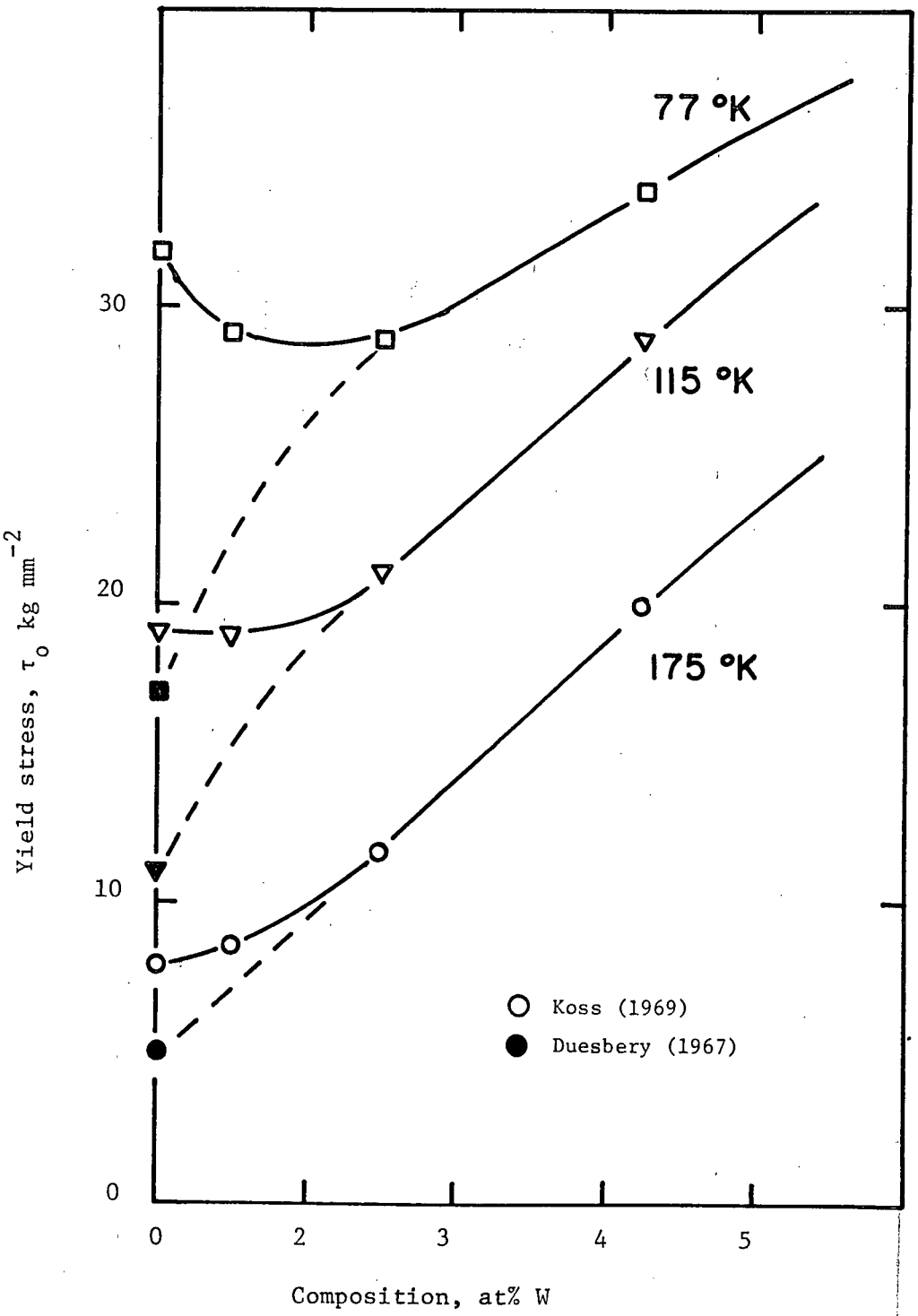

Fig 46. Yield stress of NbW alloys at low temperatures. (after Koss (1969))

namely that interstitial atoms in bcc metals are present both as single unassociated atoms and as clusters containing from two to four atoms. Similar results have been obtained from direct studies in the field-ion microscope (Nakamura and Muller (1965)). Such associations could influence the effective interstitial content, as already suggested.

As in the case of substitutional atoms, there could be an interaction between dislocations and interstitials due to both the size and modulus differences. However the modulus effect is very small; the size effect can be evaluated on an isotropic continuum approximation, if it is assumed that the interstitial produces isotropic dilatation only (Cottrell and Bilby (1949)). However in actual anisotropic crystals, the stable interstitial configuration can have tetragonal symmetry and the interstitial would then react with shear stresses as well as normal stresses. An approximate elasticity calculation was performed by Cochardt et al (1955) and was later applied by Schoeck and Seeger (1959) and Fleischer (1962). The large tetragonal distortion in bcc metals is produced by interstitials in the $(\frac{1}{2},0,0)$ octahedral positions; a smaller distortion is possible in the $(\frac{1}{2},\frac{1}{4},0)$ tetrahedral positions. Interstitials in the octahedral sites occupy equivalent positions, 120° apart, in the neighbourhood of a screw dislocation. The maximum interaction energy has been calculated to be about the same for both edge dislocations and screws.

In addition to interstitial interactions with the elastic strain fields of dislocations, interactions are also possible with the dislocation core, where elastic calculations break down. Atomic calculations for possible core states are very difficult to perform; attempts have been made by assuming a particular representation for the interaction between atoms, such as a Morse function (Doyama and Cotterill (1968).

At low temperatures, interstitials are potent hardeners of the hcp metals Zr, Ti, and Hf in which the effect is mainly on the thermal component of the flow stress (Tyson (1967)). Tyson found that application of the elastic calculations of Cochardt et al resulted in an interaction which was too small to account for the observed effects. The hardening was concluded to be due to a short range interference by solute atoms with the atomic core of gliding dislocations, although no quantitative description was possible.

The situation is more complicated in bcc metals because interstitial atoms have an athermal as well as a thermal effect. Furthermore the interaction of interstitials must be stronger with screws than with edges to explain the microstrain evidence. In the absence of calculations involving the dislocation core, there exists no satisfactory theory at present. However, further attempts at elastic approximations have revealed some interesting agreements with experimental observations:

a) An attempt to relate the interstitial-dislocation interaction to the cross-slip of screw dislocations has been made by Formby (1966).

Fig 47a shows a section through a $[\bar{1}11]$ screw dislocation on $(01\bar{1})$. The possible cross-slip planes are taken to be $(1\bar{1}0)$ and $(\bar{1}01)$. As the dislocation moves from A to B the stress at the dislocation due to impurity atoms in the three equivalent $(\frac{1}{2},0,0)$ positions will change. The actual forces will depend on the particular occupation of sites but it can be seen that there are situations when the forces will be applied to the dislocation in a cross-slip direction. Formby obtained experimental support for the mechanism of impurity-induced cross-slip from observations on cross-slip within slip bands and from changes in ductility.

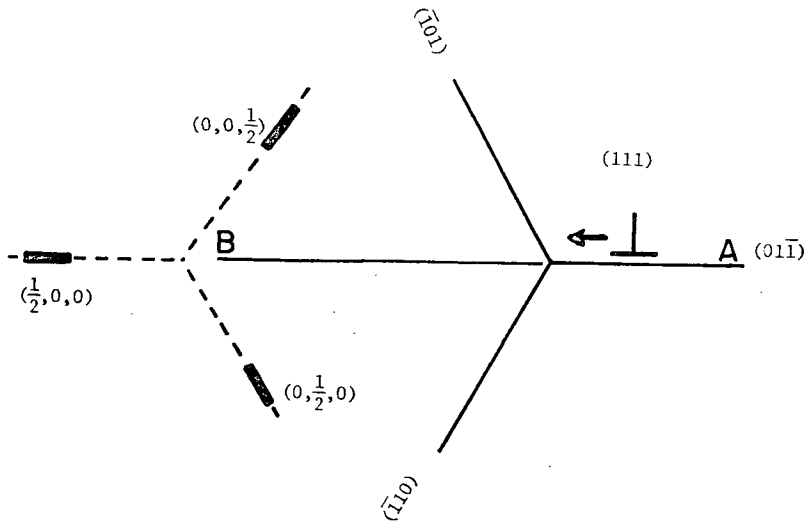

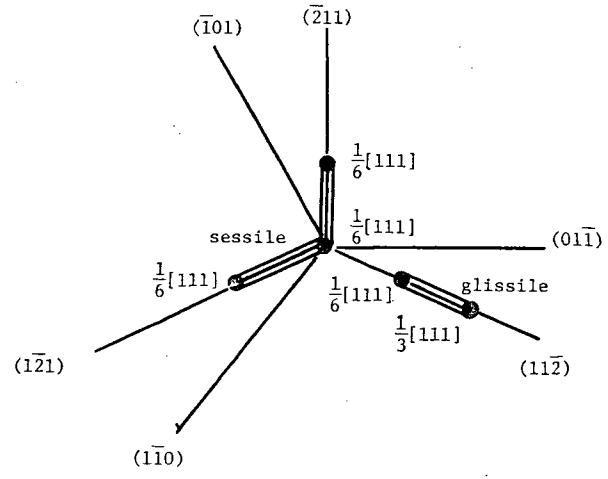

glissile: $\frac{1}{2}[111]_{(01\bar{1})} = \frac{1}{6}[111]_{(11\bar{2})} + \frac{1}{3}[111]_{(11\bar{2})}$

sessile: $\frac{1}{2}[111]_{(01\bar{1})} = \frac{1}{6}[111]_{(01\bar{1})} + \frac{1}{6}[111]_{(1\bar{2}1)} + \frac{1}{6}[111]_{(\bar{2}11)}$

Fig 47. Section through $\frac{1}{2}[111]$ screw dislocation:

a) approaching possible interstitial sites

b) showing all the possible {011} and {112} slip planes and two energetically favourable dissociations

b) Fig 47b shows a section through a [111] screw dislocation, together with all the possible {011} and {112} slip planes on which dissociation of the dislocation would be possible. Certain energetically favourable dislocation reactions involve sessile and glissile configurations; an example of each is shown. Using anisotropic elasticity theory, Vitek and Kroupa (1966) calculated the probabilities for transitions betweeen {112} and {110} planes and found good correlation with slip line and asymmetric critical shear stress data. However it must be recognized that the magnitude of the dissociation is too small to admit the existence of discrete partial dislocations.

It is conceivable that a combination of the above two approaches could explain the impurity interaction as well as the manner of screw dislocation motion. However in each model, the limit of applicability is set by the extent to which elasticity theory can be applied, since both are concerned with localized effects in the region of the dislocation core. It is rather discouraging to realize that this deficiency would become even more pronounced in any combined approach.

8. SUMMARY AND CONCLUSIONS

a) Oriented single crystals of Nb and dilute alloys of Nb with Mo and Ta were deformed in tension at various temperatures over a wide range of strain sensitivities, from microyield to macroscopic failure.

b) At 295°K, a small initial yield drop was followed by a multi-stage flow curve. Addition of Ta to Nb produced a slight parabolic hardening effect in spite of no atomic size difference; a very large linear hardening was produced by Mo additions. The primary slip system and the nature of slip were found to be unaffected by alloying; the active slip plane was non-crystallographic and was related to the orientation of the crystal.

c) At low temperatures or with large Mo additions, non-uniform deformation became evident. This behaviour, and the magnitude of the initial yield drop, was explained in terms of a stability criterion relating the yield stress and true work hardening rate.

d) The NbTa alloys deformed by slip at all temperatures, although sporadic twinning was in evidence at 77°K. At this temperature Nb was softened by the addition of Ta. At low temperatures twinning or cleavage failure without evidence of slip always occurred in NbMo alloys.

e) A high sensitivity microstrain technique was developed to give the stress versus strain relation from microyield ($\varepsilon \simeq 10^{-6}$) to macroflow ($\varepsilon > 10^{-3}$). Microyield was identified with the motion of edge dislocation segments; at higher stresses the screws begin to move and dislocation multiplication occurs. At macroflow, both edges and screws

move long distances through the crystal.

f) The microyield stress was found to be very sensitive to the initial distribution of mobile dislocations. Prestraining was necessary to eliminate the direct effect of impurities, which are believed to be of significance even in the highest purity bcc metals tested to date.

g) The temperature sensitivity of microyield was deduced to be a consequence of an interaction between interstitial impurities and the core of edge dislocations. It is suggested that the interaction with screw dislocations is stronger and becomes saturated at very low interstitial concentrations. The Peierls mechanism alone was found to be incapable of explaining the low temperature deformation of Nb. Furthermore the low temperature softening in NbTa alloys was also observed at microyield, and an interstitial association effect, rather than a reduction in Peierls stress upon alloying, was considered to be responsible.

h) The microstrain results indicated that the alloy effects were fairly independent of strain sensitivity; substitutional solute had a similar effect on the mobility of edges and screws. Previous suggestions that the concentration dependence of flow is a consequence of the concentration dependence of dislocation multiplication have been refuted. The Fleischer analysis of solid solution hardening was found to be unsuccessful when applied to bcc substitutional alloy systems. A statistical theory of alloy hardening may be more promising.

i) Two components of the internal stress field were recognized: one component always opposes dislocation motion and is determined by the dislocation density and solute concentration; the effect of the other

component depends on the direction of dislocation motion and is determined by the instantaneous distribution of mobile dislocations. Consequently the internal stress does not have a unique value below the macroflow stress and can itself be temperature dependent.

j) The significance of screw dislocation motion in the deformation of bcc metals and alloys was recognized. However the distinction between a "Peierls effect" and an "impurity effect" was considered semantic rather than basic in view of the predominance of interstitial-dislocation core interactions at a point where elastic calculations break down. The possible results of an exact calculation were suggested by means of different elastic approximations.

APPENDICES

A.1 Properties of relevant bcc metals

		Niobium	Molybdenum	Tantalum
Atomic number		41	42	73
Atomic weight		92.9	95.9	180.9
Metallic radius (Å)		1.43	1.37	1.43
Valence electrons		5	6	5
Melting point (°C)		2468	2610	2996
Vapour pressure at 2468°C (torr)		1×10^{-3}	3×10^{-2}	8×10^{-4}
Elastic compliances at 300°C: ($\times 10^{-12}$ $cm^2 dyn^{-1}$)				
(Carroll (1965), Featherstone and Neighbours (1963))	S_{11}	0.687	0.291	0.699
	S_{12}	-0.248	-0.818	-0.379
	S_{44}	3.41	0.823	1.22

A.2 Purity of vacuum-melted niobium

The mechanical properties of the bcc metals are very sensitive to the presence of small amounts of impurities, particularly the gaseous interstitial elements, oxygen and nitrogen. Since analysis of these elements becomes increasingly unreliable as their concentration is decreased, it is useful to estimate the amounts present under given melting conditions, by using calculations based on existing thermodynamic data.

Sieverts Law, which is a modification of Henrys Law, states that at constant temperature the solubility of a diatomic gas in a metal is proportional to the square root of the pressure.

Pemsler (1961) has published data for the interaction of Nb with O and N at temperatures near the melting point. This data is shown in Fig 48 in the form of Sieverts Law plots. From the slopes of the lines at 2470°C, the solubilities of O and N at a partial pressure p torr are given by:

$$[O]\text{at\%} = \frac{1}{0.45} p_{O_2}^{\frac{1}{2}} \qquad (1)$$

$$[N]\text{at\%} = \frac{1}{0.36} p_{N_2}^{\frac{1}{2}} \qquad (2)$$

If P torr is the operating pressure in the melting chamber (ie dynamic vacuum) and the gases are present in the proportions they are in air, then

$$p_{O_2} = 0.2\ P \qquad (3)$$

$$p_{N_2} = 0.8\ P \qquad (4)$$

Also, since

$$[O]\text{at\%} = \frac{1}{1740} [O]\text{ppm} \qquad (5)$$

$$[N]\text{at\%} = \frac{1}{1530} [N]\text{ppm} \qquad (6)$$

substituting equations (3) and (5) in (1), and (4) and (6) in (2), gives the amount of O and N (in wt ppm) in equilibrium with liquid Nb at 2470°C:

$$[O]\text{ppm} = 1730\ P^{\frac{1}{2}} \qquad (7)$$

$$[N]\text{ppm} = 3800\ P^{\frac{1}{2}} \qquad (8)$$

Equations (7) and (8) are plotted as full lines in Fig 49, from which it can be seen, for example, that at an operating pressure of 5×10^{-5} torr, the equilibrium concentrations of O and N are 12 and 27 ppm respectively.

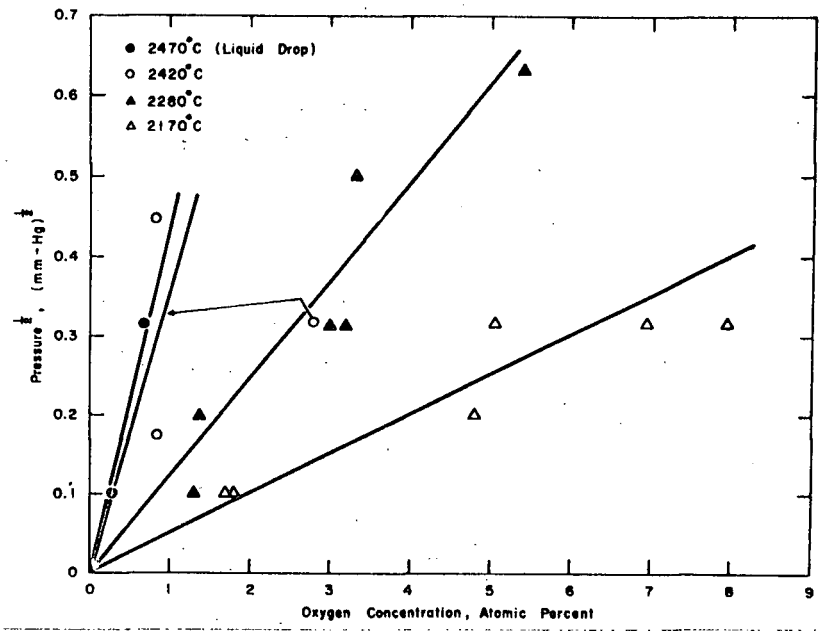

(a)

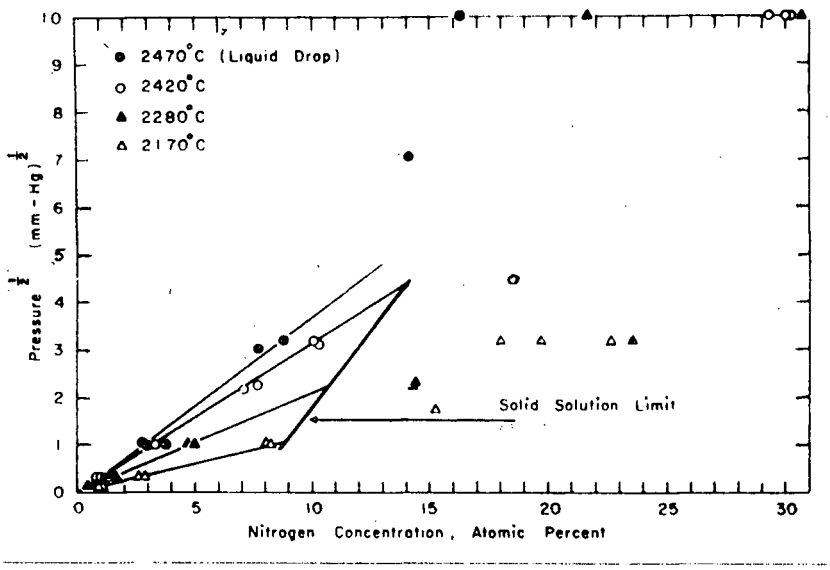

(b)

Fig 48. Sieverts Law plots of solubility of a) oxygen b) nitrogen in Nb at high temperatures (from Pemsler (1961)).

Since it is certain that the as-received Nb contained more than this amount of O and N, the calculated figures must represent the highest possible purity. The figures are a minimum because, as can be seen from Fig 48, the affinity of Nb for O and N increases at temperatures below the melting point. Pemsler's data has also been used to calculate the dashed curves in Fig 49, which show the amounts of O and N in equilibrium with solid Nb at 2170°C. It is evident that contamination of the melted Nb will occur after solidification. It is possible to determine the magnitude of the dynamic vacuum required for purification by high temperature annealing. For example, a pressure of less than 5×10^{-7} torr would be required to purify an alloy containing 12 ppm O by vacuum annealing at 2170°C.

A.3 Crystallography of slip

A.3.1 Definitions of slip parameters

Consider a dislocation line with Burgers vector $\underline{b}$, which can move conservatively on a general plane of normal vector $\underline{p}$, in a crystal subjected to a tensile stress, $\underline{\sigma}$.

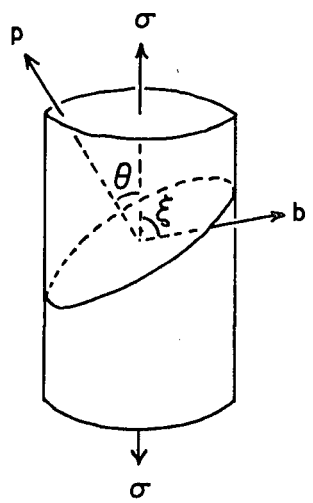

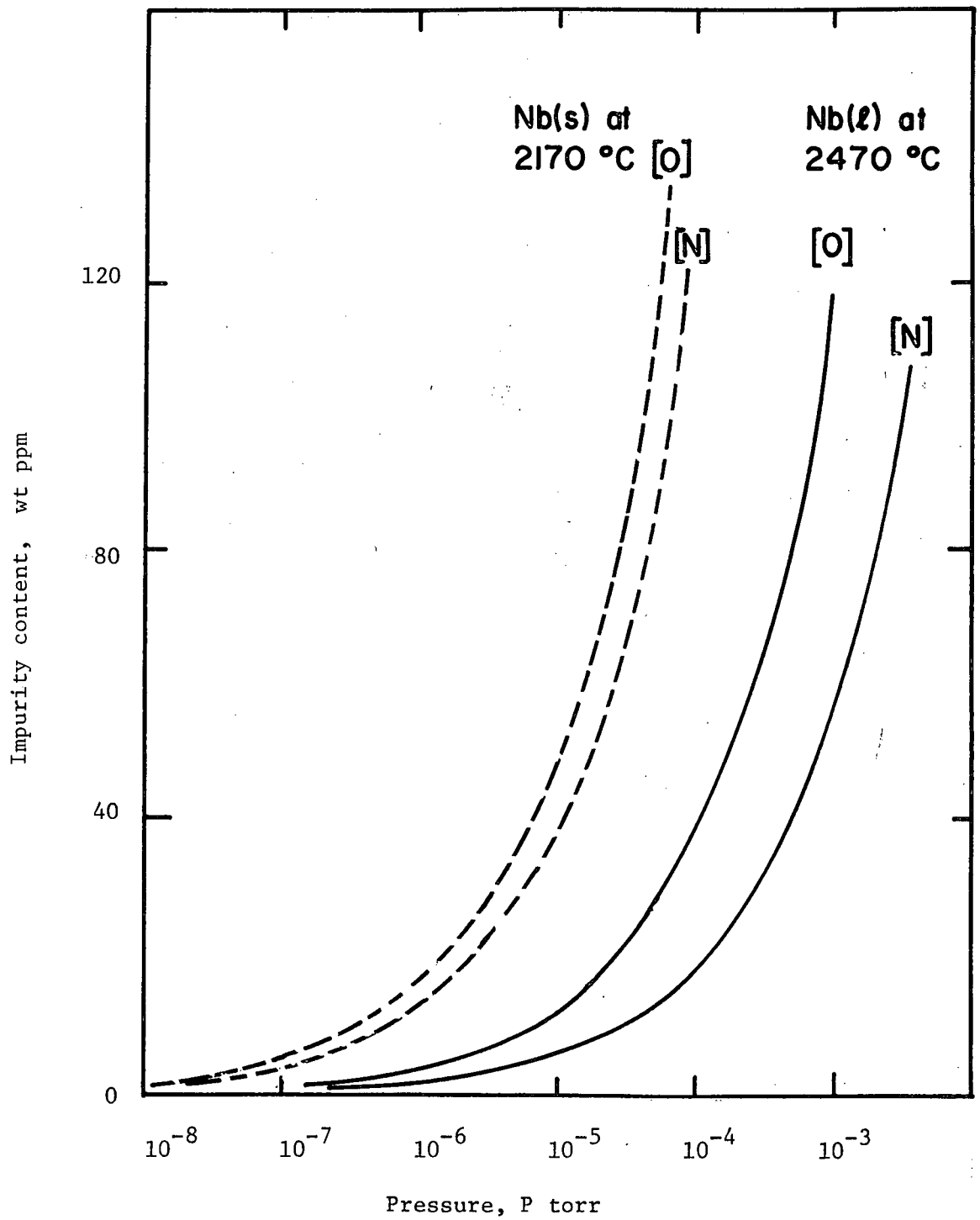

Fig 49. Calculated equilibrium solubilities of oxygen and nitrogen in Nb at high temperatures.

Glide motion is represented by $\underline{b}.\underline{p} = 0$

Let $\underline{\sigma} \wedge \underline{p} = \theta$

and $\underline{\sigma} \wedge \underline{b} = \xi$, as shown, where $\theta + \xi \geq 90°$

In bcc crystals, the Burgers vector is always of the type <111> , so that for a particular orientation, ξ is fixed. The resolved shear stress in the direction $\underline{b}$ on the plane $\underline{p}$ is given by

$$\tau(\theta) = \sigma.\cos\theta.\cos\xi$$

where $\cos\theta.\cos\xi$ is the Schmid factor for that slip system.

If no assumptions are made about slip planes being crystallographic, then the plane on which $\tau(\theta)$ is a maximum is of interest; the plane $\underline{p}$ becomes the "maximum resolved shear stress plane", $\underline{m}$. It corresponds to a minimum value of θ ($\theta + \xi = 90°$) which occurs when the vectors $\underline{m}$ $\underline{\sigma}$ and $\underline{b}$ are coplanar.

On the other hand, if the observed slip traces are measured and the direction of $\underline{p}$ is determined, then $\underline{p}$ is called the "observed slip plane", $\underline{n}$, and θ has the particular value, κ.

The shear stress resolved on the observed slip system is then given by

$$\tau_{\kappa} = \sigma.\cos\kappa.\cos\xi$$

where $\cos\kappa.\cos\xi$ is the observed Schmid factor, s.

These vectors can be represented as poles on a (001) stereographic projection, if the tensile axis $\underline{\sigma}$ is placed within the standard triangle [001] - [101] - [111]:

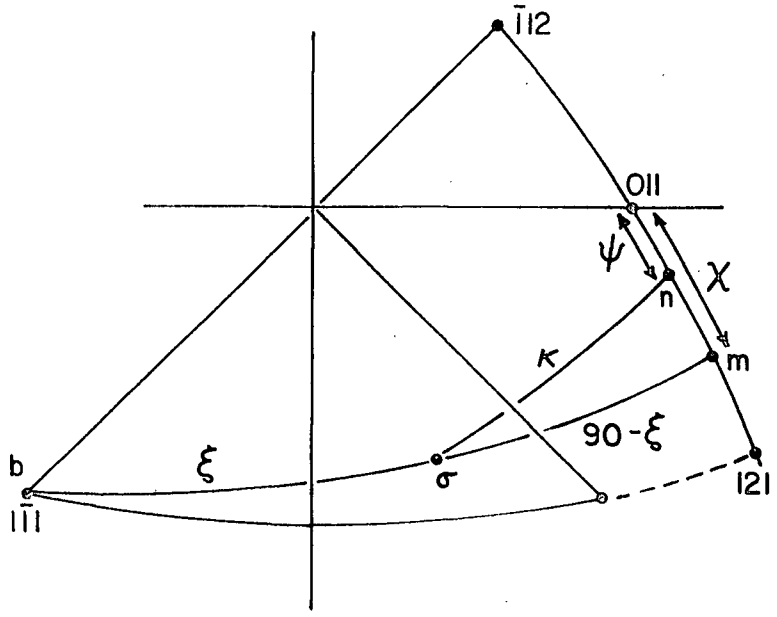

Because of the symmetry of the $(1\bar{1}1)$ pole, the (112) plane is equivalent to the (121); so it is useful to take (011) as a reference plane. The positions of $\underline{n}$ and $\underline{m}$ can then be determined by the angles ψ and χ that they make with the (011) pole, such that

$$-30^\circ \leq \psi, \chi \leq +30^\circ$$

A.3.1 Orientation dependence

It has been found experimentally (Sestak and Zarubova (1965)) that in crystals of different orientations, the observed slip plane (measured by ψ) does not depend on the angle ξ, but is a function only of the position of the maximum resolved shear stress plane (measured by χ). Thus the orientation dependence of the observed slip plane can be expressed by $\psi(\chi)$ for $-30^\circ \leq \chi \leq +30^\circ$.

If slip occurs on the maximum resolved shear stress plane, then

$$\psi = \chi$$

If slip is crystallographic: on (011) then $\psi = 0$

(143) $\psi = 14°$

(132) $\psi = 19°$

(121) $\psi = 30°$

In the past, crystallographic slip has been reported on all these planes (Bowen et al (1967), Milne and Smallman (1968)). However the accuracy of the slip line determinations is never quoted, so that whether slip is or is not crystallographic could depend on the statistical approach of the author.

The Oxford school (eg Foxall et al (1967)) take the observed asymmetry of ψ with respect to χ as evidence for discrete crystallographic slip on {112} planes. They divide the standard triangle into regions of expected operation of slip systems having {011} and {112} slip planes.

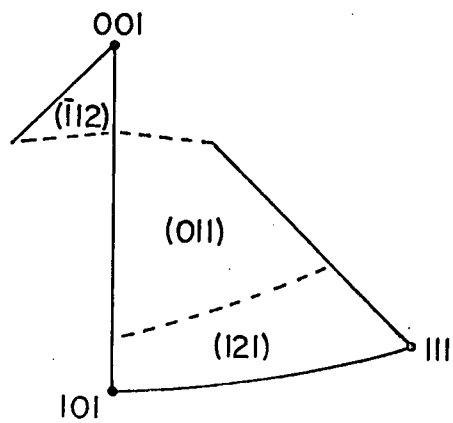

Thus the enclosed areas represent regions where the Schmid factor for a system with a $[1\bar{1}1]$ Burgers vector on the given slip plane is a maximum; the dotted boundary lines have equal Schmid factors on the adjacent systems.

To allow for non-crystallographic slip, the slip systems are here described in terms of the Burgers vector and the slip plane parameter:

$$[\underline{b}].\psi$$

A.3.3 Determination of slip systems

The slip plane can be determined by measuring the angle of inclination of the slip trace to the tensile axis (ϕ) at various angles (β) around the crystal.

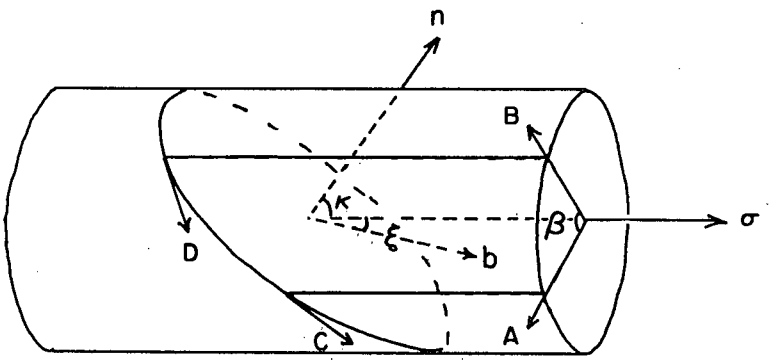

In the above diagram, the slip plane is represented by its normal vector $\underline{n}$; $\underline{C}$ is tangential to the slip plane at its point of maximum inclination to $\underline{\sigma}$; $\underline{A}$ represents $\beta = 0$ and is normal to $\underline{C}$ and $\underline{n}$; ξ is fixed for a given crystal orientation.

It is desired to determine κ from a knowledge of $\phi(\beta)$.

In Fig 50, the above angles are represented on a stereographic projection with $\underline{\sigma}$ again in the standard orientation and $\underline{b} = [1\bar{1}1]$.

$Z(\underline{n})$ represents the zone of the slip plane $\underline{n}$, and $Z(\underline{b})$ and $Z(\underline{\sigma})$ represent the zones of $\underline{b}$ and $\underline{\sigma}$ respectively.

Therefore, $\underline{A}$ lies at the intersection of $Z(\underline{\sigma})$ and $Z(\underline{n})$

$\underline{B}$ lies at β from $\underline{A}$ along $Z(\underline{\sigma})$

$\underline{C}$ lies at 90° from $\underline{A}$ on $Z(\underline{n})$

$\underline{D}$ lies at ϕ from $\underline{\sigma}$ on $Z(\underline{n})$ and at 90° to $\underline{B}$

Let $\underline{D} \wedge \underline{C} = \lambda$, then using Napiers Rule in Δ DCσ

$$\sin(90 - \phi) = \cos(90 - \kappa).\cos\lambda$$

therefore, $$\cos\phi = -\sin\kappa.\cos\lambda \qquad (1)$$

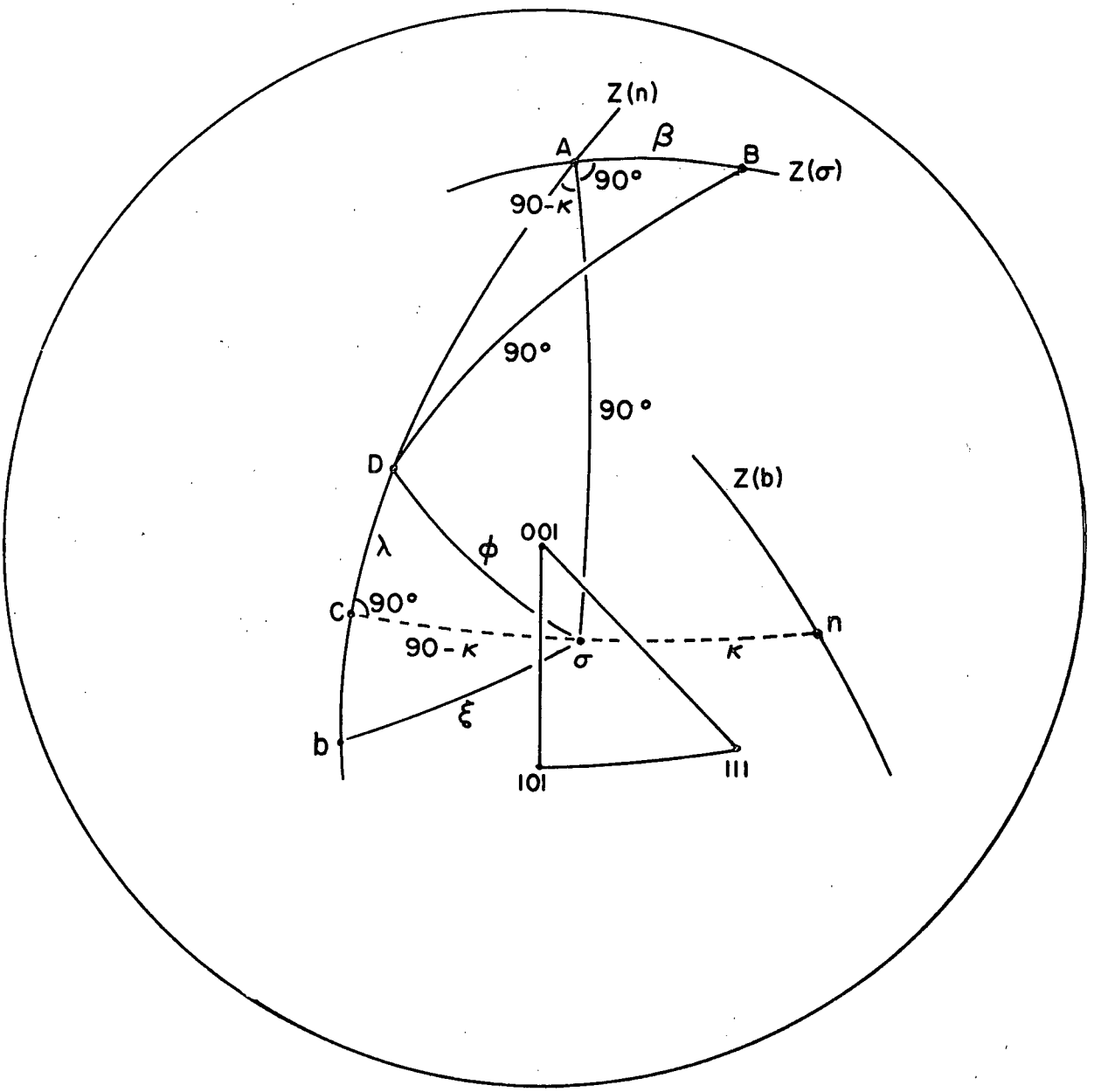

Fig 50. (001) Stereographic projection showing parameters for slip line analysis.

Using the Cosine Rule in Δ DAB :

$$\cos 90 = \cos\beta.\cos(90 - \lambda) + \sin\beta.\sin(90 - \lambda)\cos(180 - \kappa)$$

therefore, $$\cos\kappa = \cot\beta.\tan\lambda \qquad (2)$$

Eliminating λ from equations (1) and (2) gives:

$$\frac{\sin^2\kappa}{\cos^2\phi} = 1 + \cos^2\kappa.\tan^2\beta$$

therefore, $$\cos\phi = \pm \frac{\sin\kappa}{(1 + \cos^2\kappa.\tan^2\beta)^{\frac{1}{2}}} \qquad (3)$$

When $\beta = 0$, $\cos\phi = \sin\kappa = \cos(90 - \kappa)$

therefore, $\phi = 90 - \kappa$ which is the minimum value of ϕ.

When $\beta = 90$, $\cos\phi = 0$

therefore, $\phi = 90$

When $\beta = 180$, $\cos\phi = -\sin\kappa = \cos(90 + \kappa)$

therefore, $\phi = 90 + \kappa$ which is the maximum value of ϕ.

Fig 51 shows a theoretical plot of $\phi(\beta)$ calculated from equation (3). Any two experimental observations separated by $\beta \sim 90°$ would be sufficient to characterize the curve. In the case of single slip the graphical approach is unnecessary because an X-ray observation at known β can be used with a two-surface trace analysis to identify the slip plane.

However in the case of multiple slip, the cosine curves must be fitted to the observed points. The cosine curves for each system will have the same period, but may differ in phase and amplitude. Once the curve is established, the operative plane is determined as for single slip.

The operative Burgers vector can be determined absolutely if the point of disappearance of the slip lines is determined. Then $\underline{D}$ is parallel to $\underline{b}$ and so $\phi = \xi$, which identifies $\underline{b}$ for a known orientation.

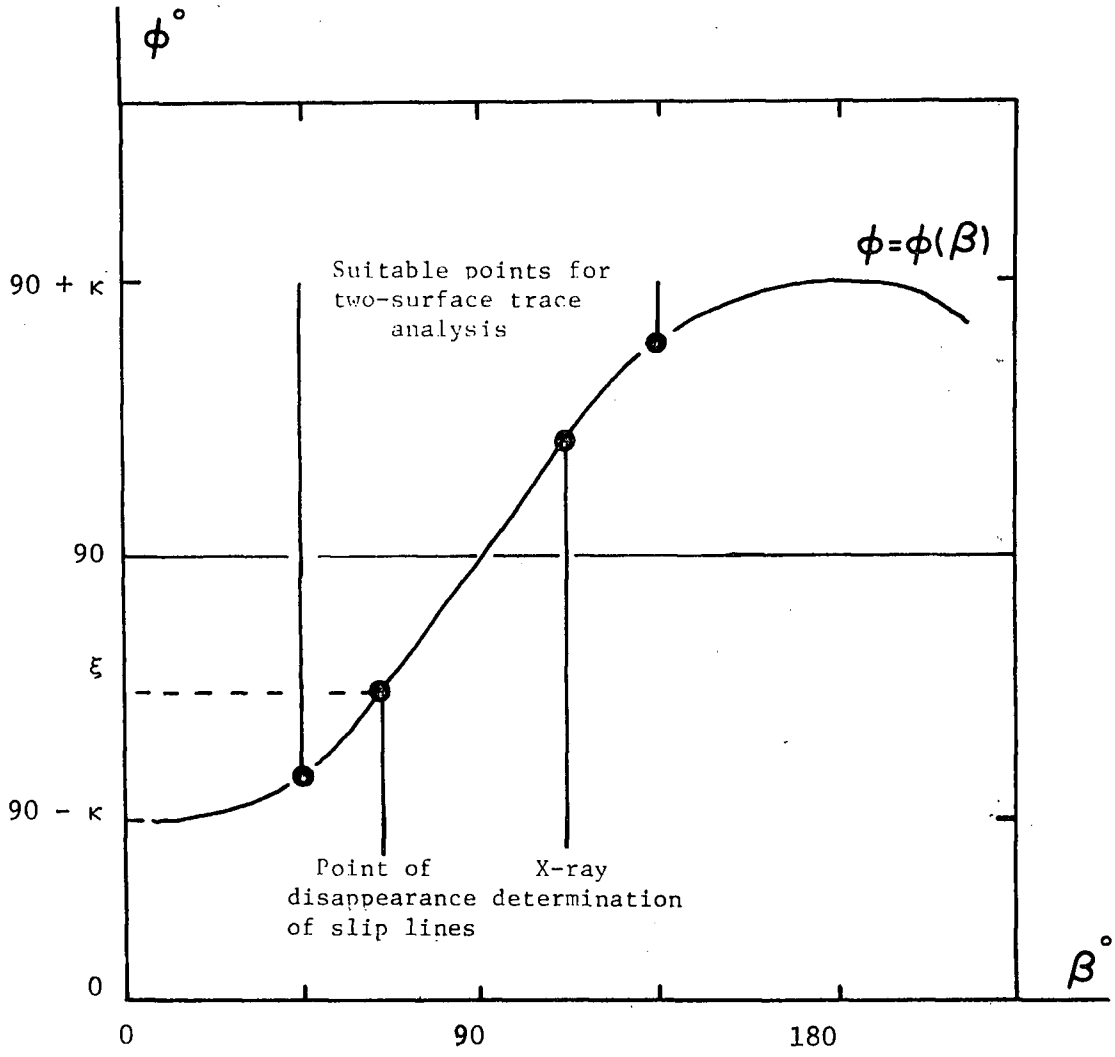

Fig 51. Plot of $\phi(\beta)$ showing information required for determination of one slip system.

A.4 Details of microstrain testing

A.4.1 Introduction

A microstrain experiment requires an instrument which is capable of measuring strains less than 10^{-4}. Some of the characteristics of possible types of extensometer are given in the table below:

	Capacitance	Differential transformer	Bonded resistance	Mechanical optical
Maximum strain sensitivity (1 in.gauge)	10^{-7}	10^{-6}	10^{-6}	10^{-10}
Attachment to specimen	direct	indirect	direct	direct
Operating temperature	room and below	room	room and below	room
Range	wide	wide	small	variable
Reversibility	excellent	excellent	fair	poor
Linearity	good	very good	poor	poor

In addition to the inherent sensitivity of the gauge, the operating limit is determined by the mechanical, electrical and thermal stability of the test assembly.

For testing in tension, over a range of temperature, the capacitance extensometer was selected as being the most suitable. The differential transformer is preferable for compression testing where direct attachment to the specimen is not required (Meakin (1967), Bowen et al (1967)).

The capacitance technique was pioneered by Brown and his co-workers at the University of Pennsylvania. The plate separation was determined from a direct measurement of the capacitance C which depends on plate

separation, ℓ, according to:

$$C \propto \frac{1}{\ell}$$

This means that the output, x, varies with plate separation according to:

$$\frac{dx}{d\ell} = \frac{dC}{d\ell} \propto \frac{1}{\ell^2}$$

The initial gap was set to the desired sensitivity using a micrometer attachment on the ground plate of the capacitance extensometer (Brown (1968)).

A.4.2 Equipment

The electronic micrometer used in this work is a commercial apparatus which gives a direct measurement of the separation between a probe and a grounded object. Thus $x \propto \ell$ and the sensitivity, $\frac{dx}{d\ell}$, is independent of plate separation.

The Wayne Kerr DM100B distance meter was manufactured by the Wayne Kerr Company Limited, New Malden, Surrey, England and consists of a stabilized power supply, 50 kHz oscillator, high gain amplifier and distance metering circuit. The output from the instrument was fed into a Wayne Kerr low pass filter, F731A, through a simple reverse voltage circuit to the X-axis of a Honeywell model 520 X-Y recorder having a maximum sensitivity of 0.1 mV in^{-1}. The output from the Instron load circuit was fed directly to the other axis of the recorder. The circuit is shown schematically in Fig 52.

A.4.3 Design of extensometer

The operation of the distance meter depends on comparing the test capacitance with an internal preset capacitor of value 0.35 pF. This value defines the maximum separation of the plates of the test

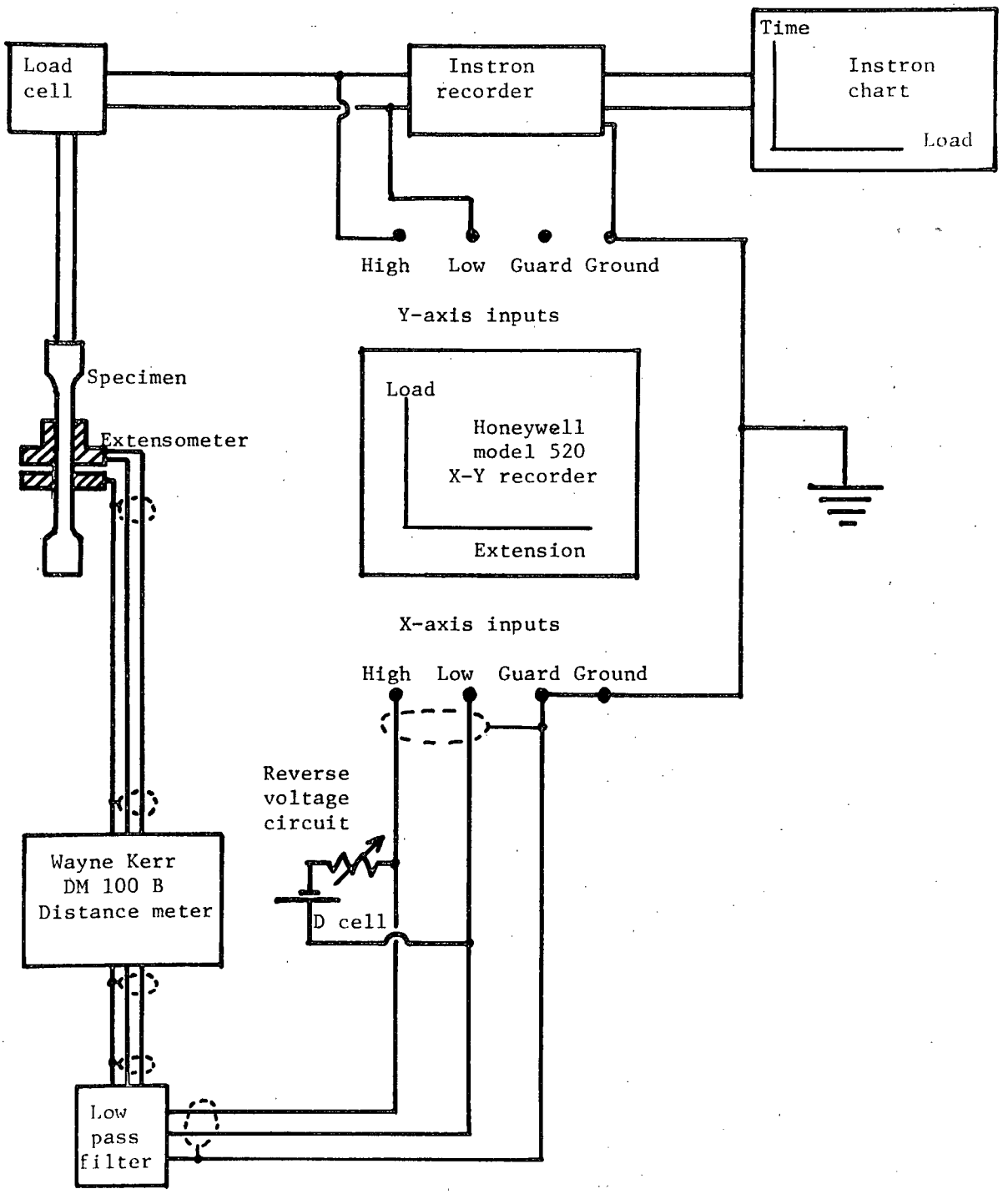

Fig 52. Schematic circuit diagram for microstrain testing.

capacitance, and is directly proportional to the area of the active plate. The displacement sensitivity is inversely proportional to the area of the plate. The active plate must be completely surrounded by a guard ring, and separated from it by a thin layer of insulation to ensure that the field is normal (or nearly so) to the surface of the plate. It is possible to relax this condition and, by decreasing the area of the active plate, increase the sensitivity at the expense of linearity. The instrument must then be specifically calibrated. This was the case in this design which gave adequate sensitivity without requiring excessive signal amplification. Detailed instructions for the design of special probes are given in the DM100B Instruction Manual, p.44.

A section through the cylindrical extensometer is shown diagrammatically below:

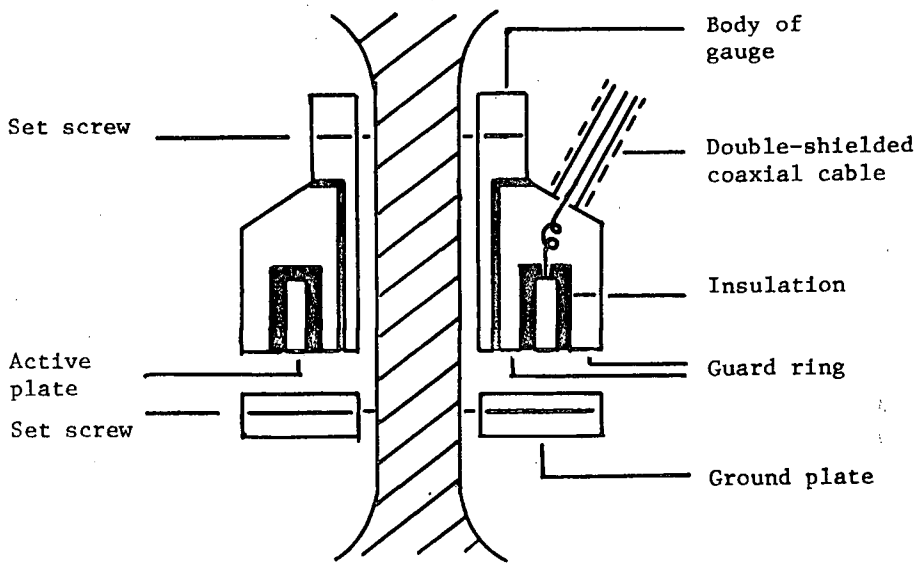

Material: brass
Insulation: mica and epoxy resin
Area of active plate: 0.039 in^2

The output from the distance meter is 0 - 1 mA at 1000 Ω. The distance meter reading, d, is in the range 0 - 10 units. The extensometer

was calibrated using feeler gauges and the results are shown in Fig 53. This gives d = d(ℓ) which is the meter reading as a function of true plate separation in thou.

The output corresponding to a meter reading d = 100.d mV

therefore, input to recorder = (100.d - V) mV

(where V is the reverse voltage in mV)

therefore, recorder displacement $x = \frac{(100.d - V)}{S}$

(where S is recorder sensitivity in mV in^{-1})

therefore, recorder displacement sensitivity $\frac{dx}{d\ell} = \frac{10^5}{S} \cdot \frac{dd}{d\ell}$

ins of chart / in displacement.

If E is the displacement represented by one small division of chart (= 0.1 in), then

$$E = S \left(\frac{dd}{d\ell} \right) \quad \text{inches displacement.}$$

This parameter has been calculated from the calibration curve in Fig 53 and is shown for different S values in Fig 54.

A.4.4 Testing

At room temperature, the microstrain test was performed using a conventional inverted tensile jig, with efforts made to eliminate draughts and vibrations. Room temperature stability was investigated prior to each test using the time-base mode on the Y-axis of the recorder.

For use at low temperatures, a gas-cooling cryostat was designed and built. The arrangement is shown schematically in Fig 55. Fig. 56 is a photograph of the testing assembly before lowering of the cryostat. The range of temperature operation was determined by the bath temperature. Fine adjustment was provided by controlling both the current through the grip heaters and the flow of cold gas, obtained by electrical heating of

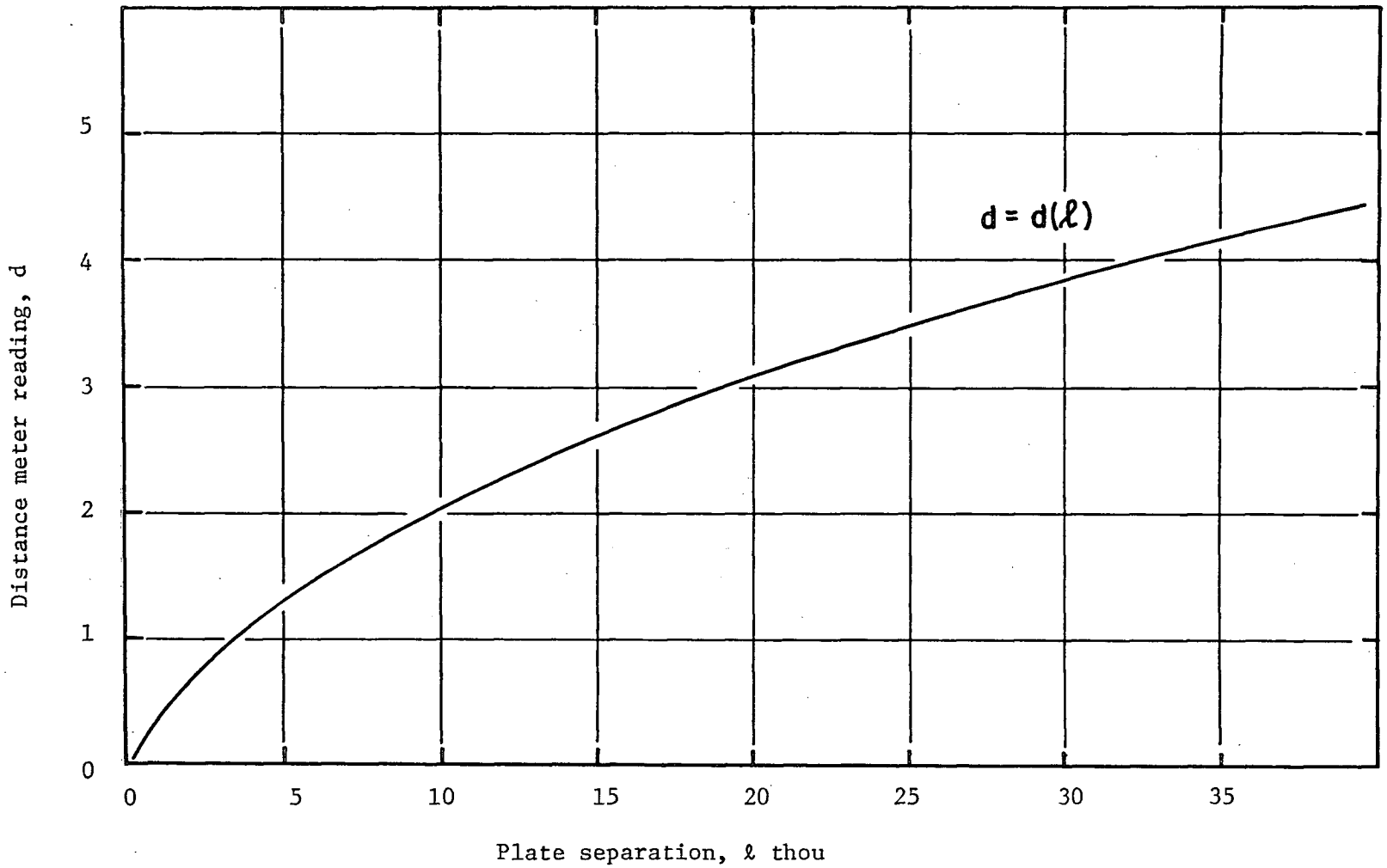

Fig 53. Distance meter reading as a function of plate separation.

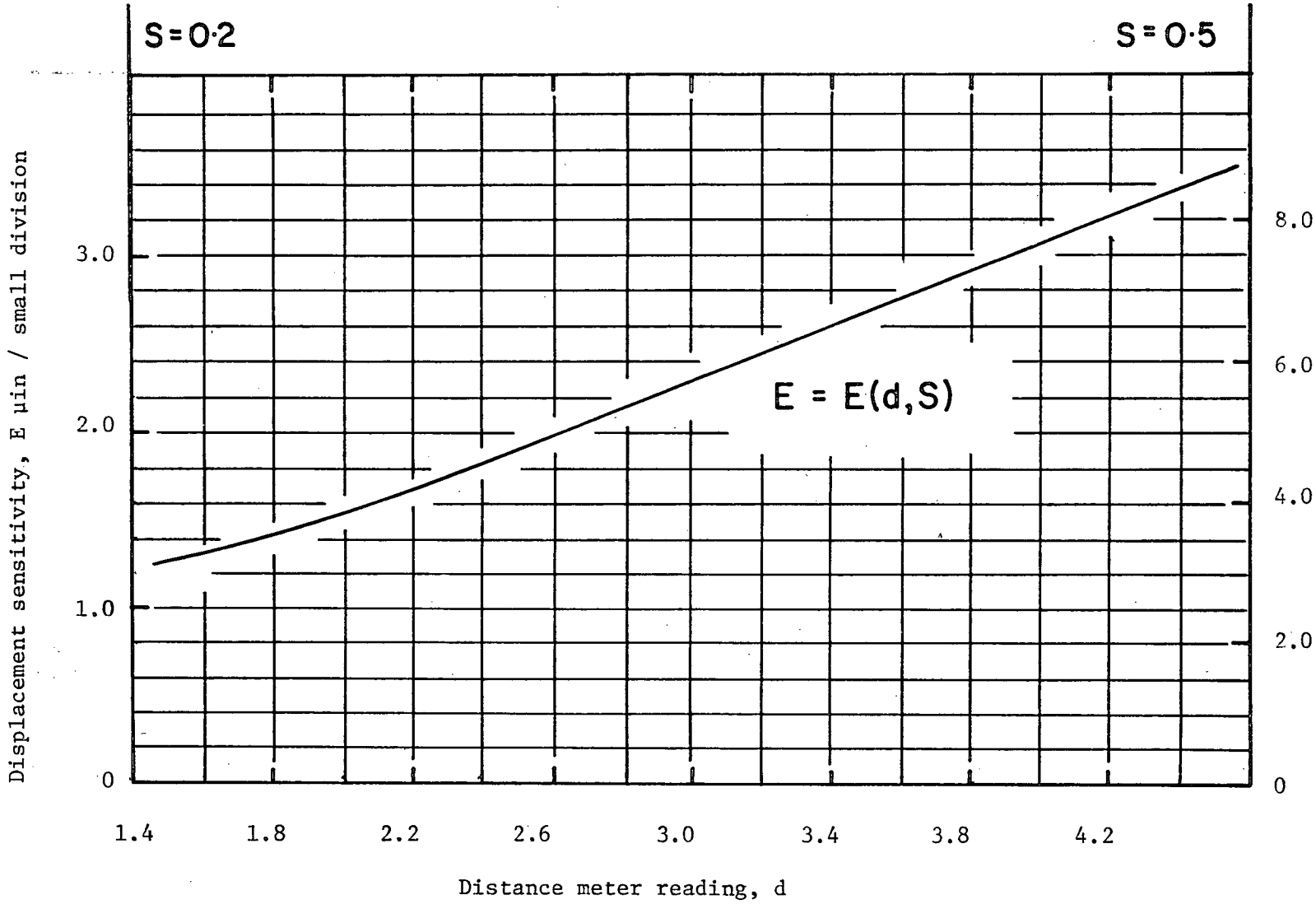

Fig 54. Displacement sensitivity of extensometer as a function of distance meter reading.

A - universal joints

B - heating coils on grips

C - contraction joint

D - dry gas inlet

E - capacitance extensometer

F - base plate

G - exit hole

Thermocouples not shown

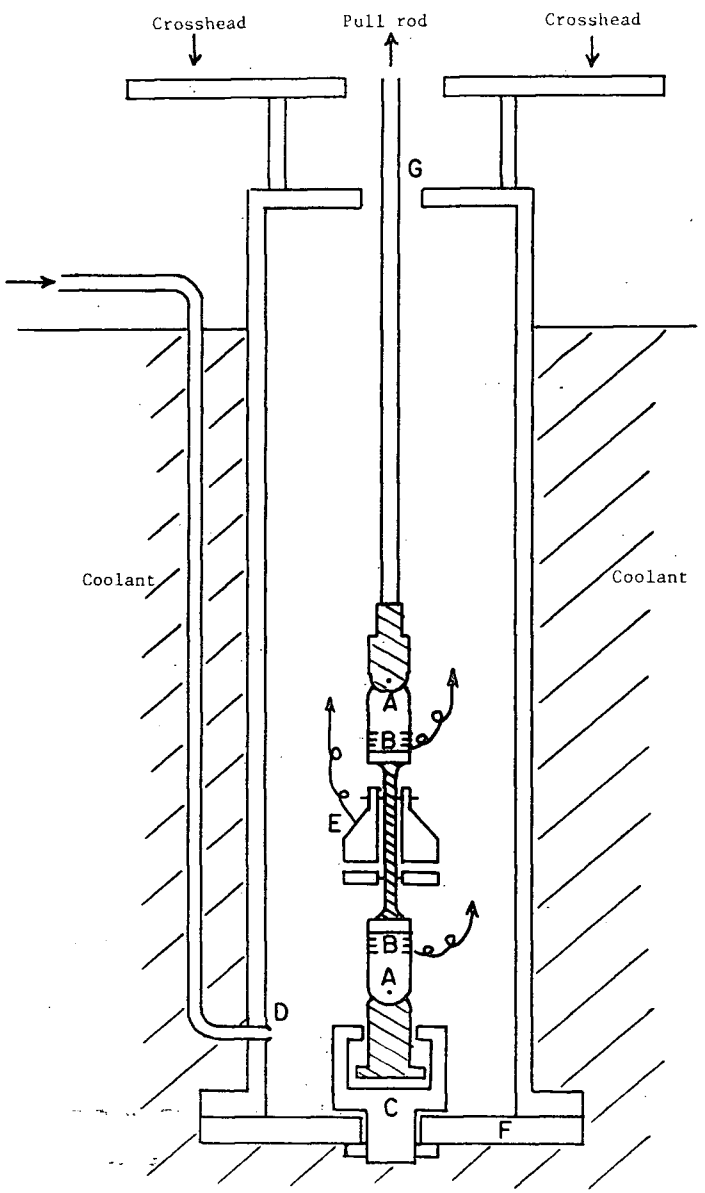

Fig 55. Schematic diagram of section through gas-cooling cryostat.

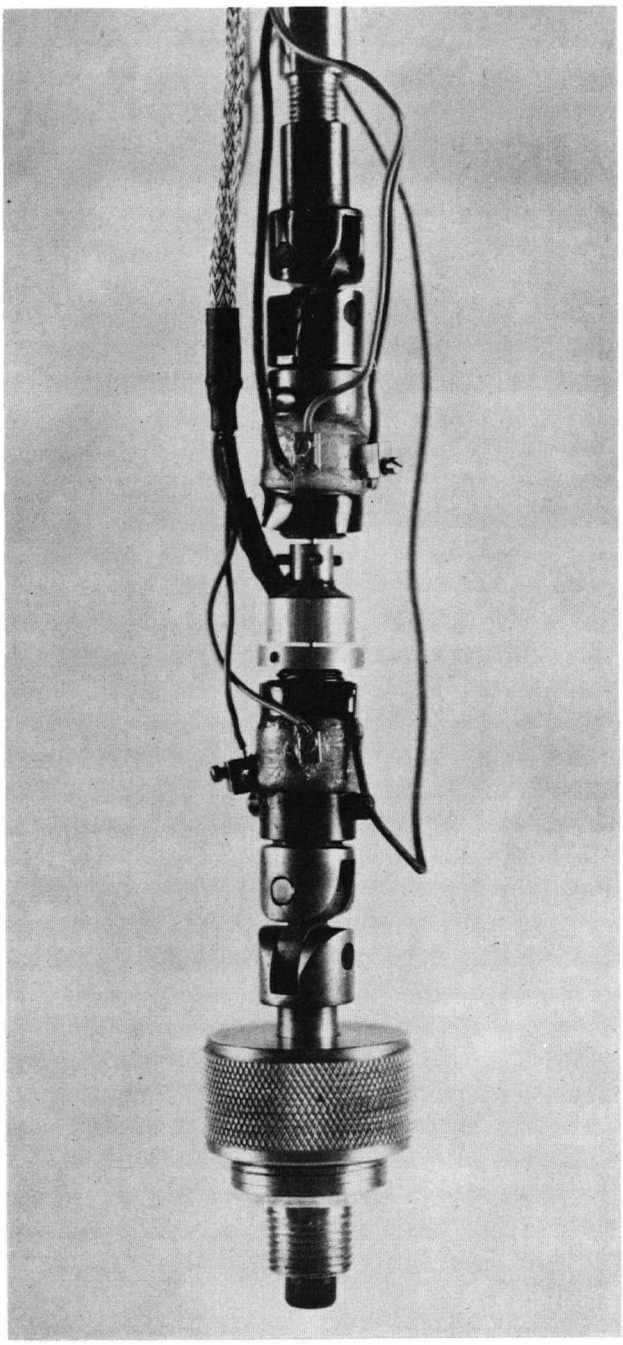

Fig 56. Test assembly for microstraining at low temperatures.

(cf Fig 55)

a coil immersed in liquid N_2. The temperature was measured by two thermocouples near the specimen shoulders, and required very accurate control. Stability was best gauged prior to testing, by monitoring the instantaneous stress and strain on the specimen during the operation of the Instron stress cycling procedure.

During testing, a continuous record of load versus time was obtained from the Instron chart recorder. The load cell could be calibrated on either the Instron chart of the X-Y recorder (Y-axis sensitivity = 1.0 mV $inch^{-1}$) and the relation between them obtained.

The alignment was established by repeatedly applying small loads until an exactly reversible linear trace was obtained. This could really only be done satisfactorily on specimens which had been prestrained in situ. The procedure adopted at room temperature is indicated in an idealized chart from the X-Y recorder in Fig 57.

A.5 Elastic constants in cubic single crystals

In a single crystal, many elastic constants may be required to define the anisotropic elastic behaviour. The value of Youngs modulus, E, and shear modulus, μ, will be a different combination of the constants for different crystal orientations and shear systems.

The particular expressions can be derived by applying the tensor transformation law to the generalized Hookes Law equation:

$$\varepsilon_{mn} = S_{mnpq}\,\sigma_{pq} \qquad (1)$$

where the repeated suffix convention is used and m n p q = 1,2,3. This equation expresses any component of the strain tensor ε_{mn} in terms of the stress tensor σ_{pq}. The S_{mnpq} are the "elastic compliances" and form a fourth order tensor. The tensors are referred to a right-handed set of

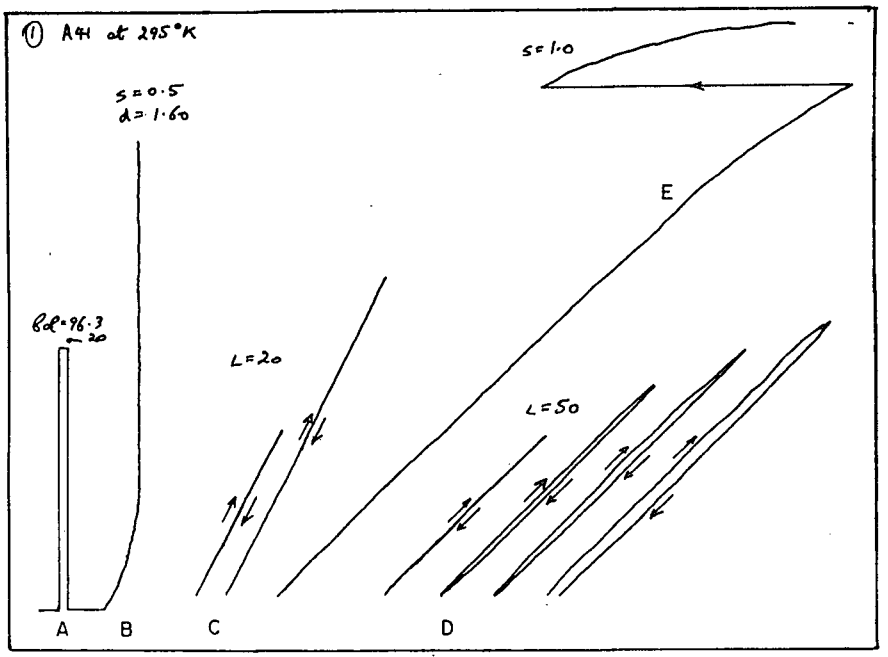

A - calibration of load cell on X-Y recorder
(L = full scale load in lbs)

B - stability test, with Y-axis on time base

C - alignment check

D - load cycling until permanent set

E - determination of flow curve

Fig 57. Idealized experimental X-Y recorder chart from microstrain test.

orthogonal axes, chosen to correspond with symmetry axes in the crystal.

Because of the symmetry of ε_{mn} and σ_{pq} , equation (1) can be expressed in shorter matrix form by the equation:

$$\varepsilon_i = S_{ij}\,\sigma_j \qquad (2)$$

where i, j = 1...6

Equations (1) and (2) are equivalent provided the following scheme is followed when changing from tensor to matrix notation (see Nye (1957)):

The pairs of suffixes mn become i , and pq become j according to

mn	11	22	33	23,32	13,31	12,21	pq
↓							↓
i	1	2	3	4	5	6	j

and in addition factors of ½ and ¼ are introduced into the S_{ij}:

$S_{mnpq} = S_{ij}$ (for i, j = 1, 2, 3)

$S_{mnpq} = \frac{1}{2}S_{ij}$ (either i or j = 4, 5, 6)

$S_{mnpq} = \frac{1}{4}S_{ij}$ (both i and j = 4, 5, 6)

The stress states of interest in this study are uniaxial tension and pure shear, but the resulting strains can only be obtained directly from the published S_{ij} if the stress state can be described directly by the original co-ordinate frame, x_i (i = 1, 2, 3).

Thus Youngs modulus in [100] is defined by

$$\frac{1}{E} = \frac{\partial \varepsilon_1}{\partial \sigma_1} = S_{11} \qquad (3)$$

and the shear modulus on (001) in [010] is given by

$$\frac{1}{\mu} = \frac{\partial \varepsilon_4}{\partial \sigma_4} = S_{44} \qquad (4)$$

The new co-ordinate frame, $\bar{x}_i$, is chosen to coincide with the direction of interest (for E) or the plane and direction of interest (for μ). The transformed tensor equation (1) becomes

$$\bar{\varepsilon}_{ij} = \bar{S}_{ijkl}\,\bar{\sigma}_{kl} \qquad (i, j, k, = 1, 2, 3)$$

The required $\bar{S}_{ijkl}$ can be obtained from the S_{mnpq} by applying the tensor transformation law for fourth order tensors:

$$\bar{S}_{ijkl} = a_{im}.a_{jn}.a_{kp}.a_{lq}.S_{mnpq} \tag{5}$$

where a_{ij} is the transformation matrix which relates the new frame $\bar{x}_i$ to the old, x_i. The components are defined as:

$$a_{ij} = \cos(\bar{x}_i \hat{} x_j) \tag{6}$$

From equations (3) and (4) the required moduli are:

$$\frac{1}{\bar{E}} = \bar{S}_{11} = \bar{S}_{1111} \tag{7}$$

and

$$\frac{1}{\bar{\mu}} = \bar{S}_{44} = \bar{S}_{3232} + \bar{S}_{3223} + \bar{S}_{2332} + \bar{S}_{2323} \tag{8}$$

In general, the symmetric matrix S_{ij} has 21 independent constants, but in the case of cubic crystals, this number is reduced to three and

$$S_{ij} = \begin{pmatrix} S_{11} & S_{12} & S_{12} & 0 & 0 & 0 \\ S_{12} & S_{11} & S_{12} & 0 & 0 & 0 \\ S_{12} & S_{12} & S_{11} & 0 & 0 & 0 \\ 0 & 0 & 0 & S_{44} & 0 & 0 \\ 0 & 0 & 0 & 0 & S_{44} & 0 \\ 0 & 0 & 0 & 0 & 0 & S_{44} \end{pmatrix}$$

From the non-zero values of S_{ij} we can obtain the non-zero values of S_{mnpq} to be used in the transformation equation (5). The

Table V. Non-zero terms for use in transformation equation (5) in the case of cubic crystals.

Non-zero i	j	Corresponding m	n	p	q	Equivalent S_{ij} (cubic)	Equivalent C_{ij} (cubic)
1	1	1	1	1	1	S_{11}	C_{11}
1	2	1	1	2	2	S_{12}	C_{12}
1	3	1	1	3	3	S_{12}	C_{12}
2	1	2	2	1	1	S_{12}	C_{12}
2	2	2	2	2	2	S_{11}	C_{11}
2	3	2	2	3	3	S_{12}	C_{12}
3	1	3	3	1	1	S_{12}	C_{12}
3	2	3	3	2	2	S_{12}	C_{12}
3	3	3	3	3	3	S_{11}	C_{11}
4	4	2	3	2	3	$\frac{1}{4}S_{44}$	C_{44}
		2	3	3	2		
		3	2	2	3		
		3	2	3	2		
5	5	3	1	3	1	$\frac{1}{4}S_{44}$	C_{44}
		3	1	1	3		
		1	3	3	1		
		1	3	1	3		
6	6	1	2	1	2	$\frac{1}{4}S_{44}$	C_{44}
		1	2	2	1		
		2	1	1	2		
		2	1	2	1		

particular value of the S_{mnpq} is then converted back to S_{ij} for cubic crystals. These operations have been performed in Table V.

A.5.1 Youngs modulus

If the tensile axis lies in a direction z relative to the old frame (which coincides with the tetrad axes in a cubic crystal) such that:

$$z \hat{} x_1 = \alpha$$

$$z \hat{} x_2 = \beta$$

$$z \hat{} x_3 = \gamma$$

then the new frame is selected so that $\bar{x}_1$ coincides with z .

From equation (6), it follows that the components of the i^{th} row of the transformation matrix are the components of a unit vector along $\bar{x}_i$ relative to the x_j frame. Thus $a_{ij} = \bar{x}_i . x_j$ and the relevant components in this case become:

$$a_{11} = \cos\alpha$$

$$a_{12} = \cos\beta$$

$$a_{13} = \cos\gamma$$

From equations (5) and (7),

$$\frac{1}{\bar{E}} = \bar{S}_{1111} = a_{1m} . a_{1n} . a_{1p} . a_{1q} . S_{mnpq}$$

The non-zero terms are obtained directly from the table by substituting the m, n, p, q and corresponding S_{ij} for cubic crystals. Thus,

$$\frac{1}{\bar{E}} = S_{11} (a_{11}^4 + a_{12}^4 + a_{13}^4)$$

$$+ S_{12} (2a_{11}^2 . a_{12}^2 + 2a_{12}^2 . a_{13}^2 + 2a_{13}^2 . a_{11}^2)$$

$$+ \tfrac{1}{4} S_{44} (4a_{11}^2 . a_{12}^2 + 4a_{12}^2 . a_{13}^2 + 4a_{13}^2 . a_{11}^2)$$

If η is defined as an orientation factor:

$$\eta = \cos^2\alpha.\cos^2\beta + \cos^2\beta.\cos^2\gamma + \cos^2\gamma.\cos^2\alpha$$

then the expression simplifies to:

$$\frac{1}{\bar{E}} = S_{11}.(1 - 2\eta) + (2S_{12} + S_{44}).\eta$$

A.5.2 Shear modulus

The shear modulus can be obtained similarly from equations (5) and (8) once the transformation matrix is determined.

If the shear is on a plane with normal vector $\underline{n}$ in direction $\underline{\beta}$, then the frame is selected so that $\bar{x}_3$ coincides with $\underline{n}$ and $\bar{x}_2$ coincides with $\underline{\beta}$.

Again the components of the transformation matrix are given by $a_{ij} = \bar{x}_i.x_j$, where $\bar{x}_i$ and x_j are unit vectors.

Consider for example, a shear on (112) in $[\bar{1}\bar{1}1]$ which is a twinning shear in bcc metals:

$$\bar{x}_3 = [112]$$

$$\bar{x}_2 = [\bar{1}\bar{1}1]$$

therefore,

$$a_{31} = \frac{1}{\sqrt{6}}\,[112].[100] = \frac{1}{\sqrt{6}}$$

$$a_{32} = \frac{1}{\sqrt{6}}\,[112].[010] = \frac{1}{\sqrt{6}}$$

$$a_{33} = \frac{1}{\sqrt{6}}\,[112].[001] = \frac{2}{\sqrt{6}}$$

Similarly, $a_{21} = -\frac{1}{\sqrt{3}}$, $a_{22} = -\frac{1}{\sqrt{3}}$, $a_{23} = \frac{1}{\sqrt{3}}$

If these values are substituted in equations (5) and (8) and

a change made to matrix notation, the resulting expression for the shear modulus is:

$$\frac{1}{\bar{\mu}} = \frac{1}{3}\left[S_{44} + 4(S_{11} - S_{12})\right]$$

Since the transformation matrix is symmetrical with respect to $\underline{n}$ and $\underline{\beta}$, $\bar{\mu}$ remains the same if $\underline{n}$ and $\underline{\beta}$ are interchanged.

Expressions for $\frac{1}{\bar{\mu}}$ for other shears in cubic crystals are:

(001) [110]	S_{44}
(110) [1$\bar{1}$0]	$2(S_{11} - S_{12})$
(111) [1$\bar{1}$0]	$\frac{1}{3}[S_{44} + 4(S_{11} - S_{12})]$

Similar equations to these can be obtained by expressing the stress components σ_i in terms of the strain components ε_j

$$\sigma_i = C_{ij}\,\varepsilon_j \qquad \text{(cf equation (2))}$$

where the C_{ij} are the "elastic stiffness constants".

The relations between the S_{ij} and C_{ij} for the cubic system are given by:

$$S_{11} - S_{12} = \frac{1}{C_{11} - C_{12}}$$

$$S_{11} + 2S_{12} = \frac{1}{C_{11} + 2C_{12}}$$

$$S_{44} = \frac{1}{C_{44}}$$

It can be seen that for the shears (001) [110] and (110) [1$\bar{1}$0]

$$\frac{1}{\bar{\mu}(S_{ij})} \equiv \bar{\mu}(C_{ij})$$

but this is not the case for the shear (111) [1$\bar{1}$0] which is of

importance in bcc deformation. Since deformation experiments apply a particular stress and measure the resulting strains, the modulus should be expressed in terms of S_{ij} rather than C_{ij}, as is usually the case (Bowen et al (1967), Mitchell and Raffo (1967)).

A shear modulus useful for solution hardening theory is Voigts' average:

$$\left(\frac{1}{2S_{44}(S_{11} - S_{12})} \right)^{\frac{1}{2}}$$

In the case of an isotropic crystal (eg tungsten) or a polycrystal there are only two independent elastic constants

$$E = \frac{1}{S_{11}} \quad \text{and} \quad \mu = \frac{1}{S_{44}} = \frac{1}{2(S_{11} - S_{12})}$$

and Voigts expression reduces to μ.

REFERENCES

Ahktar A. (1968). PhD Thesis, University of British Columbia

Allen B.C. and Jaffee R.F. (1963). Trans ASM 56 387

Arsenault R.J. (1967). Acta Met 15 501

(1969). Acta Met 17 1291

Arsenault R.J. and Lawley A. (1967). Phil Mag 15 549

Bowen D.K., Christian J.W. and Taylor G. (1967). Can J. Phys 45 903

Brown N. (1968). Microplasticity p.52, Interscience, New York

Brown N. and Ekvall R.A. (1962). Acta Met 10 1101

Calverley A., Davis M. and Lever R.F. (1957). J. Sci Inst 34 142

Carnahan R.D., Arsenault R.J. and Stone G.A. (1967). Trans Met Soc AIME 239 1193

Carroll K.J. (1965). J. Appl Phys 36 3689

Christ B.W., Gamble R.P. and Smith G.V. (1969). Scripta Met 3 521

Cochardt A.W., Schoeck G.S. and Wiedersich H. (1955). Acta Met 3 533

Conrad H. (1963). NPL Symposium p.476, London, HMSO

Cottrell A.H. (1963). NPL Symposium p.456, London, HMSO

Cottrell A.H. and Bilby B.A. (1949). Proc Phys Soc A62 49

Davies R.G. and Gilbert A. (1967). Acta Met 15 665

Davies R.G. and Ku R.C. (1966). Trans Met Soc AIME 236 1691

Doyama M. and Cotterill R.M.J. (1968). Trans Jap Inst Metals 9 suppl 55

Duesbery M.S. (1967). PhD Thesis, University of Cambridge

Featherstone F.H. and Neighbours J.R. (1963). Phys Rev 130 1324

Fleischer R.L. (1961). Acta Met 9 996

(1962). Acta Met 10 835

(1963). Acta Met 11 203

(1967). Acta Met 15 1513

Formby C.L. (1966). Phil Mag 14 745

Foxall R.A., Duesbery M.S. and Hirsch P.B. (1967). Can J. Phys 45 607

Fraser R.W. and Lund J.A. (1962). Can Met Q. 1 1

Gibala R. and Wert C.A. (1966). Acta Met 14 1095

Hahn G.T. (1962). Acta Met 10 727

Haasen P. (1965). Alloying behaviour and effects in concentrated solid solutions p.270, Gordon and Breach, New York

(1968). Trans Jap Inst Metals 9 suppl XL

Harris B. (1966). Phys Status Solidi 18 715

Hendrickson A.A. (1969). Private communication

Hutchison M.M. (1963). Phil Mag 8 121

Keh A.S. (1968). Dislocation dynamics p.483, McGraw-Hill, New York

Keh A.S. and Weissman S. (1963). Electron microscopy and strength of crystals p.231, Interscience, New York

Kelly P.M. (1969). Scripta Met 3 149

Kocks U.F. (1966). Phil Mag 13 541

(1967). Can J. Phys 45 737

(1968). Trans Jap Inst Metals 9 suppl 1

(1969). To be published in: Physics of strength and plasticity, MIT Press, Cambridge, Massachusetts

Koo R.C. (1963). Acta Met 11 1093

Koss D.A. (1969). Pratt and Whitney Aircraft Corporation. Unpublished results

Kossowsky R. and Brown N. (1966). Acta Met 14 131

Kostorz G. (1968). Z. Metallk 59 941

(1969). Trans Met Soc AIME 245 2102

Kroupa F. and Vitek V. (1967). Can J. Phys 45 945

Lawley A. and Gaigher H.L. (1964). Phil Mag 10 15

Maddin R. and Chen N.K. (1953). Trans Met Soc AIME 197 1131

Meakin J.D. (1967). Can J. Phys 45 1121

Milne I. and Smallman R.E. (1968). Trans Met Soc AIME 242 120

Mitchell T.E., Foxall R.A. and Hirsch P.B. (1963). Phil Mag 8 1895

Mitchell T.E. and Raffo P.L. (1967). Can J. Phys 45 1047

Mordike B.L. (1962). Z. Metallk 53 586

Mott N.F. and Nabarro F.R.N. (1948). Bristol conference p.1, Phys Soc, London

Nabarro F.R.N. (1968). Dislocation dynamics p.475, McGraw-Hill, New York

Nakamura S. and Muller E.W. (1965). J. Appl Phys 36 3634

Nye J.F. (1957). Physical properties of crystals, Oxford U.P., Oxford

Pemsler J.P. (1961). J. Electrochem Soc 108 744

Peters B.C. and Hendrickson A.A. (1966). Acta Met 14 1121

Place T.A. (1969). PhD Thesis, University of British Columbia

Prekel H.C. and Conrad H. (1968). Dislocation dynamics p.431, McGraw-Hill, New York

Raffo P.L. (1969). J. Less-common Metals 17 133

Raffo P.L. and Mitchell T.E. (1968). Trans Met Soc AIME 242 907

Ravi K.V. and Gibala R. (1969). Scripta Met 3 547

Schoeck G. and Seeger A. (1959). Acta Met 7 469

Sestak B. and Zarubova N. (1965). Phys Status Solidi 10 239

Solomon H.D. and McMahon C.J. (1968). Work hardening, Gordon and Breach, New York

Statham C.D. (1968). D.Phil Thesis, University of Oxford

Stein D.F. (1968). Microplasticity p.141, Interscience, New York

Stoloff N.S., Davies R.G. and Ku R.C. (1965). Trans Met Soc AIME 233 1500

Szkopiak A.C. (1966). Physical basis of yield and fracture p.108, Inst Phys and Phys Soc, London

Taylor G. and Christian J.W. (1965). Acta Met 13 1216

Thomas W.R. and Leak G.M. (1954). Phil Mag 45 656

Tyson W.R. (1967). Can Met Q. 6 301

Vitek V. and Kroupa F. (1966). Phys Status Solidi 18 703

Votava E. (1965). J. Less-common Metals 9 409